Diss. ETH 16466

Body-Worn Inertial Electromagnetic Micro-Generators

A dissertation submitted to the

SWISS FEDERAL INSTITUTE OF TECHNOLOGY
ZURICH

for the degree of
Doctor of Sciences

presented by

Thomas von Büren
Dipl. Ing. ETH
born 12th March 1974
citizen of Flumenthal SO

accepted on the recommendation of

Prof. Dr. Gerhard Tröster, examiner
Prof. Dr. Christofer Hierold, co-examiner

2006

To Andrea

Acknowledgements

If I have been able to see farther, it was only because I stood on the shoulders of giants.
(Isaac Newton, 1675, in a letter to Robert Hooke)

Figuratively speaking, this doctoral thesis has been possible because I was able to stand on the 'shoulders' of many people:

First of all, I would like to thank my advisor, Prof. Dr. Gerhard Tröster, for giving me the opportunity to carry out research and write a Ph.D. thesis in the exciting and promising field of wearable computing. I have enjoyed the open-minded research atmosphere in his group.

I am grateful to Prof. Dr. Christofer Hierold who accepted to review my thesis and act as co-examiner.

Special thanks go to Walter Bachmann, Roy Hunziker, and Peter Brühwiler of the mechanical workshop at the Physics Department and Martin Vogt of the workshop at the Electrical Engineering Department for fabricating early prototypes as well as drawing the construction plans and fabricating the final generator prototype. Without their support, I would not have been able to build a working generator.

My sincere appreciation also goes to Paul Mitcheson of Imperial College, the co-author of one of my publications. Various aspects of this thesis are at least partly based on his inputs during our discussions.

I would like to thank Dr. Klaus Häusler of the Institute of Mechanical Systems for the valuable discussions regarding the mechanical generator aspects. Dr. Stephan Busato and Dr. Adrian Neild of the same institute have provided me with the measurement equipment for the generator evaluation.

Gerold Brändli of the Electronics Lab deserves my gratitude for providing me with contacts in the generator watch industry which lead to useful input from Walter Hammer of Crossmos Ltd and Nadim Azzam of NA Unternehmensberatung.

I have also received a lot of support from the members of my research group, especially Urs Anliker, Mathias Stäger, Holger Junker, Marc von

Waldkirch, and Ivo Locher. They have volunteered as subjects for the acceleration measurements, have participated in scientific discussions and have encouraged me in times when things were not going well.

I owe special thanks to my parents, who supported and encouraged me in all situations. Finally, I would like to thank my girl-friend, Andrea Aeschbacher, for her understanding, support and unconditional love.

Zürich, February 2006 THOMAS VON BÜREN

Contents

Abstract

This doctoral thesis discusses the potential and the limitations of body-worn mechanical generators, with a special focus on inertial electromagnetic architectures. The main objective is to develop a generator architecture that can serve as power supply for body sensor networks (BSNs).

BSNs could have a major impact on how health care is conducted in the future. By continuously monitoring the life signs of patients and analyzing the signal patterns, dangerous medical conditions can be detected earlier and diagnoses could be improved, leading to more effective treatment. One of the big obstacles on the way towards this vision is the power supply of the sensor nodes. Finite energy sources such as batteries require user maintenance and are not practical for BSN, especially, if many sensor nodes are used. A possible solution to the power supply issue is 'harvesting' ambient mechanical energy using body-worn inertial (vibration-driven) generators. These generators extract a small amount of mechanical energy and convert it to electrical energy when the human body is moving. However, due to the low frequencies of human motion, generating enough electrical power for BSNs is challenging. A suitable generator architecture and design optimization are therefore essential.

This thesis proposes a novel linear inertial electromagnetic generator architecture intended for body-worn power supplies. The architecture is based on the combination of a tubular air-cored electromagnetic generator and a flexible parallel-spring bearing. This architecture enables high-efficiency operation through a high electromagnetic force capability and low parasitic mechanical damping: For short-circuit operation of the fabricated prototypes in this thesis, the measured ratio of elecromagnetic force to translator velocity is 0.15 to 0.25 Ns/m. The measured parasitic mechanical damping is 0.0045 to 0.0060 Ns/m, which is 25 to 50 times smaller. Mechanical and resistive losses taken into account, the overall generator efficiency is 65% to 75%. Simulations show that for a generator volume of $0.25\,\mathrm{cm}^3$, the achievable generator power is between 2 and $25\,\mu$W, depending on the mounting location on the human body and the driving motion. This power level is sufficient for many sensing applications.

In order to optimize the generator design parameters, an optimization method is presented. The method is based on two stages. The first stage uses electromagnetic finite element analysis to find the geometry of the generator that yields maximum electrical damping force. The second stage uses the geometry of the first stage and finds the resonance frequency and electrical load which lead to maximum electrical output power. The optimization results show that the optimal values for some geometric parameters are independent from generator volume. In addition, it is shown that the optimal resonant frequency does not simply lie at the fundamental frequency of the human motion, as often assumed. Instead, the optimal resonant frequency is 5 to 20 times higher, which leads to higher output power than previously estimated.

All inertial generator simulations in this thesis use measured acceleration waveforms as driving motion. The waveforms have been acquired from eight subjects and nine different positions on the human body during normal walking. Thus, the simulated power levels reflect typical operation conditions of body-worn mechanical generators.

In conclusion, this thesis shows that efficient $\mathrm{sub-cm}^3$ electromagnetic inertial generators can be designed and thus represent a viable option for the power supply of body-worn sensors networks.

Zusammenfassung

Die vorliegende Doktorarbeit behandelt das Potential und die Grenzen von mechanischen Generatoren, die am Körper getragen werden, mit vertiefter Betrachtung elektromagnetischer Trägheitsarchitekturen. Das Ziel ist die Entwicklung einer Generatorarchitektur, welche als Energiequelle für vernetzte Sensoren auf dem Körper (Körpersensor-Netzwerke) verwendet werden kann.

Körpersensor-Netzwerke könnten einen grossen Einfluss auf das zukünftige Gesundheitswesen haben. Durch die kontinuierliche Überwachung der Körperfunktionen von Patienten und die anschliessende Analyse der Signale lassen sich medizinische Notfälle rascher erkennen, sowie Diagnosen qualitativ verbessern, was zu einer effektiveren Behandlung führt. Eines der grossen Hindernisse, welche dieser Vision im Wege stehen, ist die Energieversorgung der Körpersensoren. Quellen mit endlicher Energie, wie zum Beispiel Batterien, erfordern eine Wartung der Sensorknoten und sind daher insbesondere für Körpersensor-Netzwerke mit vielen Sensorknoten nicht geeignet. Eine mögliche Lösung für die Energieversorgung ist das Abschöpfen von mechanischer Energie aus der Umgebung der Sensoren durch vibrationsgetriebene, körpergetragene Generatoren (Trägheitsgeneratoren). Wenn eine Person einen solchen Generator trägt und sich bewegt, entnimmt der Generator eine kleine Menge mechanischer Energie und wandelt sie in elektrische Energie um. Allerdings ist die Erzeugung von genügend Energie für Körpersensor-Netzwerke anspruchsvoll, da die menschliche Bewegung meist nur tiefe Frequenzen enthält.

In dieser Doktorarbeit wird eine neuartige Architektur eines linearen, trägheitsbasierten, elektromagnetischen Generators für Körpersensor-Netzwerke präsentiert. Die Architektur basiert auf der Kombination einer zylinderförmigen Generatortopologie mit eisenlosem Stator und einer elastischen Parallelfeder-Führung. Die Architektur ermöglicht eine hohe elektromagnetische Dämpfungskraft und eine kleine mechanische Reibung und als Folge davon einen Generatorbetrieb mit hoher Effizienz. Die Generatorprototypen, die im Rahmen dieser Doktorarbeit hergestellt wurden, haben eine auf die Geschwindigkeit bezogene Dämpfungskraft von 0.15 bis 0.25 Ns/m. Die mechanische Dämpfung

durch Reibung ist 0.0045 bis 0.0060 Ns/m und damit 25 bis 50-Mal kleiner. Unter Beachtung der mechanischen und resistiven Verluste beträgt die Effizienz der Generatorprototypen 65% bis 75%. Simulationen haben gezeigt, dass die erreichbare Ausgangsleistung für ein Generatorvolumen von 0.25 cm^3 sich zwischen 2 und 25 μW bewegt, je nach Montageort am Körper und Anregung. Dieses Leistungsniveau genügt für viele Sensoranwendungen.

Für die Optimierung der Design Parameter des Generators, wird eine zweistufige Optimierungsmethode präsentiert. Die erste Stufe verwendet elektromagnetische "Finite Elemente Analyse", um die Generator Geometrie mit maximaler elektrischer Dämpfungskraft zu finden. Die zweite Stufe baut auf der gefundenen Geometrie auf und findet die Resonanzfrequenz und die elektrische Last, die zu maximaler Ausgangsleistung führen. Die Optimierungsresultate zeigen, dass die optimalen Werte für einige geometrische Parameter unabhängig vom Generatorvolumen sind. Ausserdem wird ersichtlich, dass die optimale Resonanzfrequenz nicht bei der Grundfrequenz der Bewegung liegt, wie oft angenommen wird, sondern 5 bis 20-Mal höher. Diese führt zu höheren Leistungswerten als bisher angenommen.

Alle Simulationen von Trägheitsgeneratoren in dieser Arbeit verwenden am Körper gemessene Beschleunigungskurven als mechanische Anregung. Die Beschleunigungen stammen von Messungen mit acht Versuchspersonen und neun verschiedenen Messpunkten auf dem Körper. Die betrachtete Bewegung ist "normales Gehen". Somit widerspiegeln die auf den Messungen basierenden Simulationsresultate typische Betriebsbedingungen von körpergetragenen mechanischen Generatoren.

Zusammenfassend zeigt die vorliegende Arbeit, dass effiziente, elektromagnetische Trägheitsgeneratoren mit einem Volumen von weniger als 1 cm^3 möglich sind und eine brauchbare Lösung für die Energieversorgung von Körpersensor-Netzwerken darstellen.

1

Introduction

Body-worn sensor networks have many potential applications in medical monitoring and activity recognition. However, for a large number of sensor nodes, supplying power becomes increasingly difficult. In this chapter, the existing power supply strategies are discussed and compared regarding their suitability to serve as a low-maintenance, long-life body-worn power source. Harvesting ambient mechanical energy using a body-worn generator is considered to be the most promising strategy and is selected as focus of the thesis. Subsequently the research objectives and an overview of the thesis are given.

1.1. Body-Worn Sensor Networks

Body sensor systems (BSN) are increasingly used for data collection, monitoring and context recognition purposes in the areas of medical electronics and wearable computing.

Medical applications: Monitoring of life signs is an important medical application field of BSN. Many chronically ill patients could have a significant increase in their quality of life and life expectancy if certain life signs could be continually monitored during their daily lives. Other medical applications are the detection of unhealthy behaviors and potentially dangerous medical conditions in healthy persons, as well as gathering data of humans during daily life for medical studies. Some examples of the above applications are given in the following list.

- Continually monitoring blood pressure in patients with hypertension can significantly increase medication compliance leading to a significant reduction in blood pressure [49].
- Real-time processing of electrocardiograph traces can be very effective at revealing the early stages of heart disease [52, 124].
- EEG monitoring allows to estimate the alertness of a person [79], as well as to detect epileptic seizures [141].
- Measuring the heart rate variability enables estimation and monitoring of the stress level of a person[77].

Several body-worn [5, 14] and implanted [20, 65, 68] medical sensors and sensor systems capable of executing such monitoring tasks have been reported. A comprehensive overview is provided in [144].

Context recognition applications: Context recognition systems, i.e. sensor systems capable of recognizing and monitoring user activities, have potential applications in maintenance, security, lifestyle, and generally in human-computer interaction. Capabilities demonstrated in research prototypes or commercially available systems include the following.

- monitoring workshop activities [106] (research)
- recognizing American Sign Language [22] (research)

- recognizing various activities of daily living [12] (research)
- measuring heart rate [138] (commercially available)
- estimating running speed and burned calories [48] (commercially available)

Expected trend: In most current body-worn sensor networks the sensor nodes are powered by batteries. This poses no problem since batteries are cheap, readily available and only a limited number of easily accessible sensors have to be powered. However, in the future, a large number of sensor nodes could be highly integrated into the user's outfit or even implanted into the human body and form a body sensor network as schematically shown in Fig. 1.1. This development will render battery replacement more difficult and time-consuming, consequently the envisaged applications will be impractical to use. Hence, other power supply strategies need to be explored. The next section will provide an overview of the possible power supply strategies.

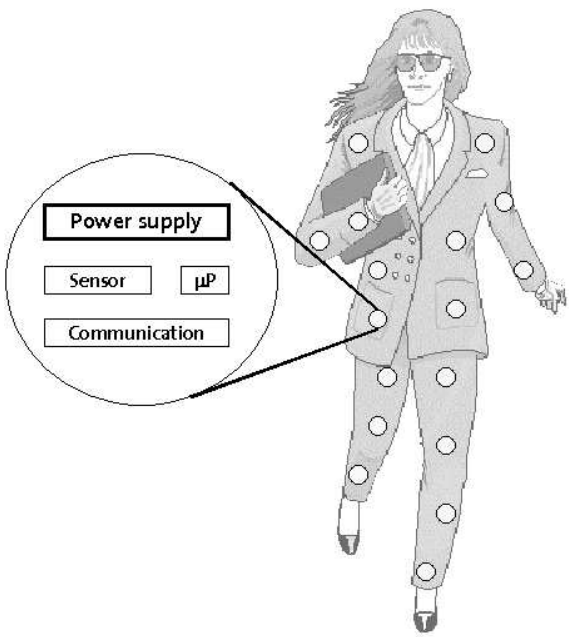

Figure 1.1: *Envisioned body sensor network based on autonomous sensor nodes powered by micro generators.*

1.2. Power Supply Strategies

1.2.1. Overview

Generally, many strategies to supply power to mobile devices exist, some being self-contained and some depending on additional infrastructure. An overview, partitioned into categories, is shown in Fig. 1.2.

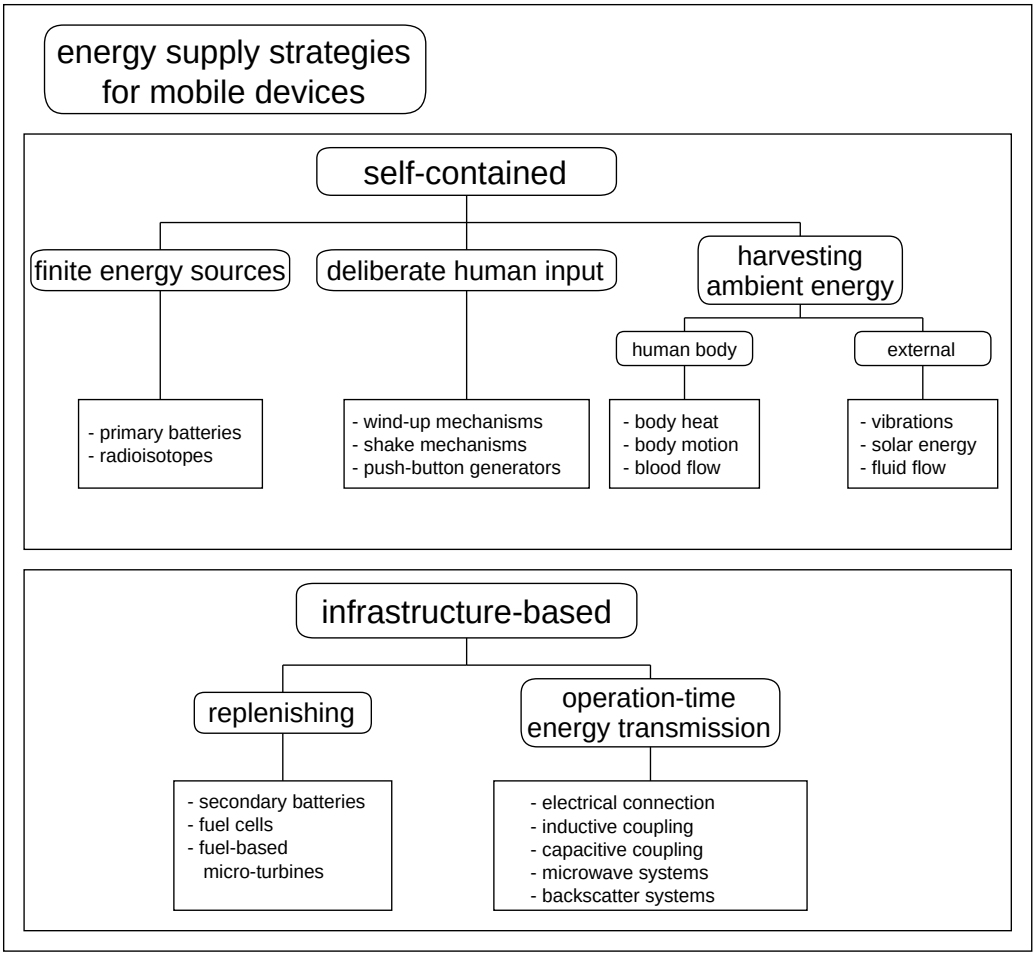

Figure 1.2: *Overview of available mobile power supply strategies. Rectangular boxes contain examples.*

Self-contained power supply strategies include the following.

- *Finite energy sources* provide a fixed amount of energy and must then be replaced. Batteries are a well-known example of such sources. Other examples are radio-isotopes which provide electrical energy in conjunction with a radioactive energy conversion de-

vice. [93, 158] list the available radioisotope-powered energy converters. The converters use the following conversion mechanisms: thermoelectric, thermionic, thermophotovoltaic, direct charging of capacitors with emitted charged particles from radioactive thin films, and directly-charged, self-reciprocating piezoelectric cantilevers [99].

- *Deliberate human input strategies* [165] require the user to deliberately execute certain movements to generate mechanical energy. Mechanisms based on cranking, shaking, pushing, pulling or other movements in conjunction with an electrical generator then convert this mechanical energy to electrical energy. Additional energy is supplied to the system every time the movement is executed, hence the amount of energy is only limited by the lifetime of the system. Such energy supply strategies are used in commercially available mechanical wind-up watches, wind-up radios [51], or flash lights [50].

- *Harvesting ambient energy*, typically known as *energy harvesting* or *energy scavenging* [132, 152, 164] extracts a small amount of energy, small enough not to be disturbing to the user, from energy sources in the local surroundings of the mobile device. Sources include body heat, body motion, vibrations, electromagnetic radiation, solar energy, and fluid flow. As with deliberate human input, the amount of energy is only limited by the lifetime [152], however no conscious effort of the user is required. Existing examples of this strategy are discussed in Sec. 1.3.

Infrastructure-based power supply strategies include the following:

- *Replenishing* relies upon a stationary recharging or refueling facility to recharge a secondary battery, a fuel reservoir or any other energy reservoir of the sensor node. When a secondary battery is used, the connection between battery and recharging facility can be wired or wireless. Many commercial mobile device use a replenishing-based strategy, e.g. cellular phones, PDAs, digital cameras, and electrical toothbrushes.

- *Operation-time energy transmission* uses specialized energy transmission infrastructure, such as inductively coupled power links, during the operation of the mobile device. Typical examples are RFID circuits [47].

In principle, all these strategies can be implemented in a centralized or a distributed structure:

- In a centralized power supply structure, the energy is supplied at one point in the system and is then distributed to the nodes using electrical connections.
- In a distributed structure, every sensor node has an own energy supply unit, no electrical connections are needed between the sensor nodes.

1.2.2. Comparison

In order to compare the different power supply strategies, the requirements for integrated body sensor networks (BSN) need to be defined. BSN will only be practical to use if their power supplies meet the following requirements:

- *Very low or zero maintenance:* The user should not be obliged to spend a significant amount of time every day on maintenance such as recharging or replacing batteries. For example, cellular phones would probably not have gained widespread adoption if one was required to spend several minutes every day to start the recharging process. Another example are current heart-rate measuring chest-belts which typically run on the same battery for several years.
- *Long life-time:* As the sensor nodes are likely to be integrated into clothes, shoes or other worn objects, the life-time of the power supply needs to match or exceed the life-time of the object into which it is integrated.
- *Unobtrusive:* The whole BSN needs to be comfortable to wear and not hinder the movements of the wearer in any way. Consequently, the power supply should also have a comfortable-to-wear shape, small volume and a low weight.
- *Self-contained:* Typically, the BSN needs to be usable in any location and situation, hence the system should not rely on specialized infrastructure.

The implications of these requirements are different for centralized and distributed power supply structures. In centralized structures the

requirements regarding size and maintenance of the power supply are somewhat relaxed, as only one unit is concerned. Consequently, strategies based on finite energy sources or replenishing are feasible. The crucial part in centralized structures is the power distribution wiring: it needs to be implemented in an unobtrusive and robust way: A possibility is to implement such wiring using conductive textiles as reported in [37, 105].

In distributed power supply structures, finite energy sources are only suitable if their life-time exceeds that of the BSN, i.e. if no replacement is necessary during the life-time of the BSN. This is the case for radio-isotope powered generators [93], which are potentially able to operate for 100 years and longer, depending on the half-life of the used radio-isotope. However, acceptance and disposal of such generators may be an issue.

Power supplies relying on deliberate human input are not suitable for BSN as they require regular maintenance by definition. Operation-time energy transmission are not suitable because they restrict the use of the BSN to locations where the appropriate infrastructure is installed.

Energy harvesting is a promising power supply strategy for BSN because of the following unique advantages:

- Energy harvesting generators (EHG) are inherently self-contained.
- Provided, the EHG has a life-time that exceeds the BSN life-time and the mean generated power is higher than the consumed power of a sensor node, then the nodes are able to operate autonomously without any user maintenance.
- Compared to radio-isotope powered generators, cost, disposal, and acceptance are likely to be less of an issue.

1.3. Energy Harvesting Generators

Energy harvesting generators (EHG) extract ambient energy stemming either from the user, e.g. body heat and body motion or from the local environment, e.g. solar energy and electromagnetic waves. Fig. 1.3 shows the ambient energy types suitable for energy harvesting along with examples. The energy types are mechanical energy, thermal energy, and radiant energy.

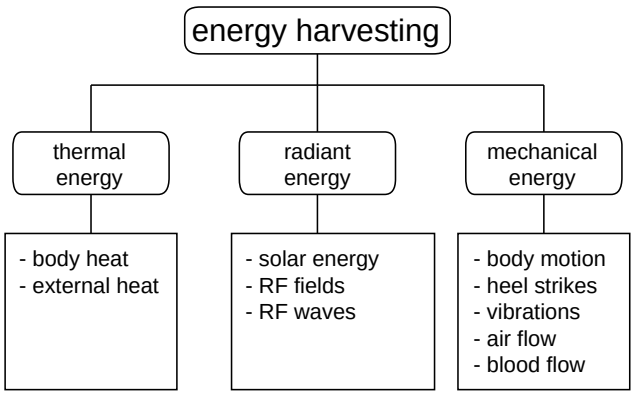

Figure 1.3: *Types of ambient energies suitable for energy harvesting.*

Various energy harvesting generators (EHG) that could be used to power medical and other sensors have been built as research prototypes. Some examples are listed in Tab. 1.1. Current commercially available systems are listed in Tab. 1.3. A comprehensive overview is also provided in [132].

Tab. 1.2 compares the general properties of body-worn generators harvesting thermal, radiant, and mechanical energy. Mechanical generators are considered promising as they have high availability, are independent of environmental conditions and allow relatively unrestricted placement on the human body when compared to the other generator types. For these reasons, body-worn mechanical generators have been studied further in this thesis.

1.4. Research Objectives

This thesis discusses the potential and the limitations of body-worn mechanical generators. The main focus is on linear inertial generators. The following research issues are dealt with:

- *Achievable output power:* Independent from the used energy conversion principle and generator design, there are certain limitations to the electrical output power a body-worn mechanical generator can achieve.
  - What are the main parameters influencing and limiting the output power?
  - How can the achievable output power be estimated independent from energy conversion principle and generator design?

Table 1.1: *Research prototypes of energy harvesting generators.*

Energy type	Conversion mechanism	References
thermal	thermopiles	[21, 39, 54, 82, 85, 142, 167]
thermal	thermo-tunneling	[34]
radiant	solar cells	[94]
mechanical	electro-magneto-hydrodynamic	[160]
mechanical	electrostrictive	[104]
mechanical	piezo-electric	[7, 9, 25, 29, 32, 38, 46, 53, 55, 56, 60, 69, 76, 81, 87, 92, 96, 97, 98, 109, 110, 119, 120, 127, 129, 130, 131, 136, 137, 143, 147, 151, 161, 162, 178]
mechanical	electrostatic	[19, 33, 35, 107, 108, 113, 114, 116, 117, 118, 150, 151, 169]
mechanical	electromagnetic	[2, 3, 15, 16, 17, 18, 26, 27, 28, 40, 41, 42, 43, 57, 58, 66, 67, 72, 73, 74, 75, 78, 90, 92, 95, 100, 101, 102, 111, 118, 121, 153, 155, 156, 174, 177, 179, 180, 181, 182, 183, 184]

  - How does the output power depend on the mounting location of the generator on the human body?

- *Electromagnetic generator architecture:* What electromagnetic topology is most suitable for body-worn generators? What type of bearing is useful to suspend the moving mass?

- *Design optimization:* Body-worn inertial generators are driven by human motion and need to be small and unobtrusive. How can the design parameters of a generator architecture be optimized, given these special requirements and operating conditions.

1.5. Thesis Overview

[1] However, output power varies with generator mounting location and orientation.

Table 1.2: *Comparison of the main types of body-worn generators.*

Property	MG	TEG	PVG
no moving parts	no	yes	yes
available in the dark	yes	yes	no
available indoors	yes	yes	limited
independent of environmental conditions	yes	no	no
unrestricted placement	yes[1]	no	no
packaging requirements	few	thermal contact	opening for light
weight/volume	low/medium	low	low
shape	depends	flat	flat

legend: (MG = mechanical generator, TEG = thermoelectric generator, PVG = photovoltaic generator)

Chapter 2 introduces the topic of body-worn mechanical generators. It discusses their special operating conditions as well as mechanical and electrical system aspects. A special focus is on electromagnetic generators.

Chapter 3 describes the recording of on-body acceleration and the subsequent evaluation. The gathered data serves as driving motion for the simulation of inertial (vibration-driven) generators.

Chapter 4 deals with the estimation of achievable generator output power for human driving motion. The analysis is based on generic generator models and thus independent from fabrication technology.

Chapter 5 presents an architecture for a body-worn inertial electromagnetic generator. An optimization method is presented which allows optimization of all relevant design parameters.

In Chapter 6, the used simulation models are validated through measurements on a fabricated prototype.

Chapter 7 draws conclusions from the conducted work, summarizes the achievements and presents an outlook.

Table 1.3: *Commercially available energy harvesting generators*

System	Energy type	Conversion mechanism	Company	Product	Reference
wristwatch	TH	TP	Citizen	Eco-Drive Thermo	[30]
wristwatch	TH	TP	Seiko	Thermic	[85, 132]
generator	TH	TP	Applied Digital Solutions	ThermoLife	[132]
wristwatch	R	PV	Citizen	Eco-Drive	[30]
wristwatch	M	EM	Oakley	TimeBomb	[128]
wristwatch	M	EM	Seiko	Kinetics	[132]
watch movement	M	EM	ETA	Autoquartz	[132]
watch movement	M	EM	Seiko	AGS	[132]
generator	M	EM	Ferro Solutions	Energy Harvester	[132]
watch movement	M	EM	Kinetron	MGS Watch	[84]
pedal illumination	M	EM	Kinetron	MGS Pedal Illumination	[84]
autonomous switch	M	PE	EnOcean	PTM100	[45, 132]
autonomous switch	M	PE	Lightning Switch	Lightning Switch	[103, 132]

legend: TH = thermal, R = radiant, M = mechanical, TP = thermopile, PV = photovoltaic, EM = electromagnetic, PE = piezoelectric

2

Body-Worn Mechanical Generators

This chapter serves as introduction to the topic of body-worn mechanical generators. First, the special properties of body-worn generators and the available biomechanical energy are discussed. Subsequently, the basic energy conversion stages and the corresponding architectural options are described. Finally, the architectural options are compared and an architecture is selected. For the resulting architecture, a resonant inertial electromagnetic generator, a system model is provided and related work is discussed.

2.1. Introduction

2.1.1. Special Properties of Body-Worn Generators

Body-worn mechanical generators have significant differences to mechanical generators mounted elsewhere, e.g. generators mounted on machines for monitoring purposes, such as the generator presented in [74].

- *Different properties of available mechanical energy:* Generators mounted on a machine will often experience sinusoidal vibrations at high frequencies (above 50 Hz) and low amplitudes (below 1 mm), whereas body-worn generators will be subjected to non-sinusoidal motion, low frequencies (below 30 Hz) and large amplitudes (at least several mm). Evidence for this is reported in [172].

- *Form factor matters:* A body-worn generator needs to be comfortable to wear and unobtrusive.

- *Size and weight are critical:* Size and weight are more critical than in generators mounted on machinery because body-worn generators are only practical if they do not impose a burden on the user.

- *The amount of available mechanical energy is difficult to estimate:* it depends not only on the properties of the human body, such as height and weight, but also on the type and frequency of body movements carried out during a day. In addition, the human body is typically also subjected to external mechanical excitations, e.g. when riding a bus or using a tool.

2.1.2. Available Biomechanical Energy

In this subsection we discuss the amount of biomechanical energy that is available to body-worn generators. The considerations are mainly based on the work of [126]. Similar work is reported in [164]. For simplification, we consider a human body model consisting of rigid segments connected by the joints [185].

For such a body model, the mechanical energy is the sum of the potential and kinetic energies of the segments. By executing a movement, a person performs mechanical work which is composed of the

contribution of all joints. The net mechanical work of one joint is

$$W = \int_0^\theta T \mathrm{d}\theta = \int_0^t T\omega \mathrm{d}t \tag{2.1}$$

where T is the torque, θ is the angle of rotation, ω is the angular velocity and t is time.

For walking motion, [126] estimates, based on the measurement of ground reaction forces and inverse dynamic, that about 2 W of mechanical power each is generated by elbow and should joints, and about 40 to 70 W each by hip, knee and ankle joints.

It is important to note, that the work performed by the muscles can either increase the kinetic energy of the joint or decrease it. The energy is increased, if the muscle torque acts in the same direction as the angular velocity, (defined in [185] as positive work). The energy is decreased, if the muscle is opposing the motion (negative work). In the latter case, the joint muscles are absorbing energy from the motion and convert it to heat.

Hence, the energy harvested by a mechanical generator has contributions of both positive and negative muscle work. This has the following consequences regarding the required muscle work

1. *Positive muscle work:* The harvested power leads to additional work performed by the muscles.

2. *Negative muscle work:* Power that would otherwise be converted to heat in the muscles is converted to electrical power by the generator. This potentially decreases the metabolic energy spent per electrical output energy. In [91, 148], the authors state the hypothesis, that they have observed this effect in a backpack generator based on an oscillating payload and an electromagnetic generator. [126] estimates that negative work constitutes between 11 and 85% of total muscle work.

For energy estimation purposes, it is more prudent to assume the worse case of harvesting positive muscle work because it will generally be difficult to control whether negative or positive muscle work is harvested. Consequently, in order to estimate the energy available to body-worn mechanical generators, only positive work is considered in this thesis: If we assume that less than 1% additionally spent muscle power is not noticeable to the human, then the available mechanical power is about 20 mW per shoulder or elbow joint and about 400 to

700 mW per ankle, knee or hip joint. Assuming < 1 mW required power per sensor node, enough power is available to supply several hundred sensor nodes. As will be shown in this thesis, the available mechanical energy from the above consideration is not the limiting factor for body-worn generators. Rather, limits are imposed by the fraction of this available energy that the generators are able to convert to electrical energy.

2.2. Basic Generator Operating Principle

The energy conversion in mechanical generators takes place in two steps, as illustrated in Fig. 2.1. The two steps are the following:

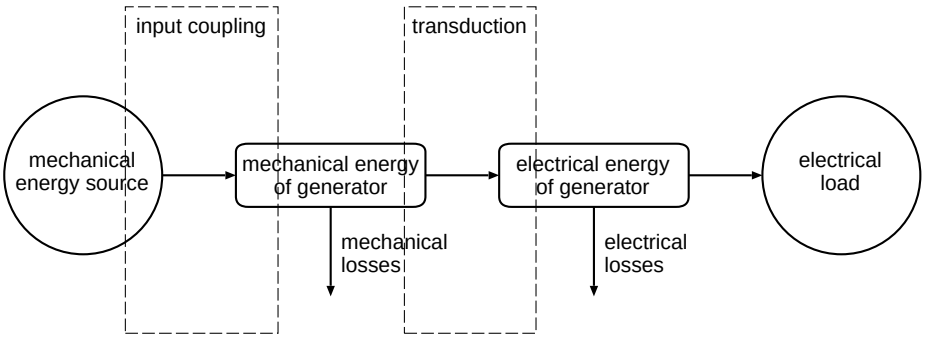

Figure 2.1: *Energy flows in electro-mechanical generators.*

1. *Input coupling:* Mechanical input energy is coupled into the generator system by the application of a coupling force or pressure which either accelerates or deforms an input coupling element. The transferred energy is the work done by the coupling force and is stored in the generator system in the form of kinetic and potential mechanical energy.

2. *Transduction:* The mechanical energy of the generator system is then transduced to electrical energy using an electro-mechanical conversion principle. As a result, a force is produced that counteracts and therefore damps the movement or the deformation of the input coupling element. The transduced energy is the work done by this transduction force.

In a water-turbine, for example, the coupling pressure is the pressure of the flowing water that accelerates the turbine blades, and the

transduction force is the Lorentz force occurring in the electromagnetic generator.

Input coupling and transduction can also occur in the same element. For example, in strain-driven piezo-electric generators, input energy is coupled into the system by straining a piezoelectric element which in turn produces an electric field.

2.3. Input of Mechanical Energy

An overview of the basic architectural options related to input coupling is shown in Tab. 2.1. The listed options are discussed in the following subsections.

Table 2.1: *Overview of basic architectural options of mechanical generator regarding input coupling.*

Property	Options
coupling type	inertial direct
motion of coupling element	linear rotary deformation
restoring force of bearing	linear spring non-linear spring no restoring force
transmission	none gear mechanism other transmission

2.3.1. Coupling Type

There are two different ways to couple mechanical energy into the generator system: *inertial* and *direct* coupling. In Fig. 2.2, each coupling type is illustrated by a generic generator model: Both generator models contain a coupling element m that moves relative to the generator frame during operation. $x(t)$ and $y(t)$ are the absolute positions of coupling element and generator frame, respectively, $z(t)$ is the position of

the coupling element relative to the generator frame. The damper f represents the damping effect of the transduction force.

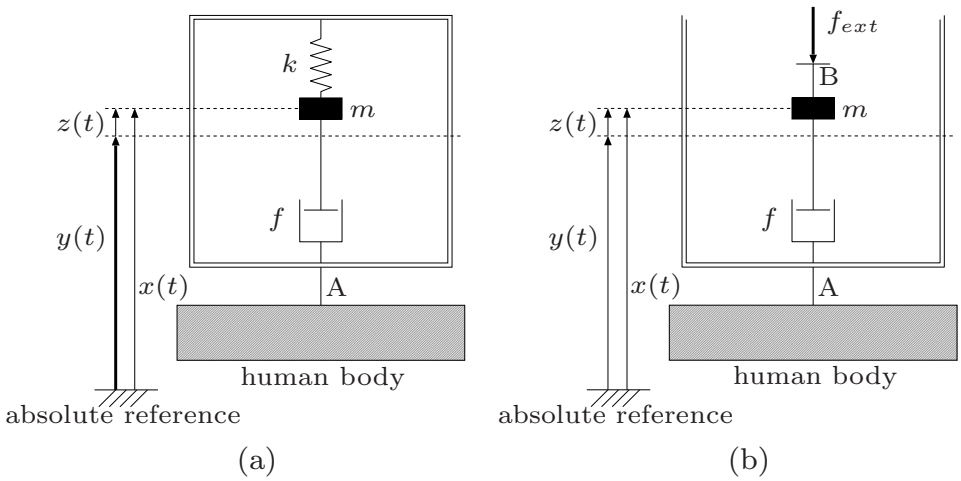

Figure 2.2: *Basic generator models showing the two possible input coupling types: (a) inertial coupling, (b) direct coupling.*

- *Inertial coupling:* These generators, called inertial or vibration-driven generators, are driven by the absolute motion of the generator frame. A basic model is shown in Fig. 2.2(a). The generator has one external mechanical connection, A. The coupling element m is a mass, called proof-mass, that is suspended to the generator frame using a spring-like structure k. When the frame is accelerated, the mass moves relative to the generator frame due to its inertia. Thus, mechanical energy has been coupled into the generator system. The system now contains mechanical energy in the form of kinetic energy of the proof-mass and potential energy of the spring. The coupling force is the inertial force acting on the proof-mass and is hence proportional to both mass and acceleration of the proof-mass. Consequently, the larger the mass the more mechanical power can be coupled into the system. Common examples of inertial generators are the generators used in automatic watches.

- *Direct coupling:* These generators are directly driven by the coupling force. A basic model is shown in Fig. 2.2(b). The generator contains a moving or deformable coupling element m, the coupling force is denoted by f_{ext}. In contrast to inertial generators, a

relative motion between two mechanical connections to the generator, is needed to drive the generator. The two connections are denoted with A and B in Fig. 2.2(b). A larger mass does not necessarily lead to more coupled power. Examples are hydroelectric power plants, where the water pressure puts a turbine into motion. The relative motion is between the water and the fixed turbine shaft.

A comparison of inertial and direct input coupling, summarized of in Tab. 2.2, yields the following observation:

- Inertial generators can be placed on many locations on the human body, whereas directly-coupled generators have severe limitations in this respect. Directly-coupled generators can be placed only at locations on the human body where relative motion is available. Suitable relative motions exist between two body parts or between a body part and a fixed object, e.g. the ground. Examples of body-worn directly-driven generators are shoe-mounted generators, which exploit the relative motion between shoe and ground [157].

- Inertial generators have the disadvantage, that the coupling force is proportional to the proof-mass. Hence, in contrast to directly coupled generators, the damping force of inertial generators is dependent on the size and the mass of the coupling element.

Table 2.2: *Comparison of inertial and directly-coupled generators*

Property	Inertial coupling	Direct coupling
flexible placement on the body	yes	no
coupling force independent of coupling element size	no	yes
coupling force independent of coupling element mass	no	yes

Since for body sensor networks, flexible placement of the sensor nodes and thus of the generators is important, inertial coupling is selected.

2.3.2. Motion of Coupling Element

Mechanical energy can only be coupled into the generator when there is relative motion between coupling element and generator frame or a deformation of the coupling element. Typically, there are three options:

- *Rotary motion:* The coupling elements rotates about a center. The motion can be reciprocating within limited angular displacement or use the full 360°. Rotating coupling elements are used, for example, in generator watches.
- *Linear motion:* The coupling element moves linearly back and forth within a limited displacement range. Linear motion is used in most reported inertial micro-generators. An example of large linear generators are wave energy converters [149].
- *Deformation:* Deformation of a coupling element, e.g. by bending, straining, or compressing, is used in some directly-coupled generators, such as shoe-mounted generators, where the direct compression of the sole generates electrical energy.

Generally, the type of coupling element motion used in body-worn mechanical generator should be chosen according to the properties of the driving motion. For example, wrist-mounted generator watches typically use rotational motion because the wrist movements contain a large rotary component. In contrast, for body-worn generators mounted on linearly moving body parts, such as the trunk, linear coupling element motion is more advantageous.

Regarding body-worn sensor networks, it is assumed that many sensors are mounted on the trunk of the user. Consequently, this thesis focuses on linear coupling element motion.

2.3.3. Restoring Force of Bearing

In order to enable the coupling element to move, a bearing is necessary that supports and guides the coupling element. The bearing may also incorporate a spring-like structure to provide a restoring force. The architectural options are as follows:

- *Linear spring:* In this case, the bearing provides a restoring force that is, up to the elastic limit, linearly dependent on the displacement of the coupling element out of the quiescent position. The

spring force f_s is defined by Hooke's Law:

$$f_s = k \cdot z \tag{2.2}$$

where k is the spring constant and z is the linear or angular displacement of the coupling element away from its idle position. Using a linear spring, the generator may be operated in a resonant mode. If no damping is present, the coupling element oscillates at the natural frequency f_n[1]. The natural frequency, f_n, is defined by:

$$f_n = \frac{\omega_n}{2\pi} = \sqrt{\frac{k}{m}} \tag{2.3}$$

where k is the spring constant and m is the mass of the coupling element. ω_n is the natural frequency in rad/s. Generators containing a linear spring intended for resonant operation are hence called *resonant generators*.

- *Nonlinear spring:* The restoring force may also be a nonlinear function of the displacement. Such spring structures [24] can be designed to let the coupling element snap back and forth between two stable equilibrium positions .

- *No restoring force:* The bearing provides no restoring force as is the typical situation in rotary generators. Linear generators with no restoring force are also possible, however, since the displacement range is inherently limited, end-stop must then be used to constrain the movement of the coupling element. Unless collisions between coupling element and end-stop are elastic or avoided, this leads to additional mechanical losses. An example of a linear generator with no restoring force is reported by Mitcheson et al. in [117].

In this thesis a bearing with a linear spring is used in order to allow resonant operation and to avoid mechanical losses due to frequent end-stop collisions.

2.3.4. Transmission

Some generators contain a mechanical transmission to transform the mechanical energy from a high-displacement, low-force load to low-displacement, high-force load or vice versa to enable the generator to

[1] The natural frequency is also called undamped resonant frequency

work at an efficient operating point. Different kinds of transmissions may be used:

- *Gear mechanism*: In some generators, transmission gears are used to convert between linear and rotary motion or to increase the relative velocity of the motion. For example, in the Seiko AGS generator described in [132], the angular velocity of the rotor is sped up by a gear mechanism to improve the efficiency of the electromechanical energy conversion.
- *Other transmission*: Kulah [90] uses a magnet on a diaphragm, oscillating at the frequency of the input motion, to attract a magnet on a cantilever with a higher resonance frequency. When the diaphragm moves away, the cantilever is released and now oscillates at a much higher frequency. This allows to increase the efficiency of the electromagnetic generator.
- *No transmission*: The mechanical energy is not transformed to another form after it has been coupled into the system.

2.4. Transduction to Electrical Energy

This section discusses architectural options related to the transduction stage in mechanical generators (cf. Fig. 2.1). An overview of the options is shown in Tab. 2.3.

Table 2.3: *Overview of basic architectural options of mechanical generators regarding transduction.*

Property	Options
electrical damping type	velocity damping Coulomb damping other
energy conversion principle	variable capacitance with air dielectric variable capacitance with elastic dielectric direct and converse piezoelectricity electromagnetic induction direct and converse magnetostriction large Barkhausen effect

2.4.1. Electrical Damping Type

As mentioned above, the converted energy is the work done by the transduction force. During energy conversion, the motion of the coupling element is damped by the transduction force. The relation between this damping and the velocity of the coupling element can be used to classify mechanical generators.

- *Velocity damping:* The magnitude of the transduction force is proportional to the velocity of the transducing element. Generators based on this damping type are called velocity-damped generators [115] and can be approximated using electromagnetic or piezoelectric energy conversion principles.

- *Coulomb damping:* The magnitude of the transduction force is constant. Generators based on this damping type are called Coulomb-damped generators [115] and can be approximated using electrostatic energy conversion principles. Coulomb-damped electrostatic generators are either based on a gap-varying parallel plate capacitor in constant charge mode or a sliding-plate capacitor in constant voltage mode.

- *Other damping:* Apart from velocity and Coulomb damping, other damping types are possible.

Coulomb-damped and velocity-damped generators were compared in [115]. Another comparison is presented by the author of this thesis and colleagues in [173], the results of which are shown in Ch. 4.

Note, that the damping type is dependent on the used energy conversion principle, thus arbitrary combinations of damping type and energy conversion principle are not possible.

2.4.2. Energy Conversion Principle

Below, the physical effects used to convert mechanical to electrical energy as well as corresponding generator operation principles are briefly explained, an in-depth discussion is not aimed at. More detailed information can be found in the references given.

Electromagnetic, electrostatic, and piezoelectric generators are compared in Chapter 4. Other comparisons include [140, 152].

Variable capacitance structures with air as dielectric

Variable capacitance structures can generate electrical energy by doing work against an electrostatic force. Generators based on this principle are called electrostatic or capacitive generators.

An electrostatic generator consists of two conductors, e.g. two parallel plates, separated by a dielectric that form a capacitor. To start operation, the capacitor is charged to an initial voltage. An attractive electrostatic force now acts on the capacitor plates. The electrical energy E_e stored in the capacitor is given by

$$E_e = \frac{CU^2}{2} = \frac{Q^2}{2C} \tag{2.4}$$

where C is the capacitance, U is the voltage between the capacitor electrodes and Q is the charge stored on the capacitor plates. If the charge is kept constant (constant charge operation) and the capacitance is decreased, e.g. by increasing the gap between the electrodes, the electrical energy stored on the capacitor increases. The additional energy is equal to the mechanical work done against the electrostatic force. The electrical energy may now be transferred to the load and a new conversion cycle may be started.

The electrostatic generator may also be operated in constant voltage mode. A comparison of the two modes is reported in [113].

Electrostatic micro-generators have been reported as research prototypes in [19, 33, 35, 107, 108, 113, 114, 116, 117, 118, 150, 151, 169].

The main disadvantage of electrostatic generators is that they require a separate voltage source to charge the capacitor. In addition, in most configurations, mechanical stops must be provided to prevent contact of the capacitor electrodes. Frequent collisions of the stops, however, could cause wear-out and reduced life-time as well as increased mechanical damping. In addition, depending on the configuration, electrostatic generator may lead to high voltages between the capacitor plates (several hundred volts), which requires more complex and hence more expensive power electronic devices. However, depending on the implementation, low voltages are also achievable.

An advantage of electrostatic generators is that they can be fabricated using MEMS fabrication processes and thus be integrated more easily with micro-electronics. An example of a MEMS electrostatic micro-generator is reported in [113].

Variable capacitance structures with elastic dielectric

Variable capacitance structures can also be built by sandwiching elastic dielectric such as dielectric elastomers or electrostrictive elastomers between two compliant electrodes [88, 104, 134].

Generators based on such structures are based on the same operating principle as generators based on capacitors with air-gaps and rigid plates. The difference is that, instead of moving rigid capacitor plates, strain is imposed on an elastic material to vary the capacitance. Also, due to the elastic nature of the materials, the acting electrostatic force deforms the structure: Charges of the same polarity within an electrode cause the electrode to expand, charges of opposite polarity cause the material between the electrodes to compress. The deformation is dependent on the square of the applied electric field. This effect is also known as Maxwell Stress effect. In electrostrictive materials, deformation is also caused by the electrostrictive effect. As for the Maxwell Stress effect, the deformation is dependent on the square of the applied electric field. The converse electrostrictive is that the dielectric properties of a material change as a function of its elastic state.

A shoe-mounted generator that converts to electrical energy some of the mechanical energy usually dissipated in the shoe sole is presented in [88, 134]. The generator is mounted in the heel of a boot and its output energy is about 0.8 J per step.

Variable capacitance generators based on dielectric and electrostrictive elastomers have the following advantages [134]:

- *Low elastic modulus and large endured strains:* This allows harvesting energy from many human motions using directly-coupled generators (see Fig. 2.2(b)) without any mechanical transmission. In contrast, directly-coupled generators based on piezoelectric materials usually require a configuration that converts the large-displacement, low-force input into a suitable low-displacement, large-force load on the piezoelectric material.

- *Large elastic energy density:* Compared to piezoelectric materials, elastomers can store a large amount of elastic energy (more than $1\,\mathrm{MJ/m^3}$ [133]).

- *Low fabrication cost:* Due to the low cost of the used materials and simple generator structure, generators based on electrostrictive materials can be fabricated at low cost.

A disadvantage of elastic electrostatic generators is the high voltage requirements of the power processing circuitry (up to several kV).

Direct and converse piezoelectricity

The piezoelectric effect occurs in certain non-conducting crystals and is the ability of a material to produce an electric field when subjected to mechanical strain. The converse piezoelectric describes the deformation of a material when an electric field is applied. Strain and electric field are linearly related. A detailed description of the effect is available in [70].

In piezoelectric generators, a suitable configuration uses the coupled mechanical energy to produce strain in a piezoelectric material. Typically, a piezoelectric bimorph is mounted as a cantilever beam. When the beam is bent, tension is produced on one side and compression on the other side. Consequently, a voltage is generated.

A large number of piezoelectric generators has been presented to the scientific community [7, 9, 25, 29, 32, 38, 46, 53, 55, 56, 60, 69, 76, 81, 87, 92, 96, 97, 98, 109, 110, 119, 120, 127, 129, 130, 131, 136, 137, 143, 147, 151, 161, 162, 178]

Commercially available examples include self-powered push-buttons sold by [45] and [103].

An advantage of a piezoelectric generator is that its conversion principle is based on a self-generating effect. Therefore, no separate voltage source is need for bias. A disadvantage is the difficult miniaturization [152]. Piezoelectric films fabricated using MEMS technologies have usually a significantly reduced piezoelectric coupling [171].

Electromagnetic induction

In electromagnetic generators a time-varying magnetic flux through a coil induces a voltage.

An advantage of electromagnetic generators is, that, using permanent magnets, it is self-generating: no separate energy source is needed.

A major disadvantage is that fabrication using micro-fabrication technologies is very difficult. Also, an electromagnetic generator has an inherently limited efficiency due to the power dissipation in the resistance of the coil. It has been claimed that only voltages of around 100 mV can be induced in a generator of 1 cm^3 volume [152], which is too low for efficient power processing. However, it will be shown, that this does not hold for the generator architecture proposed in this thesis.

A more detailed discussion of electromagnetic generators is presented in Sec. 2.5.

Direct and converse magnetostriction

Magnetostriction, present in ferromagnetic materials, allows interchange of mechanical and magnetic energies [36]. The effect that a material sample changes its dimensions when a magnetic field is applied, is called Joule magnetostriction. The converse effect is called Villari effect: stress induced strain produces a change in the magnetization of the material.

Typically, magnetostriction is only used in sensors, however, power generation is possible. Energy conversion using magnetostriction is achieved in combination with electromagnetic induction: A magnetic circuit provides a DC bias flux in the magnetostrictive material, which is surrounded by a coil. Now, the magnetostrictive material is strained which causes the magnetization to vary. Consequently, the flux through the coil is changed and a voltage is induced.

A generator prototype based on magnetostriction is present by Staley et al. [163].

Large Barkhausen effect

The Barkhausen effect [44] refers to a series of sudden changes in the size and orientation of ferromagnetic domains, that occur during a continuous process of magnetization or demagnetization.

In special configurations, e.g. when the considered material volume has only one ferromagnetic domain that has an anisotropy leading to a preferred magnetization direction, the effect leads to step discontinuities in the hysteresis curve of a material [89]. In this case, the effect is referred to as *Large Barkhausen effect*.

The Large Barkhausen effect is used in so-called pulse wires sensors and in Wiegand wires [123, 145, 146], where the material is magnetized with a permanent magnet. As soon as a certain magnetic field strength is reached, a voltage of up to 3 V is induced in a sensor coil, which is, in fact, not dependent on the rate of change in the magnetic field.

It is possible to construct generators based on pulse-wires [146]. However, only about 70 nJ are generated per pulse.

2.5. Resonant Inertial Electromagnetic Generators

2.5.1. Motivation

This thesis focuses on resonant inertial electromagnetic generators with linear proof-mass motion for the following reasons:

- *Resonant operation:* A bearing with linear spring functionality and thus a resonant generator system is chosen to avoid mechanical losses due to end-stop collisions.
- *Inertial coupling:* The inertial input coupling is selected because it allows more flexible generator placement on the human body compared to directly coupled generators.
- *Electromagnetic conversion principle:* As shown in Chapter 4, electromagnetic inertial generators potentially have a higher achievable output power than other generators, if the proof-mass is allowed an amplitude of above 200 to 800 μm.

2.5.2. Energy Conversion Principle

Electromagnetic induction

Electromagnetic generators use electromagnetic induction to produce a voltage.

Faraday's law states that the electromotive force (EMF) produced along a closed path is proportional to the rate of change of the magnetic flux through any surface bounded by that path.

$$\oint_{\partial A} \vec{E} \mathrm{d}\vec{l} = -\frac{\partial}{\partial t} \int_A \vec{B} \mathrm{d}\vec{A} \tag{2.5}$$

where A, ∂A are the area and its boundary, E is the electric field, B is the magnetic flux density and t is time. With

$$u_{ind} = \oint_{\partial A} \vec{E} \mathrm{d}\vec{l} \tag{2.6}$$

$$\phi = \int_A \vec{B} \mathrm{d}\vec{A} \tag{2.7}$$

the same law can be written as:

$$u_{ind} = -\frac{\mathrm{d}\phi}{\mathrm{d}t} \tag{2.8}$$

where u_{ind} is the induced voltage and ϕ is the magnetic flux.

Generator structure

In an electromagnetic generator, a voltage is induced by a time-varying magnetic flux $\phi(t)$ through a coil, typically called armature coil. The varying flux is produced by the relative motion between a moving part, called translator, and a stationary part, called stator. For example, a magnet that moves relative to a coil will induce a varying flux in the coil. However, the translator can also be the armature coil or a soft-magnetic element.

The translator is suspended to the generator frame by a bearing that provides a restoring force proportional to translator displacement. As mentioned previously, this allows resonant operation of the generator.

2.5.3. System Model

A lumped-parameter model of a linear inertial electromagnetic generator is shown in Fig. 2.3. The mechanical and the electrical aspects are modeled by the subsystem on the left, and by the subsystem on the right, respectively. The system input is the acceleration $\ddot{y}(t)$ of the generator frame. The system output is the electrical power dissipated in the load R_l.

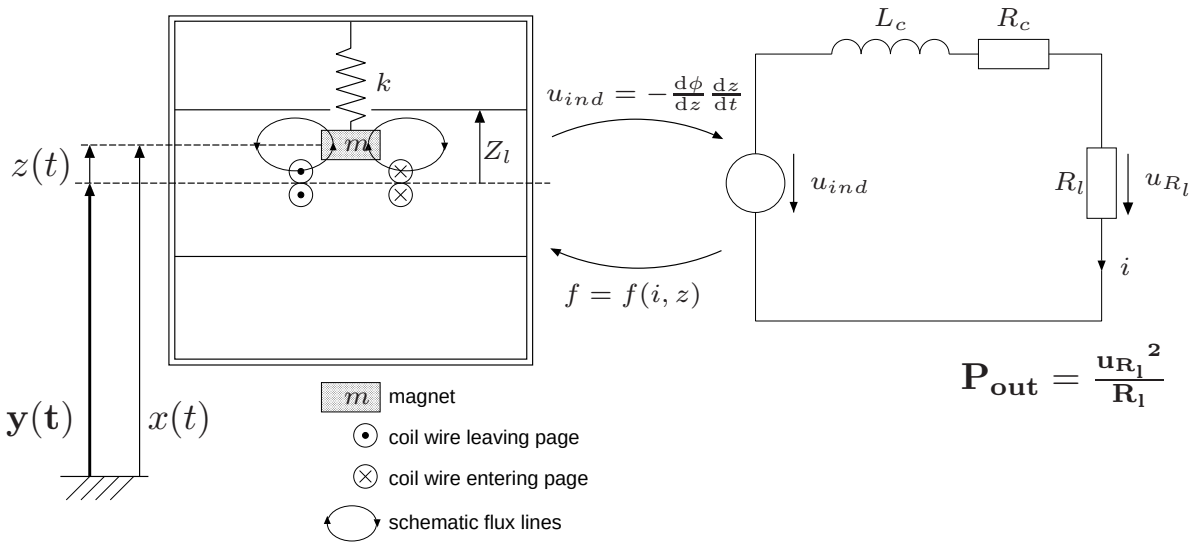

Figure 2.3: *Lumped parameter model of an electromagnetic generator (mechanical sub-model on the left, electrical sub-model on the right).*

The mechanical sub-system uses the following variables: spring constant k, translator mass m, translator displacement limit Z_l. x and y

are absolute translator position and absolute generator frame position, respectively. z is the position of the translator relative to the generator frame. x, y, and z are related by:

$$x = y + z \tag{2.9}$$

The electrical sub-system uses the following variables: coil inductance L_c, coil resistance R_c, and load resistance R_l.

The two sub-systems are coupled as follows. The translator motion leads to time-varying flux $\phi(t)$ in the coil. Consequently, a voltage is induced and a current i flows through the coil. At the same time, the coil current causes an electromagnetic force f which opposes and hence damps the motion of the translator. Therefore, this force is called electrical damping force.

The inductance L_c will be neglected in the following calculations because its influence is likely to be marginal. Evidence for this assumption is given by considering the coil reactance: The coil reactance X_c (imaginary part of coil impedance) is defined as:

$$X_c = \omega L_c \tag{2.10}$$

where ω is the frequency in rad/s. Since the generator is driven by human motion, the highest relevant frequencies of z will be below 25 Hz (see Subsec. 3.3.2). For a (very large) coil inductance of 0.5 H and a frequency of 25 Hz, the reactance X_c is only 79 Ω which is likely to be small compared to the coil resistance. Consequently, the self-induced voltage of the coil will be small compared to the resistive voltage drop across the coil.

Generator force capability

For the force computation we neglect the coil inductance and mechanical losses. The sum of dissipated electrical power and extracted mechanical power must then be zero in accordance with energy conservation:

$$f \cdot \dot{z} + u_{ind} \cdot i = 0 \tag{2.11}$$

Here, f is the damping force, $\dot{z}$ is the translator velocity, u_{ind} is the induced voltage, and i is the current flowing through the coil.

$$f \cdot \dot{z} = -u_{ind} \cdot i = \frac{\mathrm{d}\phi}{\mathrm{d}z} \cdot \frac{\mathrm{d}z}{\mathrm{d}t} \cdot i = \frac{\mathrm{d}\phi}{\mathrm{d}z} \cdot \dot{z} \cdot i \tag{2.12}$$

Hence, f becomes

$$f = \phi_z(z) \cdot i \tag{2.13}$$

where $\phi(z)$ is the flux through the stator coil for a given translator position z, and $\phi_z(z)$ is the flux gradient with respect to z.

For a resistive load R_l, the current i becomes

$$i = \frac{u_{ind}}{R_c + R_l} = -\frac{\frac{\mathrm{d}\phi}{\mathrm{d}z}\frac{\mathrm{d}z}{\mathrm{d}t}}{R_c + R_l} \tag{2.14}$$

and the force is

$$f = -\frac{\phi_z^2}{R_c + R_l} \cdot \dot{z} \tag{2.15}$$

The force is proportional to the translator velocity $\dot{z}$. Thus, a force to velocity ratio $D(z)$ can be defined:

$$f = -D(z) \cdot \dot{z} \tag{2.16}$$

$$D(z) = \frac{|f|}{|\dot{z}|} \tag{2.17}$$

$D(z)$ is computed by:

$$D(z) = \frac{\phi_z^2}{R_c + R_l} \tag{2.18}$$

Note, that D is generally dependent on the translator position z.

Using the definitions

$$\alpha = \frac{R_l}{R_c} \tag{2.19}$$

$$\hat{D}(z) = \frac{\phi_z^2}{R_c} \tag{2.20}$$

the force velocity ratio can be rewritten as

$$D(z) = \frac{\hat{D}(z)}{1 + \alpha} \tag{2.21}$$

Note that $\hat{D}$ is independent from the load and can thus be used to describe the ability of the generator to provide electrical damping force. Therefore, $\hat{D}$ will be called *force capability* in this thesis. The load R_l can be used to tune the force velocity ratio $D(z)$ in the range $[0, \hat{D}(z)]$: For open-circuit operation ($R_l \to \infty$, $\alpha \to \infty$), the force velocity ratio $D(z)$ becomes 0, for short-circuit operation ($R_l = 0$, $\alpha = 0$) it is $\hat{D}(z)$.

System equations

In order to model the system, the translator is considered as mass point and its motion as purely one-dimensional. Thus, the system has one degree of freedom. Then, the *Principle of d'Alembert* is applied. This principle states that the sum of all forces (including inertial forces) acting on a moving mass point must be zero. The forces on the mass are:

- the spring force $F_s(t) = -k \cdot z$ (following Hooke's law)
- the electrical damping force $f = -D\dot{z}$
- the inertia force $F_a(t) = -m \cdot \ddot{x}$

where k is the spring constant, z is the position of the translator relative to the moving generator frame, m is the mass of the translator, and $\ddot{x}$ is the absolute acceleration of the translator. Applying the *Principle of d'Alembert* one gets:

$$F_{res} = \sum_i F_i = 0 \tag{2.22}$$

$$F_s + f + F_a = 0 \tag{2.23}$$

$$-m\ddot{x} - D\dot{z} - kz = 0 \tag{2.24}$$

inserting (2.9) and dividing both sides of the equation by the mass we get:

$$-m\ddot{y} - m\ddot{z} - D\dot{z} - kz = 0 \tag{2.25}$$

$$m\ddot{z} + D\dot{z} + kz = -m\ddot{y} \tag{2.26}$$

$$\ddot{z} + \frac{1}{m} \cdot D\dot{z} + \omega_n^2 z = -\ddot{y} \tag{2.27}$$

where ω_n is the natural angular frequency of the system as defined by (2.3). Inserting (2.21), the system equation becomes:

$$\ddot{z} + \frac{1}{m} \cdot \frac{\hat{D}}{1+\alpha} \cdot \dot{z} + \omega_n^2 z = -\ddot{y} \tag{2.28}$$

where α is the ratio of load to coil resistance as defined by (2.19).

2.5.4. Generated Power

As mentioned in Sec. 2.2, the transduced energy is equal to the work done by the electrical damping force. Thus, the mean converted power $\overline{P_{conv}}$ for a given time interval T is:

$$\overline{P_{conv}} = -\frac{1}{T}\int_0^T f \cdot \dot{z}\,\mathrm{d}t \tag{2.29}$$

Inserting (2.17) and (2.21), the equation becomes:

$$\overline{P_{conv}} = \frac{1}{T}\int_0^T D(z)\,\dot{z}^2\mathrm{d}t \tag{2.30}$$

$$= \frac{1}{T}\int_0^T \frac{\hat{D}(z)}{1+\alpha}\,\dot{z}^2\mathrm{d}t \tag{2.31}$$

Here, the convention is used, that generated electrical power leads to a positive value of $\overline{P_{conv}}$.

As electrical power is lost through dissipation in the coil resistance, the power available to the load $\overline{P_{out}}$ is less than $\overline{P_{conv}}$:

$$\overline{P_{out}} = \frac{R_l}{R_l + R_c}\cdot\overline{P_{conv}} \tag{2.32}$$

$$= \frac{\alpha}{1+\alpha}\cdot\overline{P_{conv}} \tag{2.33}$$

$$= \frac{\alpha}{(1+\alpha)^2}\cdot\frac{1}{T}\int_0^T \hat{D}(z)\,\dot{z}^2\mathrm{d}t \tag{2.34}$$

Here, the electrical efficiency η_{el} is:

$$\eta_{el} = \frac{R_l}{R_l + R_c} = \frac{\alpha}{1+\alpha} \tag{2.35}$$

2.5.5. Effects of Static Acceleration

Static acceleration, i.e. constant acceleration, can be caused by motion (e.g. the centrifugal acceleration in a rotary movement has a DC component) or by gravity. For linear resonant generators, i.e. linear inertial generators with a spring bearing, static acceleration affects the quiescent position of the translator within the frame, thus lowering the possible amplitude of relative translator-to-frame motion and consequently lowering the generated power. For a given static acceleration,

A_{DC}, the quiescent position, z_{DC} is easily calculated:

$$kz_{DC} = mA_{DC} \tag{2.36}$$

$$z_{DC} = \frac{m}{k}A_{DC} \tag{2.37}$$

$$z_{DC} = \frac{A_{DC}}{\omega_n^2} \tag{2.38}$$

where k is the spring constant, m is the translator mass, and ω_n is the natural angular frequency. Note, that for a given natural frequency, the quiescent position is independent from the translator mass. Fig. 2.4 shows the quiescent position as a function of the natural frequency for a static acceleration of 1 g. The quiescent position and hence the loss in available translator motion amplitude is only below 1 mm for natural frequencies above 16 Hz.

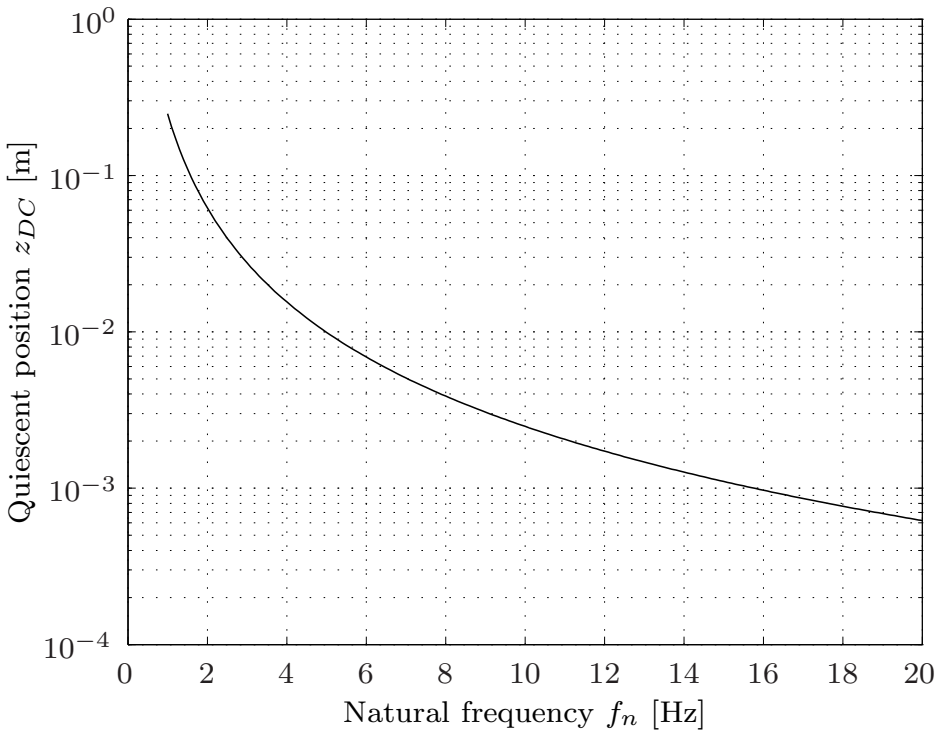

Figure 2.4: *Quiescent position, z_{DC} of translator as a function of the natural frequency, f_n, of the generator for a static acceleration of 1 g.*

Ideally, static acceleration should be compensated out in order to maximize the possible amplitude of relative translator motion. Whereas in electrostatic generators this is possible by applying an offset force, it is impossible to do with a purely electromagnetic generator. This

means, that linear inertial electromagnetic generators should have an orientation on the human body with little static acceleration to avoid lowering the available translator amplitude.

2.5.6. Architectural Options

This section briefly discusses the architectural options regarding various aspects of electromagnetic generators. A more detailed discussion of different generator architectures is available in [10].

Field generation

The magnetic field required for generator operation can be set up in different ways: by permanent magnets or by coils, called field coils, fed with current. Field coils are used in induction machines (asynchronous machines) as well as in field wound synchronous machines. For micro-generators, permanent magnet (PM) topologies are more interesting because they allow the generator to startup from zero stored energy. Also, additional resistive losses are avoided. Therefore, in this thesis, only PM generators are considered.

Generator types

There are three possible generator types

- *Moving magnet type:* The varying flux is induced by moving magnets, the coil is stationary.
- *Moving coil type:* Magnets and iron are stationary, the coil is moving.
- *Moving iron type:* Magnets and coil are stationary. A moving iron varies flux path and flux density leading to a varying flux through the coils.

A moving coil generator is not suited for a long life-time micro-generator, because electrical connections have to be made to a moving part. The resulting wear can lead to device failure. Moving iron and moving magnet generators both have the advantage of not having connections to the moving part. However, the moving magnet generator uses the magnet mass as inertial mass, whereas in moving iron generators, the magnet mass has no useful function, but still adds to the total generator weight.

Translator cross-section

Most linear electromagnetic generators have a translator with either a rectangular or a circular cross-section.

Flux lines

Typically, the magnetic flux lines are mainly located in one or several parallel planes. In some topologies these planes are parallel to the direction of translator motion, with the generators called linear flux machines (LFMs) or perpendicular to it, with the generators called transverse flux machines (TFMs). TFMs are inherently three-dimensional, which renders simulation more time-consuming and fabrication more difficult. LFMs, however, can be designed using rotation-symmetry.

Soft-magnetic material

Often, soft-magnetic material is used to guide the magnetic flux and thus avoid leakage flux, as well as to increase the magnetic flux density. Typically, the armature coils are wound about or surrounded by soft-magnetic material, which is sometimes called *magnetic core* or *back-iron*.

2.6. Related Work

2.6.1. Generators

Linear inertial electromagnetic micro-generators with a volume below several cubic centimeters have been presented by the following research groups:

- Boise State University, Idaho, USA [153]
- Canon Inc., Japan & University of Warwick, U.K. [118]
- Chinese University of Hong Kong, China [26, 27, 28, 95, 100, 101, 102]
- MIT, U.S.A. [2, 3]
- National Tsing Hua University, Taiwan[67]
- Seoul University, Korea [78]

- Sheffield University U.K. [155, 156, 181, 182, 183, 184]
- Southampton University, U.K. [15, 16, 17, 18, 41, 42, 43, 57, 58, 72, 73, 74, 75]
- Southampton University, U.K. & Tyndall National Institute, Ireland [16, 17, 18]
- University of Michigan, U.S.A. [90]

Most of these generators have only been intended or demonstrated for sinusoidal driving motions of 50 Hz and above. Human body motions, however, are far from such conditions. Kulah et al. [90] have presented a generator design specially intended for low frequency driving motion, however so far, only an initial prototype with 4 nW output power has been demonstrated. [3] has considered human motion but not presented an implementation.

One of the contributions of this thesis is the design and evaluation of an electromagnetic inertial generator with a special focus on the suitability for human body driving motions.

2.6.2. Optimization Methods

[177] presents an optimization method for linear generators based on lumped magnetic circuit analysis. However, the architecture used is different from the one in this thesis.

In [176] several linear generators architectures have been optimized for maximum force capability based on approximate analytic solutions of the magnetic field. Also here, the architecture of this thesis is different.

The architecture used in this thesis is based on the one presented by Baker et al. [10, 11]. However, Baker uses only a rough approximation to compute the force capability for the optimization of the architecture, whereas in this thesis, finite element analysis is used.

In addition, the optimization method proposed in this thesis also takes into account the characteristics of human body driving motions.

3

Measurements and Evaluation of On-Body Acceleration

In order to have input data for the simulation of body-worn generators that represents typical human motion, acceleration data from humans during tread-mill walking has been gathered. This chapter describes the instrumentation and the procedures used as well as the properties of the measured acceleration waveforms.

3.1. Introduction

3.1.1. Motivation

In Subsec. 2.1.2, literature has been discussed that estimates the amount of biomechanical energy available to body-worn generators. The discussed work is based on the estimation of the torques acting on the joints. While this gives an indication of how much energy is available, it does not provide any information about how much mechanical energy can be coupled into an inertial generator and converted to electrical energy. This is due to the fact, that the inertial coupling of mechanical energy is dependent on the properties of the acceleration waveform at the location where the generator is mounted. Hence, to estimate the performance of body-worn inertial generators, it is necessary to know these properties at given points on the human body for typical human movements.

Most existing work has approximated accelerations on the human body as sinusoids with a frequency of 1 to 2 Hz. However, as will be shown in this chapter, the acceleration of body motion is characterized by non-sinusoidal waveforms, low frequencies (below 30 Hz) and large position amplitudes.

For this thesis, a total of 216 acceleration measurements at several points on the human body and for several subjects have been carried out using triaxial accelerometers. In this chapter, the measurement procedure as well as the properties of the measured accelerations are discussed. In Chapter 4, an estimation of inertial generator performance based on the acquired acceleration data is presented.

3.1.2. Measurement Scenario

The measurement scenario, i.e. the type of motion studied and the measurement duration, should allow good reproducibility and be close to the conditions of envisioned micro-generator applications. As comprehensive acceleration measurements during all possible activities of daily living are not feasible, a set of typical activities needs to be selected. In this thesis 'Walking' has been selected for two reasons:

- Walking constitutes a substantial part of the total daily energy expenditure for most people ([1, 23, 154]).
- By using a tread-mill, the measurement conditions are well-defined.

3.2. Measurements

3.2.1. Instrumentation

A custom-made wearable sensor system, *PadNET* [80] (cf. Fig.3.1), has been used to acquire the acceleration signals.

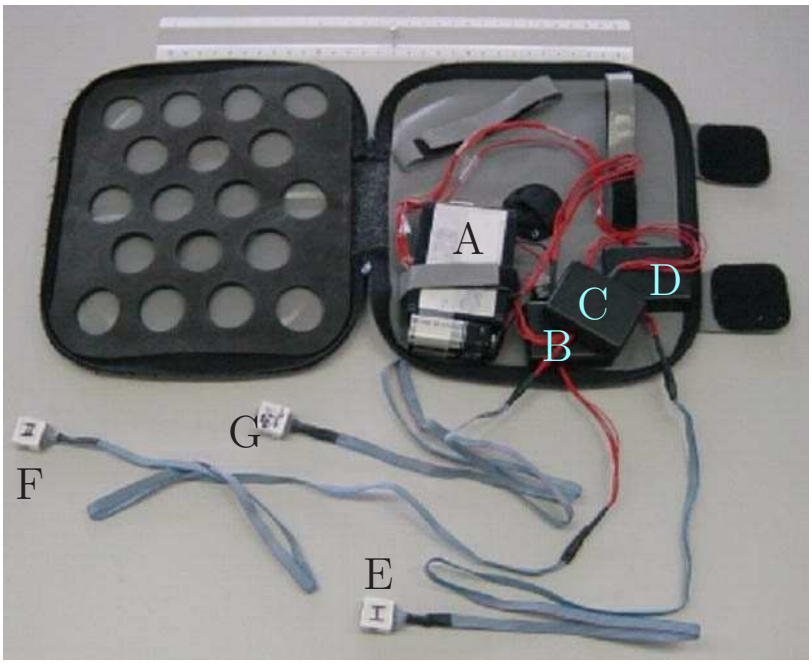

(a)

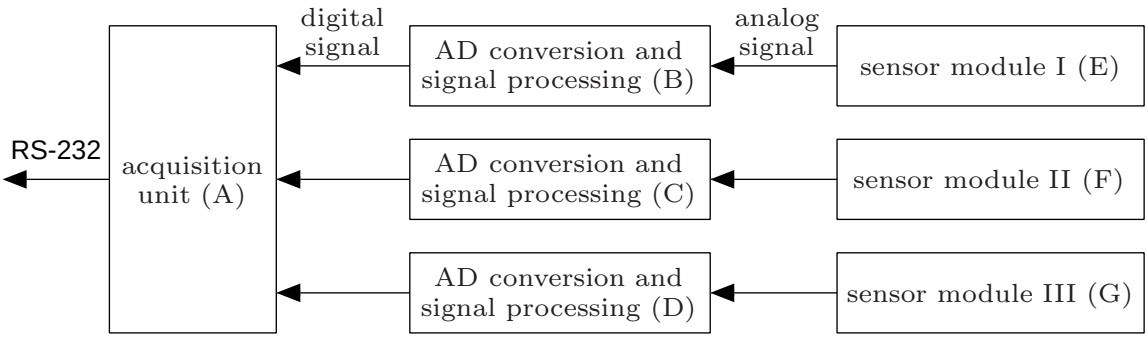

(b)

Figure 3.1: *Sensor System 'PadNET' [80] (a) picture, (b) schematic drawing*

The system consists of three tri-axial sensor modules based on ADXL210E (range ±10g) and ADXL202E (range ±2g) sensors [4], *i.e.* the system is able to record acceleration from all 3 axes from 3 independent locations at a time. The ADXL sensors measure AC and DC

acceleration, hence when the sensors are held still and aligned with the gravity vector, the output will correspond to 1 g.

Two ADXL sensors packaged in a small, light-weight PVC box form one sensor module. The sensor modules weigh less than 5 g, which is substantially less than typical commercial 3D acceleration sensors [86].

The acceleration signals are filtered by an active second-order RC low pass filter (f_{-3dB} = 55Hz) before being sent over RS-232 to an iPAQ 3660 Pocket PC which records the data with a sampling rate of 150 Hz. This configuration is adequate since, according to [8], 99% of the force signal power of human gait is typically contained in the frequency band below 15 Hz.

3.2.2. Mounting of Accelerometers

Two main methods exist to mount accelerometers on a human body: the sensors can be mounted on the skin-surface or directly attached to the bone through a surgical procedure [83]. In a body-worn sensor network most sensors are likely to be attached on the skin or integrated into the users outfit, therefore skin-mounted sensors are used in this thesis.

The sensor modules are tightly fastened to the body using elastic straps with velcro ends, as shown in Fig. 3.2 and Fig. 3.3, to ensure that the sensor module closely follows the body motion. As one sensor modules has a weight of only 5 g, and the expected maximum acceleration is less than 100 ms^{-2} [125], the load of the straps is below 0.5 N. This load can be handled by the used straps.

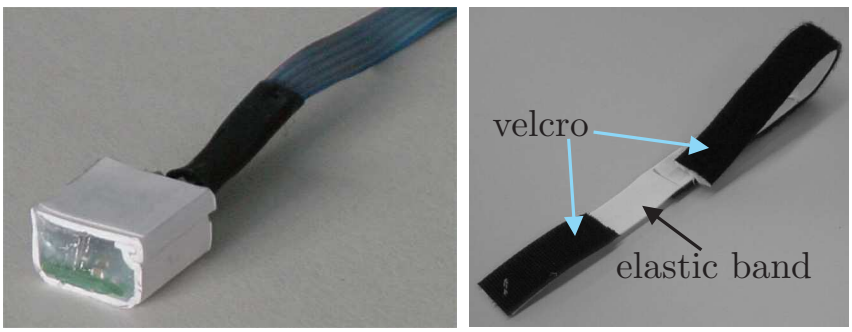

(a) (b)

Figure 3.2: *(a) Sensor module, (b) strap used to fix sensor modules to body.*

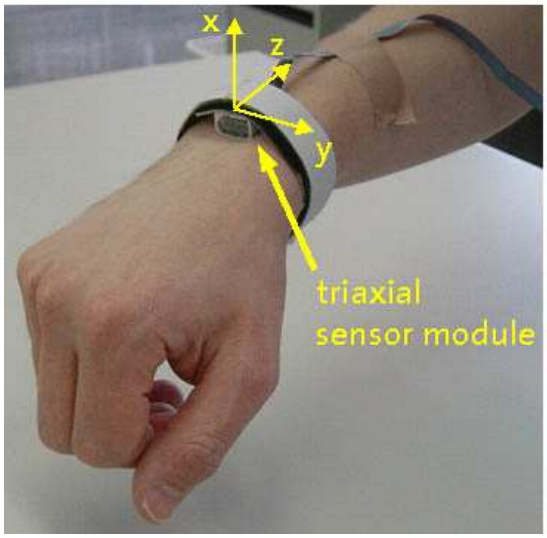

Figure 3.3: *Sensor module mounted on wrist.*

The signal wires are fixed to the skin using medical tape to minimize their mechanical influence (cf. Fig. 3.3). The sensor modules are attached to the nine locations shown in Fig. 3.4.

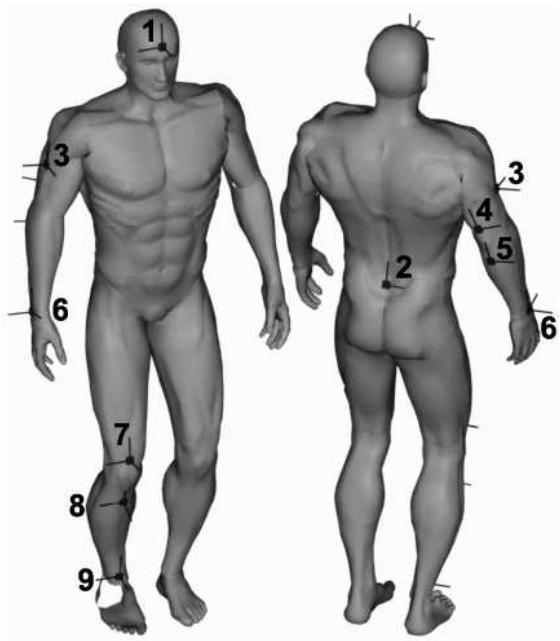

Figure 3.4: *Locations of measurement points on test subject.*

3.2.3. Measurement Method

Eight men are used as test subject (age: 27.3 ± 2.5years, weight: 71.6 ± 7.4 kg, height: 179 ± 6.5 cm (mean± s.d.)). The test subjects are wearing normal walking shoes and are asked to walk normally on a treadmill for 60 seconds while the sensor system is recording the accelerations . The treadmill is running at constant 4 km/h (cf. Fig. 3.5). Three independent measurements are carried out for every measurement point and every test subject. As the used sensor system is only able to record accelerations from 3 locations at a time, 3 measurement runs are needed to obtain one dataset for the whole body. In total, 216 acceleration waveforms of 60 seconds length have been recorded.

Figure 3.5: *A subject walking on the treadmill during a measurement.*

3.3. Evaluation

The following convention is used for the sense of acceleration in the following plots: If the sensor is accelerated in the positive direction of one axis then the acceleration value for that direction will be positive.

3.3.1. Time Domain

In Fig. 3.6 exemplary acceleration waveforms of one subject are shown for all nine measurement locations and three sensor axes. Note that the vertical axis for all measurements has a DC component of about $9.81\,\mathrm{m/s^2}$ which is due to gravity. The entire waveforms of 60 seconds have been segmented into fundamental periods, which yields about 48 segments, the segments have then been plotted overlaid. A fundamental period contains a time period equivalent to two consecutive impacts of the same foot on the floor. It can be seen that all segments have a similar shape. Note, that since the ground reaction force has not been measured, the start of a segment does not correspond to a particular time point within a step phase, e.g. heel impact.

3.3.2. Frequency Domain

In Fig. 3.7 the one-sided magnitude spectra of the waveforms from Fig. 3.6 are plotted. The dominant spectral lines are below 10 Hz. The mean bandwidth containing 95% of the energy of the AC acceleration signal is shown for each location in Fig. 3.8. The vertical bars indicate standard deviation. The bandwidth values have been averaged over the 8 subjects, 3 axes, and 3 independent measurements per location. The mean bandwidths for the upper body, containing locations 1, and 3-6 are below 10 Hz, while for the lower body, containing locations 2, and 7-9 they are between 10 Hz and 25 Hz.

Acceleration waveforms on locations 1, and 3-6 on the upper body have lower bandwidth, because some energy of the foot-ground impacts is absorbed by the body before it reaches the upper body. In addition, head, (location 1), shoulders and upper arms (locations 3-5), are moved a shorter distance during a step than the legs (locations 7-9).

The standard deviations of the bandwidth for locations 1-2 and 6-9 are rather large, up to about 60% of the mean values. The possible reasons are variations in height, body weight, walking style, and to a lesser extent, variations in footwear properties.

It has also been analyzed how the frequency spectrum of the measured acceleration waveforms varies over the 60 seconds duration of one recording. For this purpose a spectrogram (spectra of shifted windows of a waveform) has been computed. Hanning windows of 4 seconds length and 50% overlap have been used to reduce spectral leakage. An exemplary spectrogram is shown in Fig. 3.9. It can be seen that the frequency spectrum is approximately constant over time.

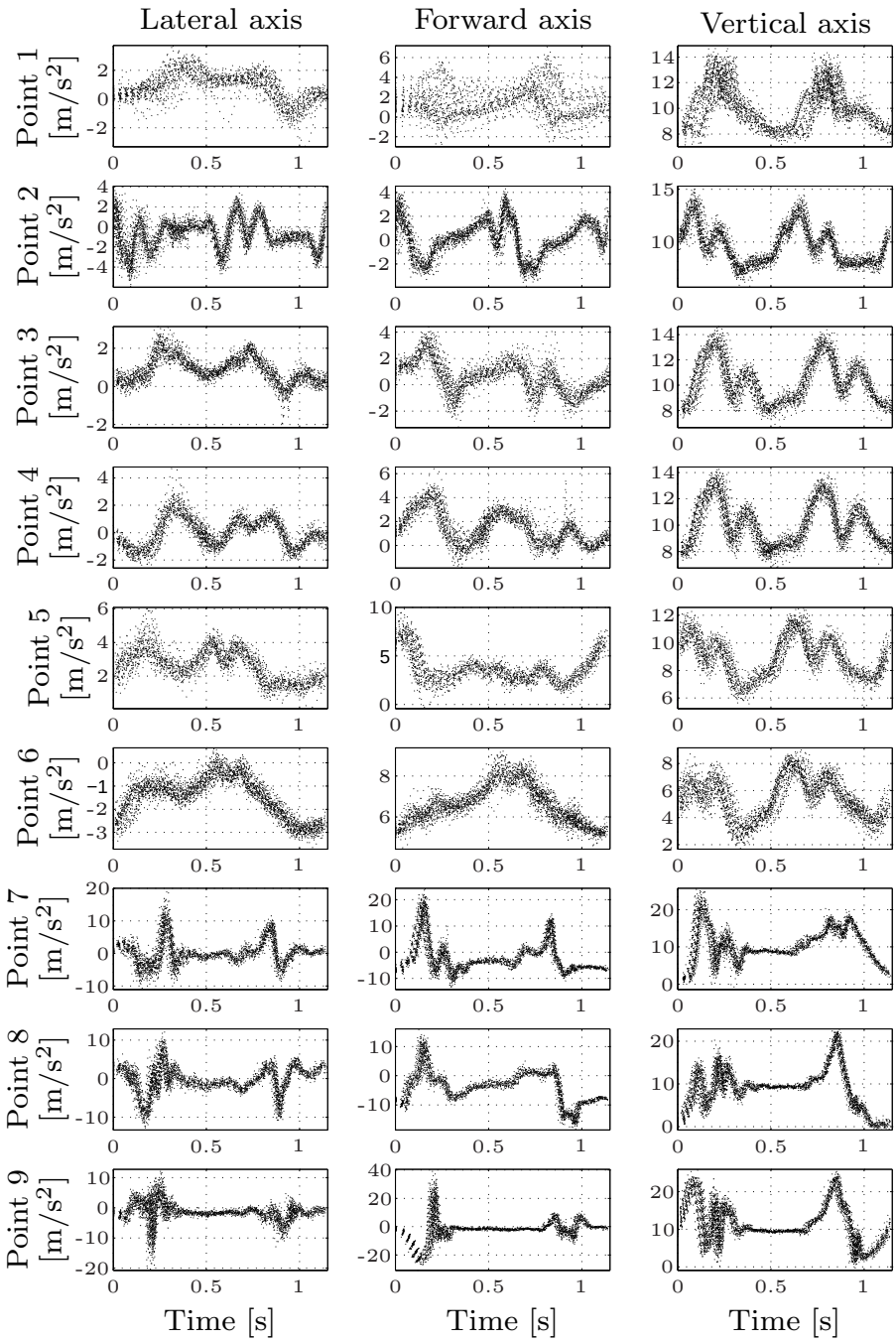

Figure 3.6: *Exemplary acceleration waveforms of one subject. The entire recording of 60 seconds is partitioned into about 48 segments, each of which has a duration corresponding to one step of the right foot. The segments are plotted overlaid. The point numbers indicate the location of the measurement points on the human body as shown in Fig. 3.4.*

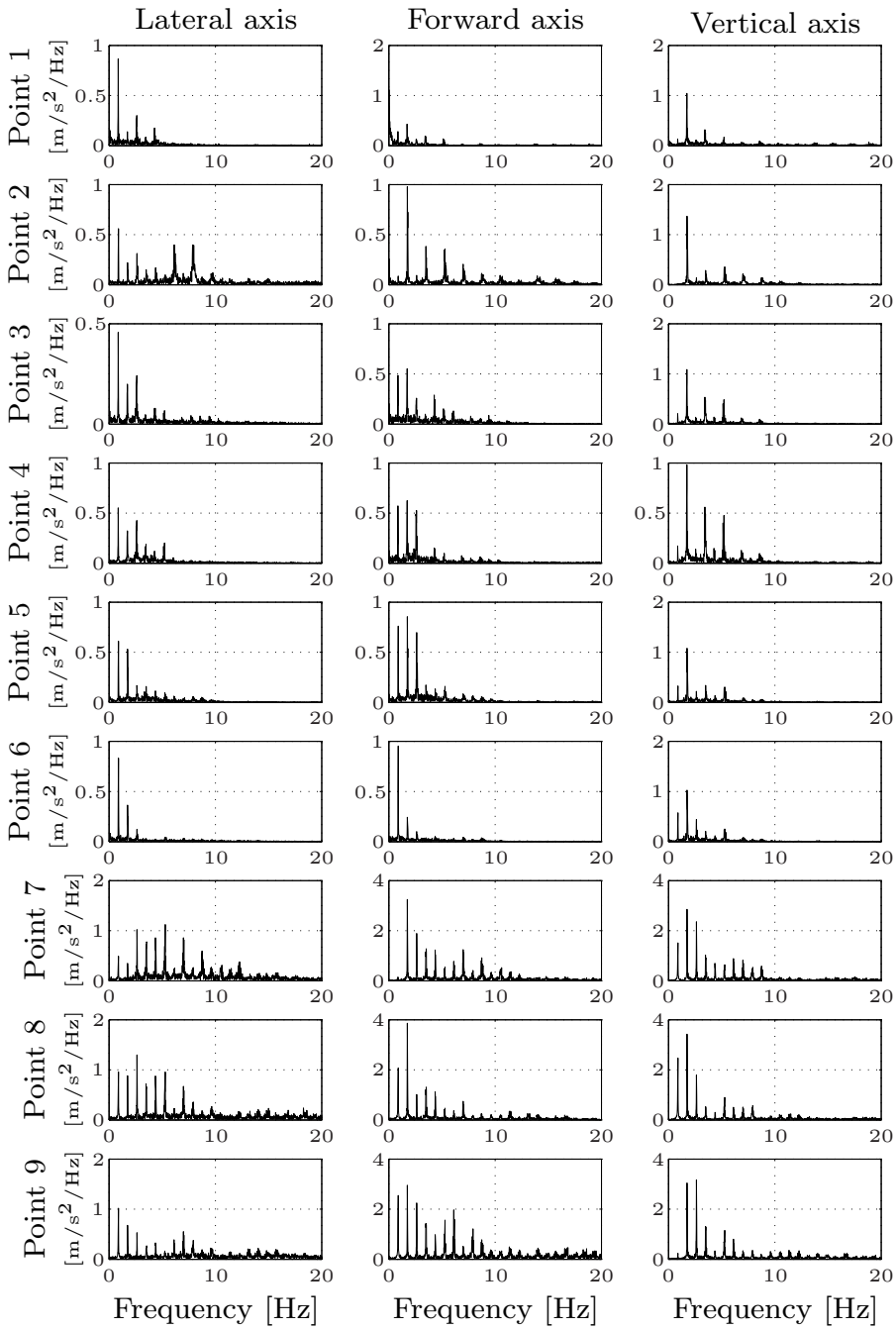

Figure 3.7: *Frequency spectra of measured acceleration waveforms. The point numbers correspond to the numbers given in Fig. 3.4.*

3.3.3. Verification of Measured Signals

In order to verify the validity of the acceleration waveforms acquired using PadNET, comparative measurements were carried out for the measurement points 2, 3, and 7. For this purpose, a PadNET sensor module and an independent reference 3D acceleration sensor were

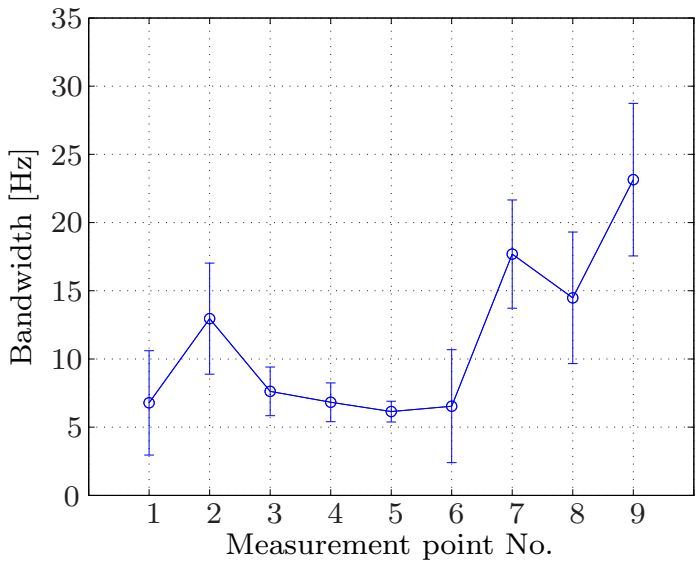

Figure 3.8: *Bandwidth containing 95 % of the energy of measured acceleration waveforms.*

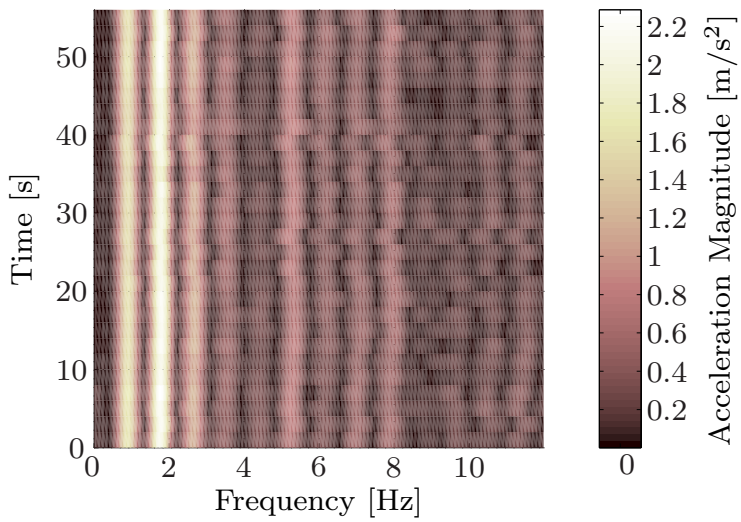

Figure 3.9: *Spectrogram of acceleration waveform of vertical axis at point 8 (see Fig. 3.4).*

mounted to the same measurement point. A test subject was then asked to walk normally for 60 seconds on a treadmill, while the two sensor systems simultaneously recorded acceleration. As reference sensor, a commercial piezoelectric 3D-acceleration sensor (K-Shear, type 8790A500, from Kistler [86]) was used. A force sensor integrated in the tread-mill

measured the ground reaction force for each foot, which allowed the detection of foot impact and hence the accurate segmentation of the waveforms into individual step phases.

While the ground reaction force sensor and the reference acceleration sensor recorded synchronized data, the PadNET system was recording independently. The acceleration waveforms recorded by PadNET and the reference sensor were synchronized by computing the cross-correlation and shifting one waveform as required.

In Fig. 3.10 and Fig. 3.11 data of both sensors is plotted overlaid. The DC component of the PadNET signals is removed for comparison as the reference sensor has a pure AC response. It can be seen, that the two sensor signals match well which verifies the accuracy of the PadNET sensor system.

3.4. Discussion

As can be seen in Sec. 3.3, the acceleration on the body of a walking person has a rich spectral content with a typical bandwidth of 10 Hz to 20 Hz, and the highest significant spectral lines at about 30 Hz. This suggests, that a theoretical analysis of body-worn inertial generators based solely on sinusoidal driving motion is not sufficient. Therefore, the estimation of the performance of body-worn inertial generators presented in Chapter 4 is based on the measured acceleration data discussed above.

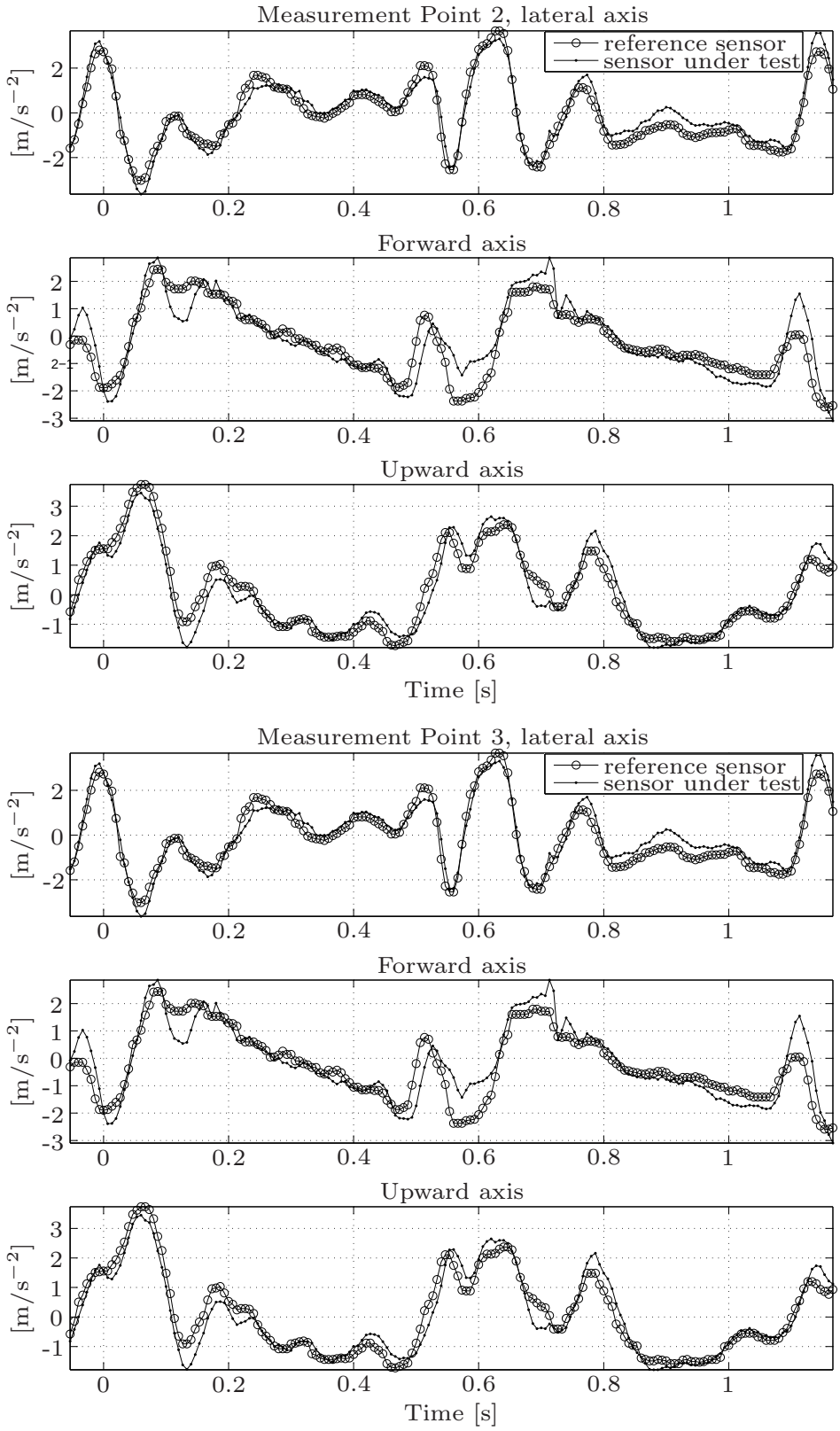

Figure 3.10: *Reference sensor and PadNET sensor data overlaid (measurement points 2 and 3), DC component removed.*

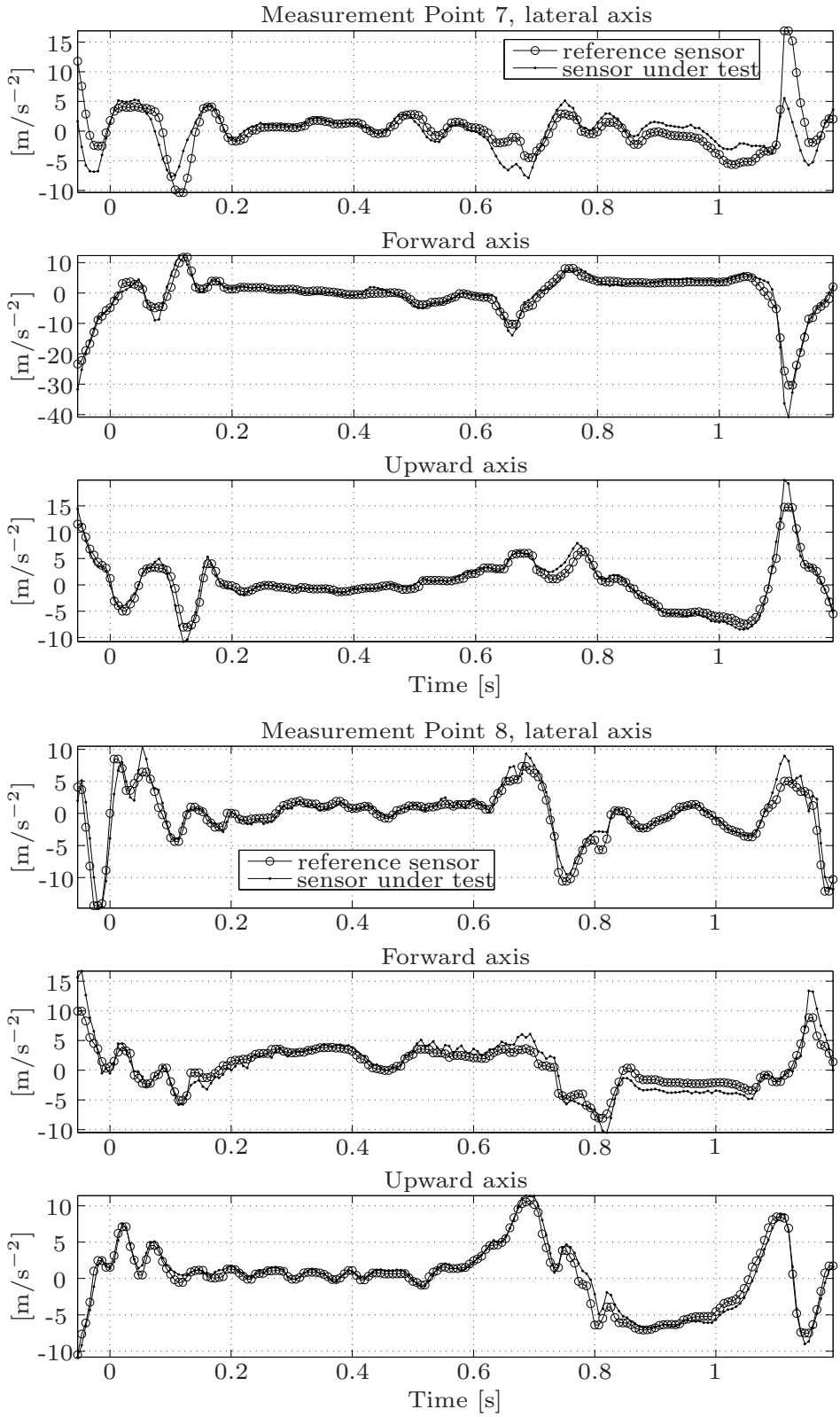

Figure 3.11: *Reference sensor and PadNET sensor data overlaid (measurement points 7 and 8), DC component removed.*

4

Estimation of Achievable Output Power*

In this chapter the output power of body-worn linear inertial generators is estimated based on the optimization of generic mechanical generator models. Acceleration data measured on the human body is used as driving motion for the system models. Three different generator architectures, velocity-damped resonant generators (VDRG), Coulomb-damped resonant generators (CDRG), and Coulomb-force parametric generators (CFPG) are analyzed and compared.

*This chapter is mainly based on [173]

4.1. Introduction

The contribution of this chapter is to estimate typical output power of body-worn inertial linear generators independent of fabrication technology. The estimation is based on the optimization of three architecture classes of body-worn inertial generators that differ in their resonant behavior and their relationship of damping force (transduction force) to proof-mass velocity. These three architectures are modeled using second order mechanical systems as described in Sec. 4.2 below.

Previous work has compared the three architectures for sinusoidal driving motion [115]. However, body motion is far from sinusoidal as has been shown in Chapter 3. Therefore, in this analysis, instead of sinusoidal acceleration, measured on-body acceleration from walking is used as input to the system models[1]. The simulation models of the three architectures together with measured acceleration data can be used to investigate several aspects of the optimization of body-worn inertial generators and answer the following questions:

- *Output power:* What is the generator output power for each body location?
- *Optimal architecture:* Which generator architecture is best suited for which body location and how does this results depend on the size limitation of the generator.
- *Sensitivity to parameter variations:* How sensitive is the generator output power to deviations of the generator parameter from the optimal values?
- *Inter-subject variation:* What are the variations of output power when using motion data from different persons?

4.2. Generator Models

Inertial micro-generators are mixed electro-mechanical systems, in which mechanical motion is used to generate electrical energy through the use of an electric or magnetic field, or a piezoelectric material. However, it is possible to model ideal implementations of these generators as a mechanical system only, *i.e.* a second order mass-spring

[1]The measurement procedure has been described in Chapter 3.

system, where the electrical energy generated is represented as the energy dissipated in a mechanical damper. The operating principle of inertial micro-generators is shown in Fig. 4.1. The inertia of a proof-mass

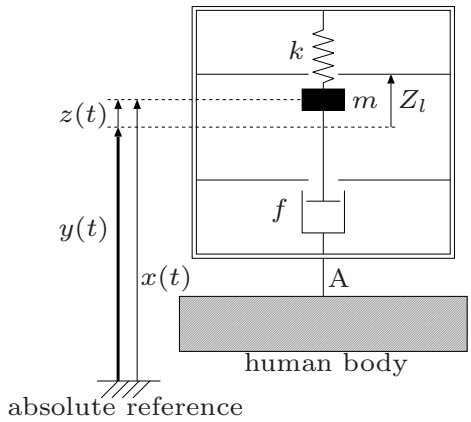

Figure 4.1: *Generic model of an inertial generator mounted on the human body. The proof-mass m is suspended to the generator frame by a spring with spring constant k. The maximum allowable displacement is Z_l. The extracted energy is the work done by the damping force f.*

m, which is suspended on a spring suspension with spring constant k, causes the mass to move relative to the generator frame with relative displacement $z(t)$ when the frame, with displacement $y(t)$, experiences acceleration. The maximum and minimum values of $z(t)$ are $\pm Z_l$, imposed by the finite size of the generator. Energy is converted when work is done against a damping force $f(\dot{z})$ which opposes the relative motion of the proof-mass.

The chosen energy-conversion principle determines the force-velocity characteristic of that damping force, and the characteristic of this force determines the achievable power density.

Inertial micro-generators have been classified into 3 main architectures by Mitcheson et al. [115], depending upon the overall operating strategy of the generator and the velocity-force characteristic of the energy-conversion mechanism. In Fig. 4.2, models are given for the 3 architectures based on the generic model of Fig. 4.1. Fig. 4.3 illustrates the operation of the generators for a sinusoidal displacement input, $y(t)$, with amplitude 1 mm and frequency 10 Hz, showing the relative mass-frame velocity, $\dot{z}$, the damping force, $f(\dot{z})$, and the relative displacement, $z(t)$.

The architectures are briefly summarized below.

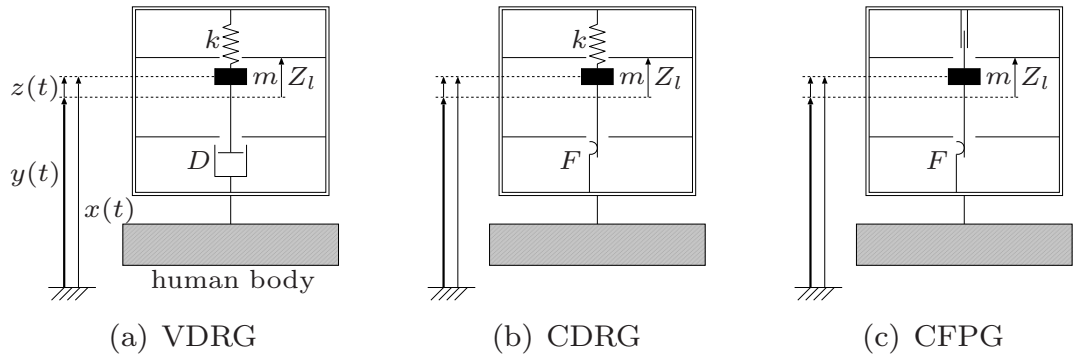

Figure 4.2: *Models of the three generator classes: Velocity-damped resonant generator, Coulomb-damped resonant generator, and Coulomb-force parametric generator.*

1. *Velocity-damped resonant generator (VDRG):* In this device, usually implemented with electromagnetics or piezoelectrics, the damping force is proportional to the relative velocity between the proof-mass and the generator frame (i.e. $f = -D \cdot \dot{z}$, where D is a constant coefficient, called the damping coefficient) [3, 58, 67, 81, 87, 90, 102, 156, 178]. The dashed lines in Fig. 4.3 show the velocity, damping and displacement for a VDRG for $m = 1\,\mathrm{g}$, $k = 80\,\mathrm{N/m}$ and $D = 0.475\,\mathrm{Ns/m}$.

2. *Coulomb-damped resonant generator (CDRG):* In this device, usually implemented with electrostatics, the damping force is of constant magnitude, always opposing relative motion between the proof-mass and the generator frame (i.e. $f = -F \cdot \mathrm{sgn}(\dot{z})$, where F is constant) [113, 150]. This damping force is similar to the one describing Coulomb-friction in mechanical systems.

   An important characteristic of the mass-frame displacement waveform is that a Coulomb-force can cause the relative motion between the proof-mass and the frame to reduce to zero for a period of time [61] in which case the mass 'sticks'. During this phase, no energy is generated. This is shown for two stops per half-cycle, with the solid line in Fig. 4.3, where $m = 1\,\mathrm{g}$, $k = 80\,\mathrm{N/m}$, and $F = 0.95\,\mathrm{mN}$.

   The values taken by the Coulomb-force require some explanation. Sticking occurs when the mass has stopped relative to the frame and the absolute value of the Coulomb-force is larger than the absolute value of the sum of spring force and inertial force at that

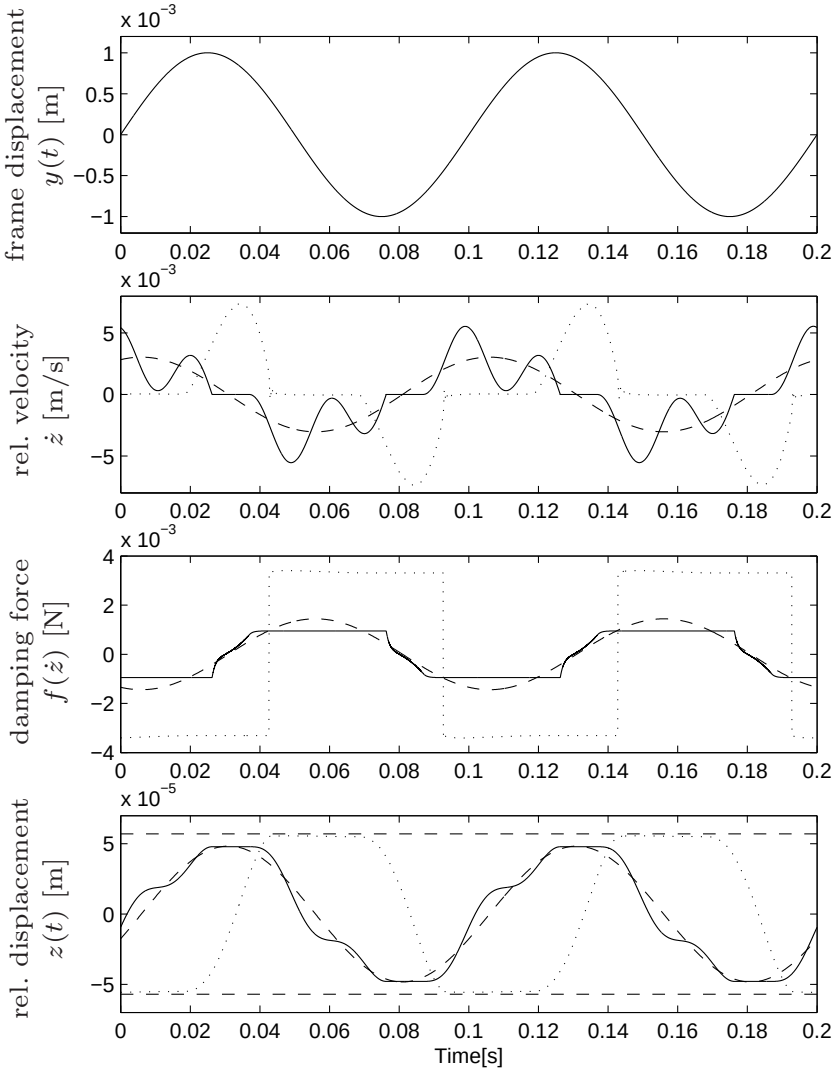

Figure 4.3: *Comparison of the operation of the three generator architectures. Dashed line is the VDRG, solid line the CDRG, and dotted the CFPG.* $\pm Z_l$ *is shown as dashed straight lines.*

time. As soon as the mass starts to move in either relative direction, the Coulomb-force acts to oppose the motion and, during a sticking period, reverses the direction of the resulting relative acceleration. This causes the mass to rapidly oscillate around a point which is stationary relative to the generator frame.

Fig. 4.3 shows the average force for the points in the cycle where the relative mass-frame velocity is zero, as the simulation results have been filtered to remove high frequency oscillation. In a practical CDRG, the capacitor being repeatedly charged and

discharged would be lossy and consequently the device requires hysteresis around $\dot{z}(t) = 0$ in order to reduce the frequency of charging of the capacitors. This would mean that in a practical implementation of a CDRG, the mass would oscillate at reduced frequency but non-zero amplitude.

3. *Coulomb-force parametric generator (CFPG):* In this non-resonant device, again usually electrostatic in nature, the damping force (here also called holding force) is constant and holds the mass at one end of the travel (against an end-stop) until the input acceleration exceeds a threshold, thus ensuring that the distance between the limits is traveled under the highest possible force [115, 116]. The mass starts to move relative to the frame when the inertial force is great enough to overcome the holding force. Once the mass has reached the opposite side of the frame, the sign of the holding force is reversed and a new generation cycle starts. The operation of this generator is shown by the dotted line in Fig. 4.3 for $m = 1\,\mathrm{g}$, $F = 0.81\,\mathrm{mN}$.

4.3. Driving Motion

4.3.1. Data Collection

The estimation of generator output power is based on the measurement of triaxial accelerations on the human body during walking. The collection of the acceleration data is described in detail in Chapter 3.

Simulations to determine the optimal parameters and maximum available power densities have been performed on 10 s of data from one subject. The waveform data gathered from the other subjects has been used to analyze the variations in generator performance across subjects.

4.3.2. Generator Orientation

Orientation (*i.e.* in terms of azimuth and elevation) and consequently the oscillation axis of the proof-mass motion relative to the body can be selected to maximize energy yield. It has been decided to align the generator in a direction for which the acceleration signals have the highest variance, as this gives a reasonable indicator of the orientation which provides maximum power. Thus, the three-dimensional acceleration sig-

nal from each location has been projected onto the chosen orientation[2] to obtain a one-dimensional signal.

4.3.3. Effects of Static Acceleration on Generator Performance

The sensors used to acquire the acceleration data, i.e. the sensors of the PadNET sensor modules (cf. Chapter 3), measure both dynamic (AC) acceleration and static (DC) acceleration. Because the sensors are based on the measurement of the force acting on their proof-mass, gravity affects their output signal. Therefore, a DC component in the acceleration sensor signal can be due to the effect of gravity or a steady acceleration.

As explained in Subsec. 2.5.5, static acceleration affects the quiescent position of the mass within the frame, thus lowering the possible amplitude of relative mass-to-frame motion and consequently lowering the generated power.

In this chapter, it is assumed that the static acceleration can be compensated out by using different damping forces in each direction and so the one-dimensional acceleration signals have been high-pass filtered with a 3rd order Butterworth filter with break frequency 0.4 Hz.

4.4. Optimization of Generator Output Power

4.4.1. Objective

The objective of the optimization is to maximize the mean generator output power by varying the resonant frequency (set by k), and the damping force (D for the VDRG and F for the CDRG).

In this work, only the transduced power, e.g. the power dissipated in the damper of the system models is considered. In an actual generator implementation, suitable power processing will be necessary in order to provide power to external circuitry. The power processing will cause loss of electrical energy. The generator output power is:

$$\overline{P} = -\frac{1}{T}\int_0^T f \cdot \dot{z}\,\mathrm{d}t \tag{4.1}$$

where v is the velocity of the proof-mass. The convention is used, that generated electrical power leads to a positive value of P.

[2]The projection is carried out by computing the scalar product of three-dimensional acceleration and the chosen orientation.

During generator operation the proof-mass may collide with the generator due to the amplitude limitation Z_l. Detailed modeling of such collisions is not attempted in this thesis because it is very dependent on the generator type, structure, and materials used. Instead the amplitude limit, Z_l, is accounted for as follows:

- VDRG and CDRG: Whilst a resonant generator may indeed work if the proof-mass collides with the constraining end-stops, it is no longer acting in a resonant mode. Thus, output power is set to zero for solution sets for which the resonant generators exceed the displacement constraint. Note that this procedure underestimates the generated energy for the cases where optimal generator operation includes end-stop collisions.

- CFPG: This device is designed to operate with the proof-mass snapping backward and forward between end-stops. If the holding force (Coulomb force) has been set optimally for a particular flight, the mass arrives at the opposite side of the generator frame with zero velocity. If the holding force is set below the optimal value then the mass simply arrives at the opposite side of the frame with a non-zero velocity, and some kinetic energy will be lost in the impact. The simple assumption used in this work is that upon impact, all kinetic energy is lost, i.e. the relative mass-frame velocity becomes zero. Thus, this procedure overestimates the mechanical losses due to end-stop collision and consequently may underestimate the generated energy.

Hence, the output power for VDRG, CDRG, and CFPG, respectively, is:

$$\overline{P}_{vdrg} = \begin{cases} -\frac{1}{T}\int_0^T D\dot{z}^2 \mathrm{d}t & \text{if } |z(t)| <= z_l \ \forall t \in [0,T] \\ 0 & \text{otherwise} \end{cases} \tag{4.2}$$

$$\overline{P}_{cdrg} = \begin{cases} -\frac{1}{T}\int_0^T F\,\mathrm{sgn}(\dot{z})\,\dot{z}\mathrm{d}t & \text{if } |z(t)| <= z_l \ \forall t \in [0,T] \\ 0 & \text{otherwise} \end{cases} \tag{4.3}$$

$$\overline{P}_{cfpg} = -\frac{1}{T}\int_0^T F\,\mathrm{sgn}(\dot{z})\,\dot{z}\,\mathrm{d}t \tag{4.4}$$

4.4.2. Optimization Procedure

As the CFPG has only one parameter to optimize (the value of the Coulomb-force, F) the maximum power for the CFPG has been found

by sweeping this parameter across a range.

The resonant generator models have two parameters to be optimized: the resonant frequency (set by k), and the damping force (D for the VDRG and F for the CDRG). The used optimization procedure is schematically shown in Fig. 4.4. Starting with initial values for k and D

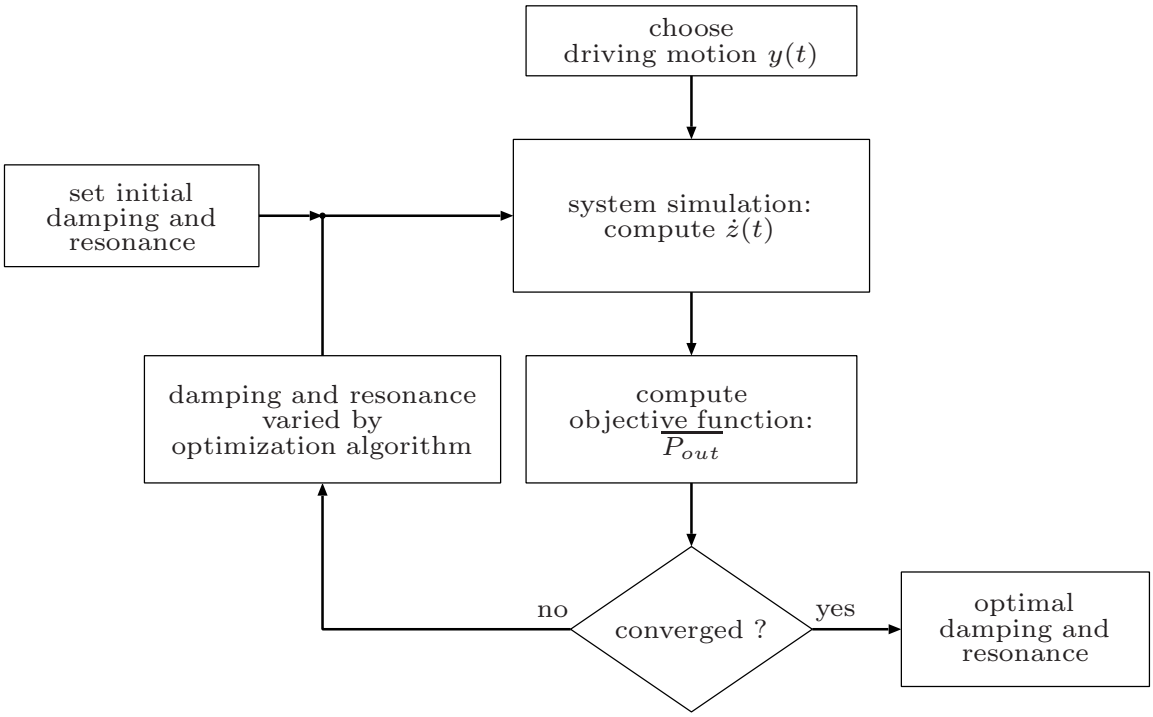

Figure 4.4: *Flow chart of VDRG and CDRG optimization*

or F, the waveform of $\dot{z}(t)$ is computed. Subsequently, the mean output power is computed according to (4.2) and (4.3). Based on the result, the optimization algorithm, adaptive simulated annealing [71], varies the parameters. The loop is repeated until the algorithm has converged to a solution.

Adaptive simulated annealing has been chosen as optimization algorithm because being a stochastic method it is less likely than gradient methods to become stuck in a local minimum.

4.4.3. Parameter Limits

The lower limits for the parameters of k and ω_n have been set to zero for the optimization. The upper limits chosen can be justified as follows. The CFPG and the CDRG generate energy until the Coulomb-force is increased to a point where the force is too large to allow any rela-

tive movement between the mass and frame. The value at which the Coulomb-force F becomes large enough to stop relative mass-frame motion is the value used for the upper limits of the search space.

The upper limit of spring constant k has been set to a value which, even with very little damping, still limits the internal mass-frame displacement to less than Z_l. Care has been taken to ensure that the resulting maximum undamped resonant frequency ($\omega_n = \sqrt{k/m}$) is well above the bandwidth of the input motion. This guarantees that the optimal value of k is included in the search space.

The same argument is used to set an upper limit on the value of velocity damping coefficient, D. The damping coefficient should not be greater than that which restricts the motion of the proof-mass from moving the distance $2Z_l$ in one period, because in an optimal configuration, the proof-mass will likely make full use of the allowed travel.

4.4.4. Generator Configurations

The generator configurations in Tab. 4.1 have been used in the simulations for all generator architectures, in order to investigate the effect of size on generator performance.

Table 4.1: *Generator configurations used.*

Config N^o.	m [g]	Z$_l$ [mm]
1	0.1	0.05
2	0.3	0.25
3	0.5	1
4	1	5
5	2	20

Configurations 1 and 2 correspond to MEMS implementations of micro-generators, with 1 being smaller than reported configurations, and 2 being the typical size of previously reported generators. Configurations 3-5 correspond to generators which could be fabricated using standard precision engineering techniques. Configuration 5 is larger than could be tolerated in many suggested applications, but is included for comparison purposes and to give a broader indication of generator scaling effects.

4.4.5. Measurement Noise in Acceleration Signals

In order to ensure that noise in the acceleration signals is not a large contributing factor to the power generated, data from stationary sensors has been recorded and the same optimization process has been carried out as previously for the actual measured waveforms. In most cases, the power generated from these signals is negligible compared to the power generated from the signals from the walking motion. The exception is the smallest generator configuration used (configuration 1), where in the worst case, the power generated from the noise rises to 35% of the power obtained from walking motion. However, the median ratio of power generated from noise to power obtained from walking motion is only 5% for configuration 1.

4.5. Results

4.5.1. Performance Comparison

The plots of Fig. 4.5 show the maximum generator power from 2 different generator sizes, after optimization. Results are given for all three architectures on each of the nine measured locations on the body. Fig. 4.5(a) shows the maximum generator power for configuration 2, and Fig. 4.5(b) shows the performance of the larger configuration 5. Locations 2-6 are on the upper body, and 7-9 the lower body, with location 1 being on the head (cf. Fig. 3.4).

For inertial generators under walking conditions, the lower body locations yield around 4 times more power than the upper body locations. This is to be expected because the accelerations on the lower body have higher RMS values.

Figs.4.5(a) and 4.5(b) show that optimized generator performance on locations 2-6 (on the upper body and the sacrum) are similar, and performance from locations 7-9 (on the knee and lower leg) are also similar. Consequently, in order to reduce the complexity of some of the following plots, two data sets have been formed, with the power equal to the mean of the values of the set from the various locations. The sets are: ‘upper body’, consisting of locations 2-6 and ‘lower body’ consisting of locations 7-9.

As can be seen, the CFPG is a marginally better choice for small generator sizes for most locations. As the generators increase in size, the resonant devices start to outperform the CFPG. The CDRG is never as

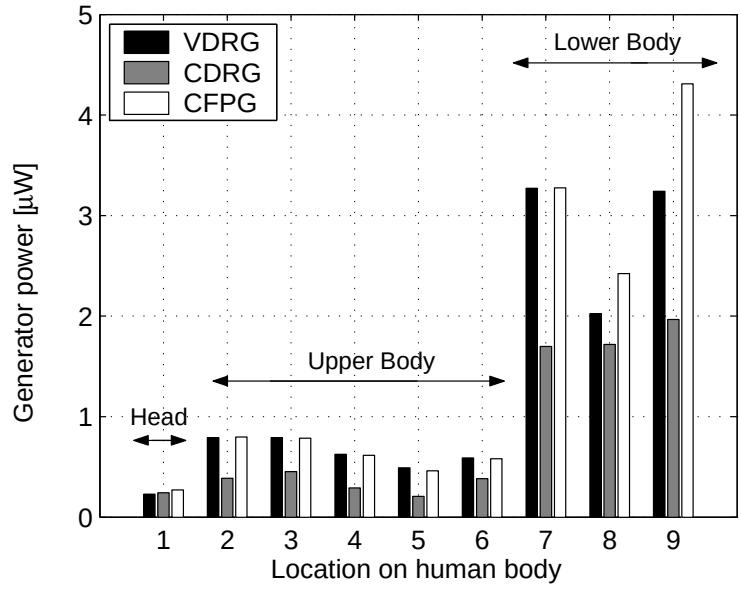

(a) Configuration 2 ($Z_l = 250\,\mu$m, $m = 300\,$mg)

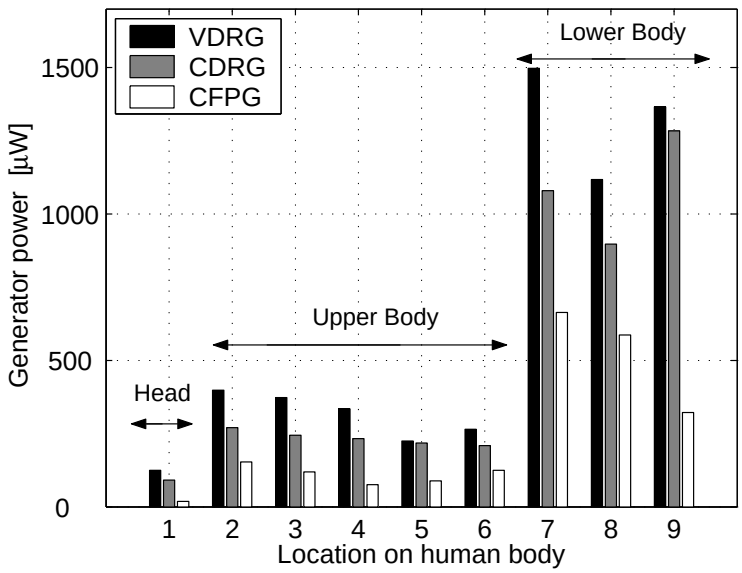

(b) Configuration 5 ($Z_l = 20\,$mm, $m = 2\,g$)

Figure 4.5: *Generator architecture absolute performance. Z_l is the displacement limit of the proof-mass, m is the mass. The locations are indicated in Fig. 3.4.*

good as the VDRG. The VDRG is the best choice for the larger scale devices.

In Fig. 4.6 the averaged normalized power values have been plotted against Z_l for the two data sets. By interpolating between the computed points it is possible to estimate the generator dimension (represented

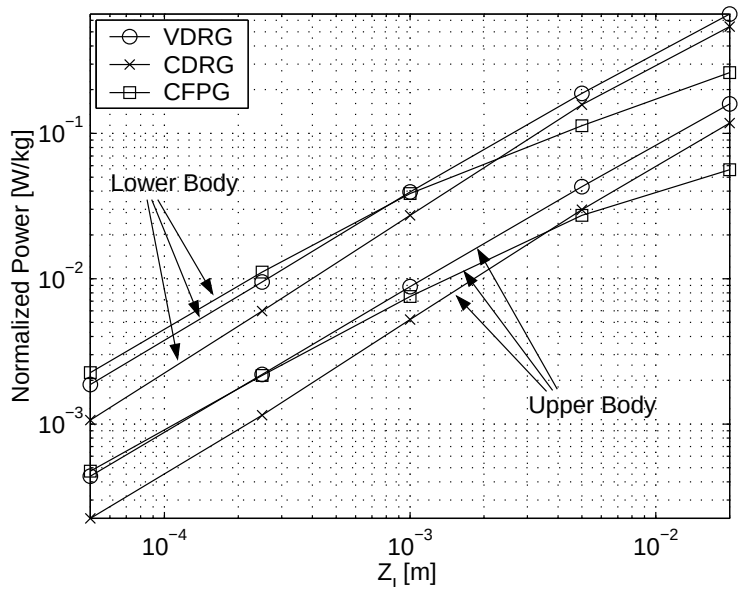

Figure 4.6: *Comparison of architecture performance for generators mounted on the upper and lower body (power normalized by the proof-mass, m). Z_l is the displacement limit of the proof-mass.*

by Z_l) where the resonant devices start to outperform the CFPG. For the upper body this cross-over point is located at about 200 μm and for the lower body at about 800 μm.

4.5.2. Optimal Parameters

The variation in the optimal generator damping parameters with generator size is shown in Figs. 4.7, 4.8, and 4.9 for VDRG, CDRG, and CFPG, respectively. As with the plots for generator output power, the VDRG damping coefficient D, and the Coulomb-force, F, have been normalized by the value of the proof-mass (because the optimal trajectory is maintained for constant D/m and F/m values). It should be noted that the relationships between optimal damping, optimal spring constant and Z_l discussed in this section are solely based upon the 5 generator sizes which have been simulated.

Fig. 4.7 shows the variation of the damping coefficient D with Z_l for the VDRG. Over much of the range, the data forms a straight line on a log-log plot, and over that range, $D \propto 1/Z_l$. Once Z_l exceeds 5 mm, this relation no longer holds for all positions.

Fig. 4.8 shows the normalized Coulomb-Force for the CDRG. As can be seen, for a given location, the force is approximately constant

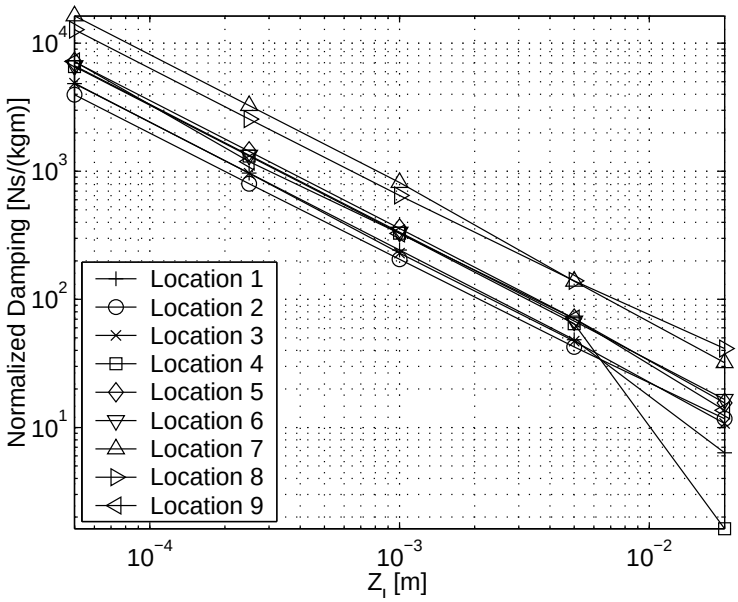

Figure 4.7: *Optimal VDRG damping coefficient.*

for $Z_l < 5\,\text{mm}$ before starting to decrease for some locations.

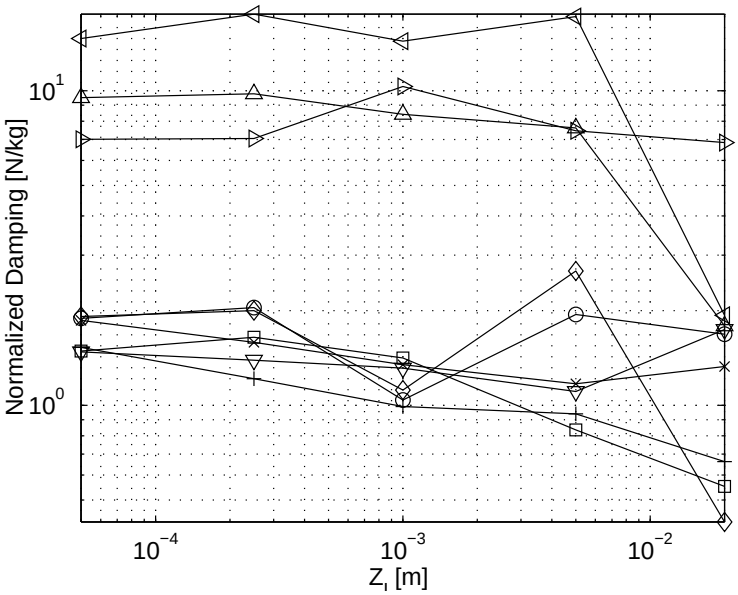

Figure 4.8: *Optimal CDRG damping force.*

Fig. 4.9 shows the dependence of the optimal holding force of the CFPG on Z_l. It should be noted that as the value of Z_l increases, it is expected that the optimal holding force would reduce to allow the mass to travel further in one flight.

Fig. 4.10 shows the dependence of the optimal resonant frequencies

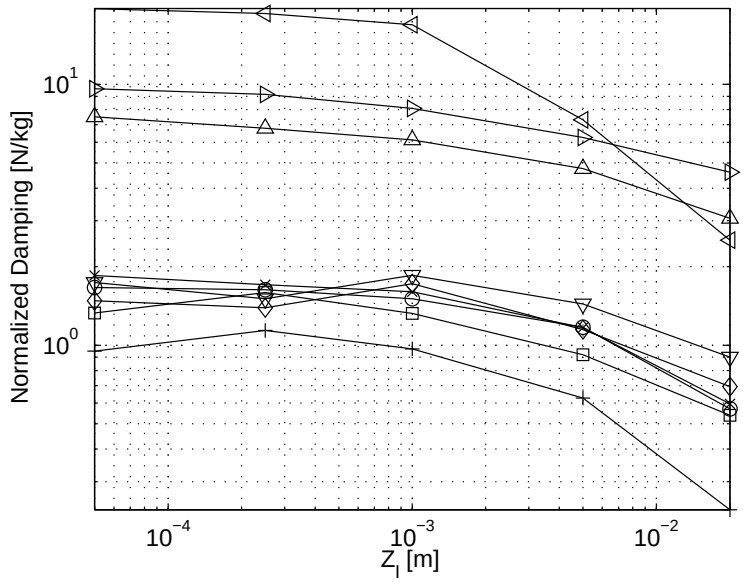

Figure 4.9: *Optimal CFPG damping force.*

on generator size.

Fig. 4.10(a) shows the variation of optimal resonant frequency for the VDRG. For $Z_l < 1\,\text{mm}$, $\omega_n \propto 1/\sqrt{Z_l}$, i.e. $k \propto 1/Z_l$. When Z_l is larger than 1 mm, the relation no longer holds for all locations, with resonant frequencies rising above that predicted by this relationship.

Fig. 4.10(b) shows the dependence of the CDRG optimal resonant frequency upon the value of Z_l. Whilst these lines are not completely parallel, the relationship between the Z_l and the optimal resonant frequency is approximately $k \propto 1/Z_l$, i.e. the same as the VDRG.

The changes in the relationships between the parameters (i.e. a proportional relationship until Z_l exceeds a certain value followed by a different choice of optimal parameter) suggests that the optimal operation for the generators shifts between modes, which correspond to the system changing from being overdamped or underdamped, i.e. once Z_l has exceeded $10^{-3}m$, resonant amplification is possible. This is shown in Fig. 4.11, with the resonant generators producing an output which is much closer to a sinusoid for configuration 5 (which operates underdamped) than configuration 2 (which operates overdamped).

4.5.3. Sensitivity of Power to Generator Parameters

It is important to consider the sensitivity of power output to changes in generator parameters. Firstly, the measured acceleration data used in the optimizations is for a narrow range of walking speed, and the reso-

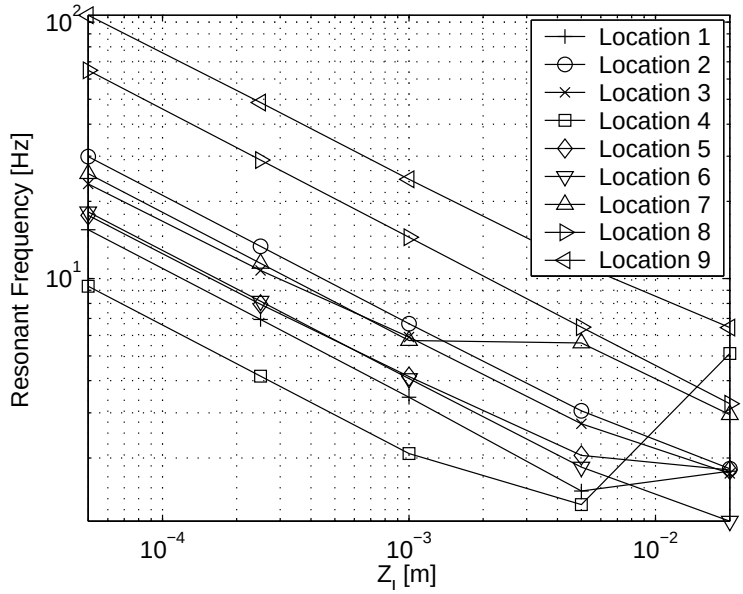

(a) Optimal VDRG resonant frequency.

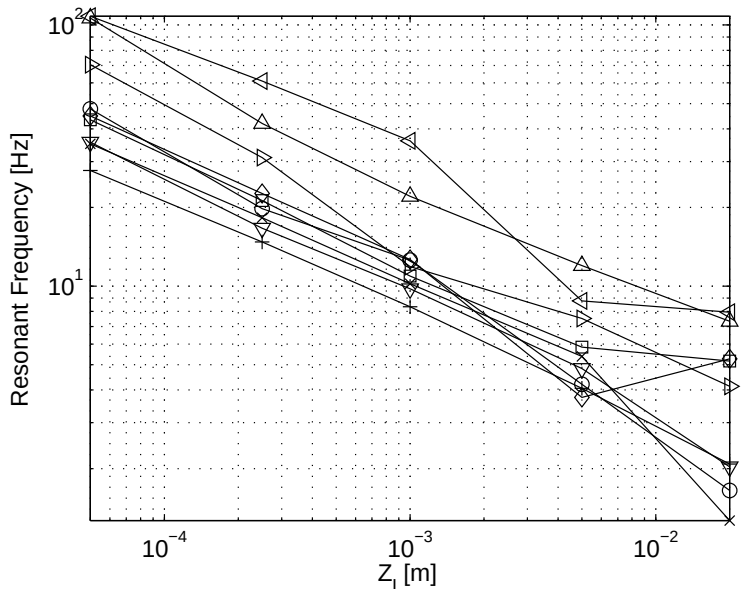

(b) Optimal CDRG resonant frequency.

Figure 4.10: *Optimal generator resonant frequency.*

nant frequency will probably not be dynamically adjustable. By varying the spring constant in the simulation we can alter the relation between resonant frequency and walking speed, which, assuming a similar harmonic content, gives a reasonable approximation to varying walking speed. Although the damping coefficient may be dynamically varied, how precisely it is optimized will depend on the control circuitry and other factors so the dependence of power on the deviation of damping from optimality is also of interest.

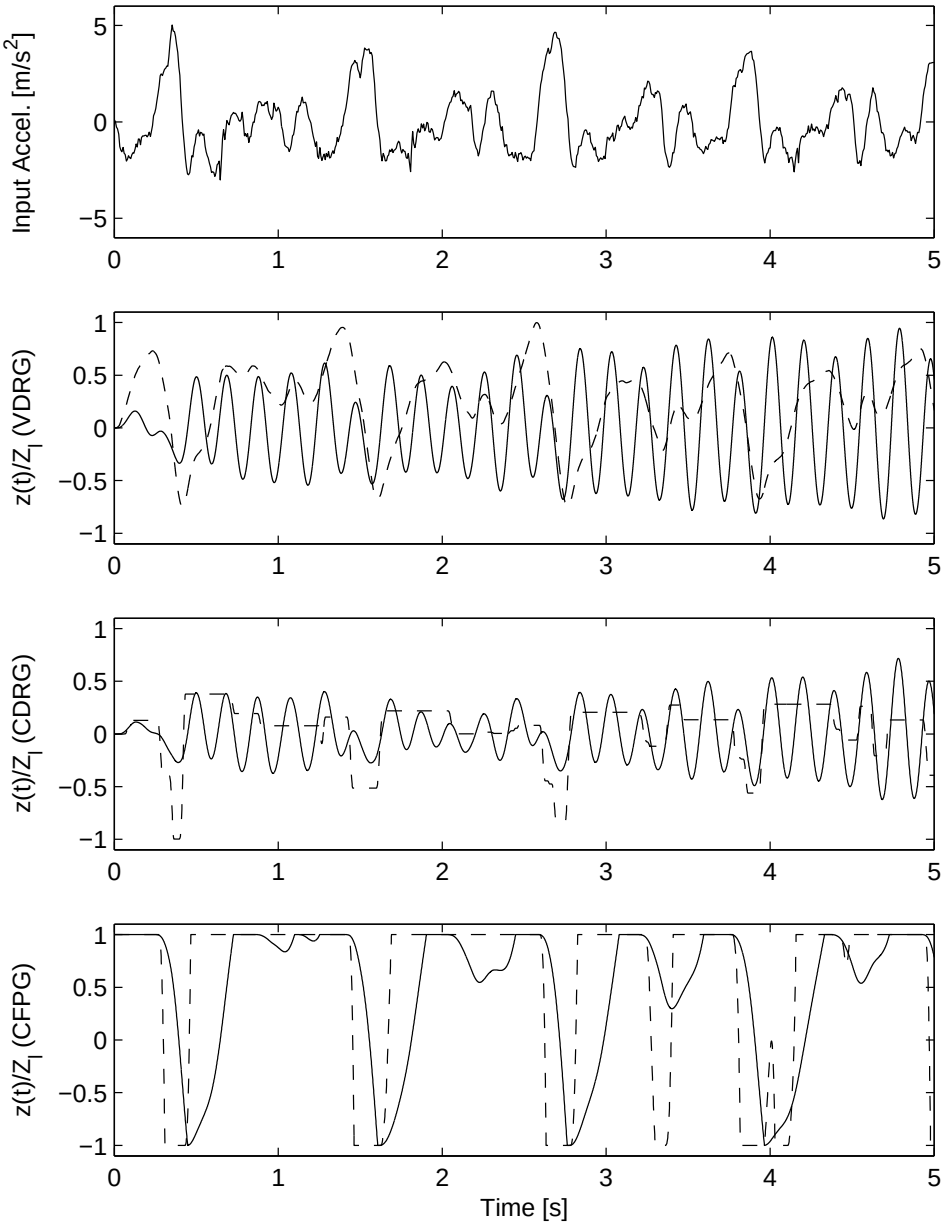

Figure 4.11: *Relative position waveforms for two sizes of each architecture for one input acceleration waveform. The dashed line is configuration 2. and the solid line configuration 5.*

Therefore the parameters of spring constant (for resonant generator types only) and damping term (for all generator types) have been varied. For every optimum, both parameters have been varied in 7 discrete steps to deviate ±20 % from the optimal value. The results have been grouped and averaged for the upper body and the lower body groups as before.

The damping parameter is regarded as adjustable online during generator operation and consequently when varying the spring constant, the damping parameter has been re-optimized each time. In contrast, the spring constant is regarded as fixed during generator operation and has hence been held constant during the variation of the damping parameter.

In Figs. 4.12 and 4.13 the generator output power for two generator sizes (configuration 2, small, and configuration 5, large) is shown. The power and the parameters are normalized by the respective values at the optimal point. For the resonant generator types, points with damping parameter values below the optimum are not shown because they all violate the displacement constraint.

For 13 out of the 20 cases, the generated power does not fall more than 20% for a deviation of 20% of the parameters from the optimal values. Larger drops in generator power occur for the CDRG for the upper body and the CFPG with an above optimal damping parameter. For the CFPG this is due to the fact that the number of flights of the proof-mass is strongly reduced with the damping force above optimal, while below the optimum the generated power is approximately proportional to the damping force. For the CDRG the cause for the power drop may be the increase in the number of times the mass motion sticks relative to the frame.

While the CFPG has the inherent advantage of not having a resonant frequency, and therefore offering the potential of being fully optimized dynamically to suit the operating conditions, Figs. 4.12(a) and 4.13(a) show that the loss of power for the small VDRG, for example, with loss of tuning is not rapid.

4.5.4. Inter-Subject Variations

As mentioned in Sec. 4.3, the generators have been optimized for the input waveforms of one subject. However, the variations in generator performance across subjects have also been considered. This has been done by feeding acceleration waveforms from the seven other subjects into the optimized generator models. The damping parameter has been re-optimized for every waveform since it is considered adjustable online during generator operation. The output power values for the other subjects are comparable to the ones of the main subject (same order of magnitude, typically not deviating more than $\pm 50\,\%$).

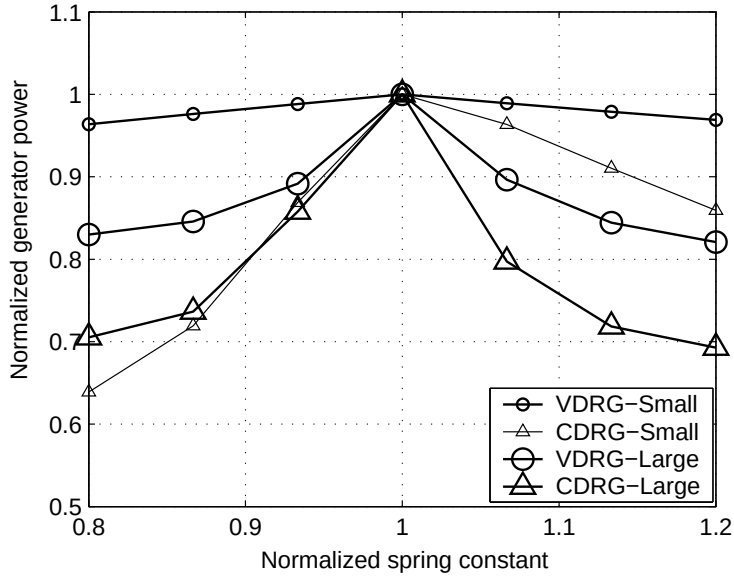

(a) Generator power with deviation in k, upper body.

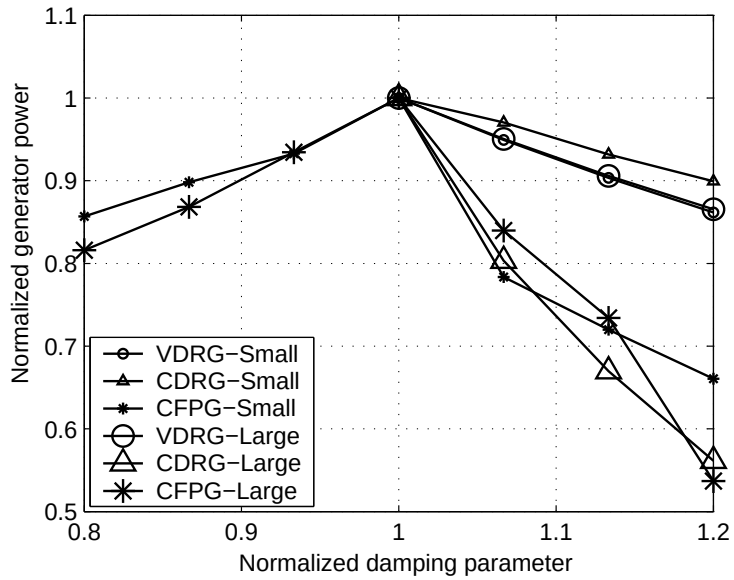

(b) Generator power deviation in damping, upper body.

Figure 4.12: *Sensitivity of generator power to changes in generator parameters, data set 1 (upper body).*

4.6. Practical Considerations

4.6.1. Realization of Optimal Parameters

An important question is what minimum generator size and mass would be needed to realize the required parameters found in Subsec. 4.5.2.

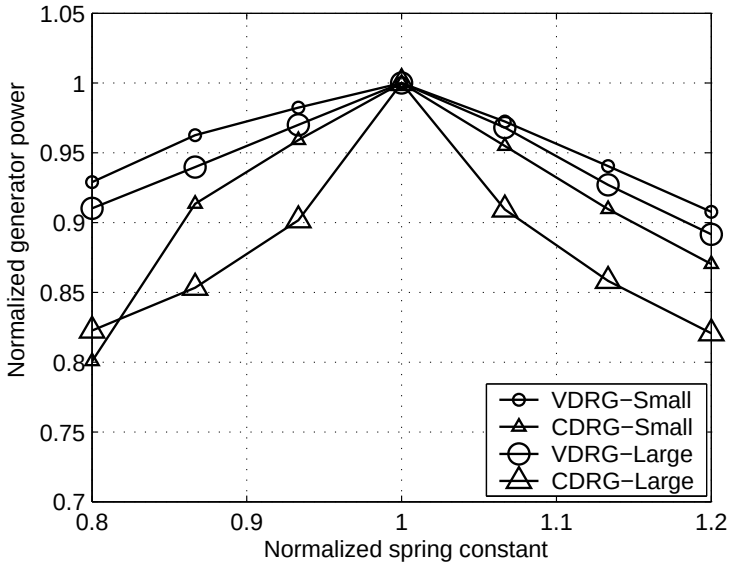

(a) Generator power with deviation in k, lower body.

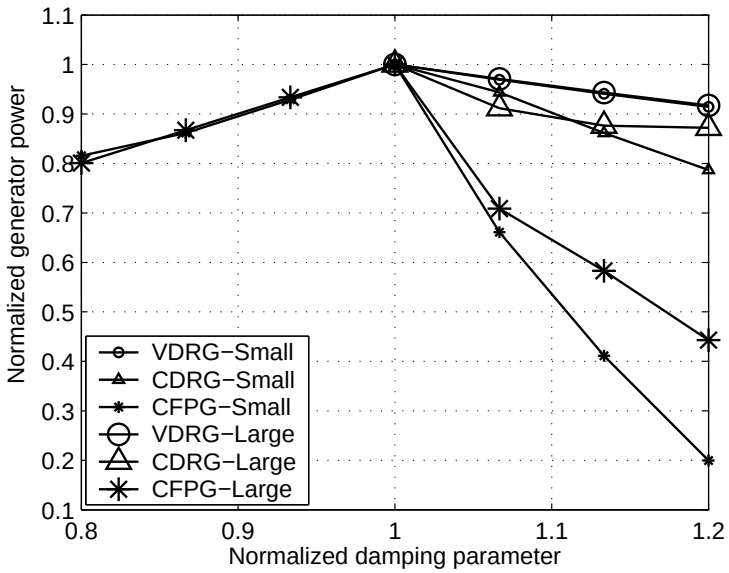

(b) Generator power with deviation in damping, lower body.

Figure 4.13: *Sensitivity of generator power to changes in generator parameters, data set 2 (lower body).*

Here, the issues are only briefly discussed based on simple generator implementations. A more detailed scaling analysis has been carried out for an electromagnetic VDRG implementation in Chapter 5. A simple realization of a VDRG is a cylindrical coil moving in and out of a homogeneous magnetic field region and connected to a resistive load. The Lorentz force that occurs is the damping force. A CDRG/CFPG

can be implemented by a parallel plate capacitor, where one plate is movable. Here, the damping force is the electrostatic force between the capacitor plates. There are two basic types: The gap-opening type is operated in constant charge mode and the sliding-plates type is operated in constant-voltage mode. For these configurations it can be shown that when all dimensions are scaled by the same factor the VDRG force is proportional to L^3 while the CDRG/CFPG force is proportional to L^2, where L is the dimension of length. Hence, for decreasing sizes, the electromagnetic damping forces drop more rapidly than the electrostatic ones and it becomes increasingly difficult for the former to achieve the required damping to operate optimally.

4.6.2. Adjustment of Damping Force

In order to adapt to different driving motions, the damping force needs to be adjustable online. In an electromagnetic VDRG implementation this can be done by changing the load resistance. In electrostatic generators the damping force is controlled via the voltage of the capacitor.

4.6.3. Compensation of Static Acceleration

As stated in Subsec. 4.3.3 it is assumed that static acceleration can be compensated out by adding a constant offset force. Whilst this is difficult to do for the electromagnetic and piezoelectric generators, it is much easier to achieve for electrostatic generators, i.e. the CDRG and the CFPG. In electrostatic generators the offset force can easily be realized by using different electrostatic forces in the up and down directions, which in turn can be achieved by pre-charging the capacitor to different values depending upon the relative direction of travel of the mass.

4.6.4. Startup

Another practical issue is startup. While an electromagnetic generator based on permanent magnets can start up with zero electrical energy stored, an electrostatic generator needs a minimum energy to charge the capacitor. In principle, it is possible to use an electret to precharge the capacitor [19, 166], however, in that case the damping force is not easily adjustable.

4.7. Discussion

Fig. 4.6 shows that for human walking movements, the generator architecture with the highest power density is dependent upon generator size and the position on the body on which the generator is mounted. The CFPG is the optimal architecture on the lower body when $Z_l < 800\,\mu$m and the VDRG for $Z_l > 800\,\mu$m. For the upper body, the architecture choices are the same, but the cross over point is at $200\,\mu$m.

For sinusoidal motion the cross over point between architectures can be defined in terms of the ratio of Z_l/Y_0 and ω/ω_n [115], where Y_0 is the amplitude of the driving motion. With inputs containing multiple frequencies, this distinction cannot easily be made as a single value for Y_0 and ω/ω_n cannot defined: each frequency component has a different amplitude Y_0 and frequency ω. However, it can be noted that the displacements on the upper body are smaller than the lower body. Consequently, it is reasonable to expect that the value of Z_l for which there is a change in optimal architecture is smaller for the upper body locations.

The achievable power density for inertial micro-generators does not remain constant for changes in generator size (specifically for changes in Z_l) [115] and so absolute power densities cannot be quoted. For optimal implementations of resonant micro-generators with sinusoidal inputs, the volume of the proof-mass will be half of the generator volume [115] (because the generated power is proportional to both m and Z_l). Whilst the proportionality to Z_l does not hold exactly for non-sinusoidal motion, Fig. 4.6 shows that for all architectures and for $Z_l < 1\,$mm, the power is approximately proportional to Z_l. Consequently, setting the mass to occupy half the volume is a good approximation to obtaining the highest power density for small generators. However, this assumption will underestimate the maximum power density for the larger generators.

The achievable power densities have been calculated for the sizes of generator studied in this chapter based upon the assumption that the mass occupies half the volume. With $Z_l = \pm 250\,\mu$m this gives a total length of the generator (in the direction of mass motion) of 1 mm, allowing for the height of the mass. Assuming the generator is cube shaped, then the total volume of an optimal mass, made of gold, is $0.5\,\text{mm}^3$, giving a total mass of 10 mg. This gives power densities of $140\,\mu\text{W/cm}^3$ for location 9, and $8.7\,\mu\text{W/cm}^3$ for location 1, for CFPGs. For $Z_l = \pm 5\,$mm, the power density is $2100\,\mu\text{W/cm}^3$ for location 9 and

134 μW/cm^3 for location 1, in this case for VDRGs.

For wearable applications, sensor nodes will usually be monitoring environmental conditions or biological functions and thus have modest data rate requirements. For example, heart rate monitoring has been estimated to require only 80 bits/min [187]. It can be shown that transmission at up to 1 kbit/s over a 1 m range can be provided with sub-microwatt power levels [186]. Recently, A-D converters have been reported with power consumption of 1 μW with sampling rates above the requirements for health monitoring applications. Assuming that additional power of as low as 2 μW is sufficient for sensor operation and suitable signal processing, a power level of 3 μW may be sufficient for realistic sensor nodes. Consequently the minimum size of a micro-generator for use on the human body to allow it to drive a sensor and wireless link lies between 1 mm^3 and 1 cm^3 depending on the location of the generator on the body, and the duty cycles of the motion and the sensor operation.

4.8. Conclusions

The simulated performance of the three micro-generator architectures has been investigated with the input motion being human walking motion. Acceleration data has been measured from 9 body locations on 8 human test subjects. One test subject has been chosen and the generator parameters have been optimized on 10 s of the data from that subject for all body locations. Five different sizes of generator have been investigated and their optimal parameters have been plotted against generator size. For the resonant generators with Z_l values less than 1 mm, the optimal values of spring constant and damping are proportional to $1/Z_l$. For $Z_l > 1$ mm, the optimal values no longer obey this proportionality, which suggests a change in the mode of generator operation.

The generated power for generators where $Z_l < 1$ mm is proportional to Z_l. For generators with larger Z_l, this relationship breaks down, with generated power increasing less rapidly with Z_l. This suggests that as generators get large, an optimal micro-generator configuration will contain a proof-mass which occupies more than half the volume of the generator. The maximum power output of a generator for a given input and value of Z_l is proportional to the value of the proof-mass and thus optimal values of the parameters, D, F and k also scale with the value of the proof-mass.

It has been shown that the CFPG is the architecture which achieves the highest power density for smaller generators and the VDRG for larger generators, with the cross over points being $Z_l = 200\,\mu$m for generators mounted on the upper body and $Z_l = 800\,\mu$m for the lower body. The CDRG did not outperform the other two architectures for any location or for any size of generator. The scaling laws of electrostatic forces and electromagnetic forces also demonstrate the suitability of the CFPG to small generators and the VDRG to larger generators. There is a distinct difference between the energy generated from upper and lower body locations for walking motion, with there being approximately 4 times as much energy available from the lower body locations. However, it should be noted that many sensors, especially implanted medical sensors, would need to be mounted on specific locations and hence it might not be possible to place them at the locations which achieve the highest power densities.

The output power of the VDRG is less sensitive to changes in spring constant than is the output power of the CDRG. The output power of the CFPG is less sensitive to a reduction of the damping force than to an increase. When, for a given optimal spring constant, the damping parameter for the resonant generators is set to below the optimum, the proof-mass hits the end stops, which shows that under optimal operation, the resonant generators operate to the displacement limit.

5

Generator Design

In the previous chapter, the velocity-damped resonant generator, VDRG, has been found to be the recommended architecture for linear inertial generators with an internal displacement limit of more than about $200\,\mu\mathrm{m}$ *to* $800\,\mu\mathrm{m}$. *In this chapter, an electromagnetic generator is presented that approximates a VDRG. First, a novel architecture comprising generator and bearing is presented. Subsequently, a two-stage optimization strategy is proposed. The first stage optimizes the generator geometry, while the second stage optimizes resonance frequency and electrical load. The influence of generator size and parameter variations are analyzed as well.*

5.1. Introduction

In Chapter 4, three inertial generator architectures have been compared:

- velocity-damped resonant generator, VDRG
- Coulomb-damped resonant generator, CDRG
- Coulomb-force parametric generator, CFPG

It has been found that the VDRG is the recommended architecture, when the proof-mass has an internal displacement limit of more than 200 μm to 800 μm. Therefore, the VDRG has been chosen as basis for a generator design in this thesis. VDRGs can be approximated using electromagnetic generators or piezoelectric generators. This thesis focuses on electromagnetic generators.

In the following sections, an architecture for an electromagnetic generator is chosen and an optimization strategy is proposed.

5.2. Generator Architecture

5.2.1. Electromagnetic Part

A linear electromagnetic generator comprises a moving part, the translator and a stationary part, the stator. One of these parts carries the armature coils, where the energy conversion takes places. During operation, the relative motion between stator and translator leads to a varying magnetic flux through the armature coil windings. As consequence, a voltage equal to the negative rate of flux change is induced. Note, that in inertial generators, the translator constitutes the proof-mass.

As architecture for further study, a permanent magnet air-cored tubular architecture based on [11] is selected. It uses axially magnetized permanent magnets on the tubular translator and coils on the iron-less stator. An example of the used architecture is shown schematically in Fig. 5.1, the associated geometric parameters are listed in Tab. 5.1.

The translator consists of several axially magnetized disc-shaped magnets separated by soft-magnetic spacers. The magnetization directions of neighbouring magnets are opposing. The soft-magnetic spacers act as flux concentrators and form the magnetic poles. In addition, they reduce the repellent force between two neighboring magnets. The stator

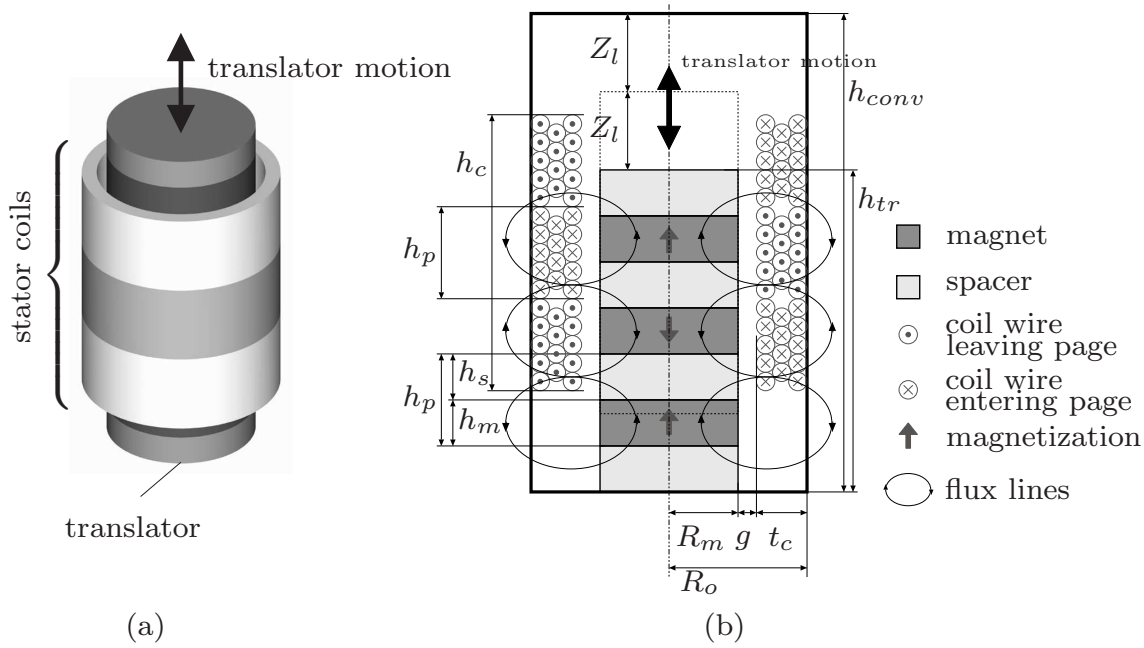

Figure 5.1: *Stator and translator of selected generator architecture: a) 3D model, b) axial cross-section with the translator displaced to the bottom limit. The center translator position is indicated by the dashed line. The coils are fixed to the generator frame. R_m, g, and t_c are magnet radius, air-gap length, and coil thickness, respectively. The maximum peak to peak displacement of the translator is $2Z_l$.*

Table 5.1: *Design parameters of chosen architecture*

Name	Description
h_p	pole pitch
h_s	height of soft-magnetic spacer
h_m	height of magnet
R_m	radius of magnet
g	air-gap length
t_c	coil thickness
n_m	number of magnets
n_c	number of coils
Z_l	maximum translator displacement
d_w	diameter of coil wire with insulation
d_{wi}	diameter of coil wire without insulation

contains several armature coils, adjacent coils are wound in different directions and connected in series. In order to maximize the magnetic flux cut by the coils, the axial height of a coil, h_p, is equal to the combined height of a magnet and a soft-magnetic spacer.

This architecture has the following advantageous properties:

- *Field generated by permanent magnets:* Permanent magnets instead of current carrying coils are used to generate the magnetic field which allows the generator to start up from zero stored energy and avoids additional ohmic losses.

- *Moving magnet:* Compared to moving coil generators, the selected moving magnet architecture (magnets on the translator, armature coils on the stator) avoids electrical connections to moving parts. Compared to moving-iron generators, the total generator mass is reduced because the mass of the magnets can be used at the same time as proof-mass.

- *Axially magnetized magnet:* Axially magnetized magnets are simpler to manufacture and hence less costly than radially or Halbach-magnetized magnets.

- *Iron-less core:* The stator contains no soft-magnetic material to avoid an attractive force between stator and translator which would impose a mechanical burden on the bearing. Also, additional eddy currents and magnetic hysteresis losses would occur. Disadvantages, compared to an iron core, are a weaker magnetic field and more leakage flux.

- *Rotation-symmetric design:* The generator topology is rotation-symmetric which generally simplifies construction and simulation (2D simulation possible).

For the shown configuration of Fig. 5.1, the flux, as a function of the translator displacement out of the center, has even symmetry and is maximal for displacement zero. If one magnet were added to the translator, then the flux function would have odd symmetry and be zero at the center position. In this thesis, these two configuration types are referred to as having *even* and *odd flux symmetry*. Any design of the used architecture with an odd difference between number of magnets and number of coils has odd flux symmetry, a design with an even difference has even flux symmetry.

The generator in Fig. 5.1 is *translator-limited*: the total height, h_{conv}, is defined by the translator length and the peak to peak displacement, $2Z_l$. The total height may also be defined by the coil height, h_c, such a generator being called *coil-limited*. Hence:

$$h_{conv} = \max(h_{tr} + 2Z_l, h_c) \tag{5.1}$$

5.2.2. Bearing

Requirements

The bearing of inertial generators has two functions:

1. *Guidance:* The bearing has to guide the motion of the translator and to keep a defined air-gap length between translator and stator.
2. *Spring:* The bearing has to provide an elastic restoring force to allow reciprocating translator motion.

The requirements towards the bearing are:

- low mechanical friction
- stiff in direction orthogonal to translator motion
- provide displacement-proportional restoring force
- low and controllable stiffness in direction of translator motion
- low wear, long life-time
- well-defined precise motion
- displacements larger than 0.5 mm achievable
- passive: no power required to operate bearings

Out of these requirements, low friction and high lateral stiffness are the most important. High friction would lead to high mechanical losses which reduces generator efficiency. Low stiffness in lateral direction would lead to frequent collisions between stator and translator leading to high wear and additional mechanical losses. The requirement that the achievable displacement should be larger than 0.5 mm is a consequence of the findings in [173]. There it was found, that the generator type VDRG outperform other generator types, if their translator is allowed to move than a certain threshold. This threshold is at about 0.5 mm.

Design space exploration

The following list gives an overview of the main types of existing bearing.

- *Sliding bearings:* These bearings carry the load by sliding. Friction and wear is relatively high, although a lubricant may be used to lower the friction.
- *Rolling-element bearings:* A rolling-element bearing, e.g. a ball bearing, is a bearing which carries a load by placing round elements between the two pieces. The relative motion of the pieces causes the round elements to roll with little sliding.
- *Jewel bearings:* A jewel bearing is a bearing which allows motion by running a shaft slightly off-center so that the shaft rolls inside of the bearing rather than sliding. As the shaft rolls, the center precesses.
- *Fluid bearings:* Fluid bearings, are bearings which support load on a thin layer of liquid or gas. They either require an external pump (hydrostatic bearings) or only work when the bearing is in motion (hydrodynamic bearings).
- *Magnetic bearings:* A magnetic bearing supports a load using magnetic levitation. However, magnetic levitation is not possible with static magnetic fields as proven by Earnshaw's theorem. Possibilities to enable magnetic levitation include diamagnetic structures [139] or feedback control system in conjunction with electromagnets.
- *Flexible bearings:* A flexible bearing, also called flexure bearing, allows motion by bending a load element. It is simple, compact and light weight. In addition, it has low friction. However, the available displacement is often limited.

Among these bearings, flexible bearings best fulfill the combined requirements of low friction, low wear, and being passive.

Selected bearing

The bearing used is shown in Fig. 5.2. It is a parallel spring stage similar to the one reported in [64, 159] and consists of two parallel

beams with two necked down flexible hinges each. When the translator is displaced, the four notches are elastically bent and thus a restoring force is provided. The restoring force is linear for small displacements. This bearing has the following advantages:

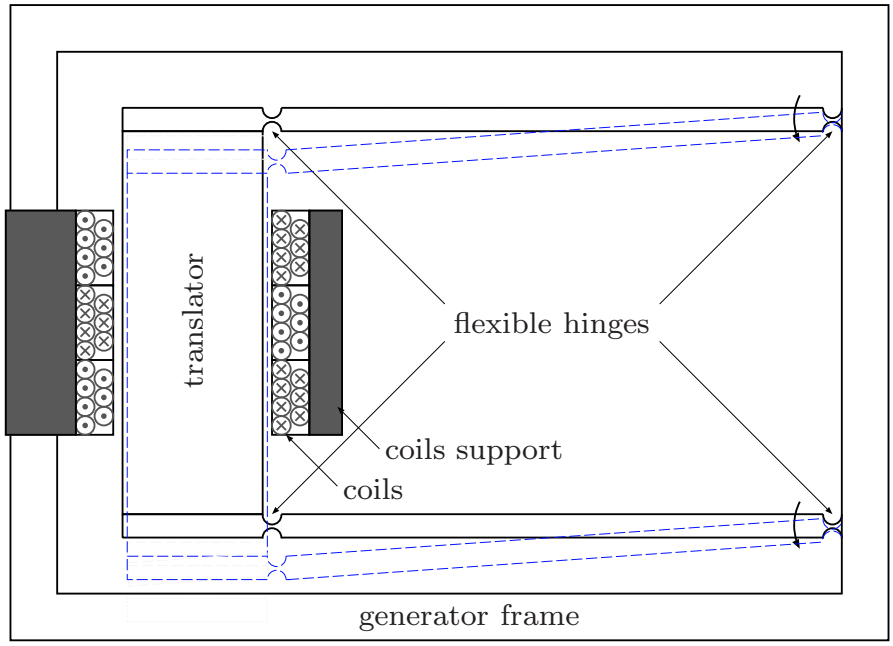

Figure 5.2: *Schematic cross-section of flexible bearing used to suspend translator to generator frame. The dashed line indicates the displaced structure.*

- In contrast to ball-bearings the flexible bearing has no rubbing parts and therefore less wear and a longer life-time.
- Compared to a generator with a helical spring bearing, the translator is guided more precisely, which allows short air-gap lengths between translator and stator and therefore a better electromagnetic performance.

Disadvantages are the limited displacement, unwanted lateral motion, rather high stiffness in the direction of translator motion, and a significant amount of occupied volume.

Computation of the resonant frequency

In the used flexible bearing, the spring constant k is composed of the contributions of the four flexible notch hinges. A close-up view of a

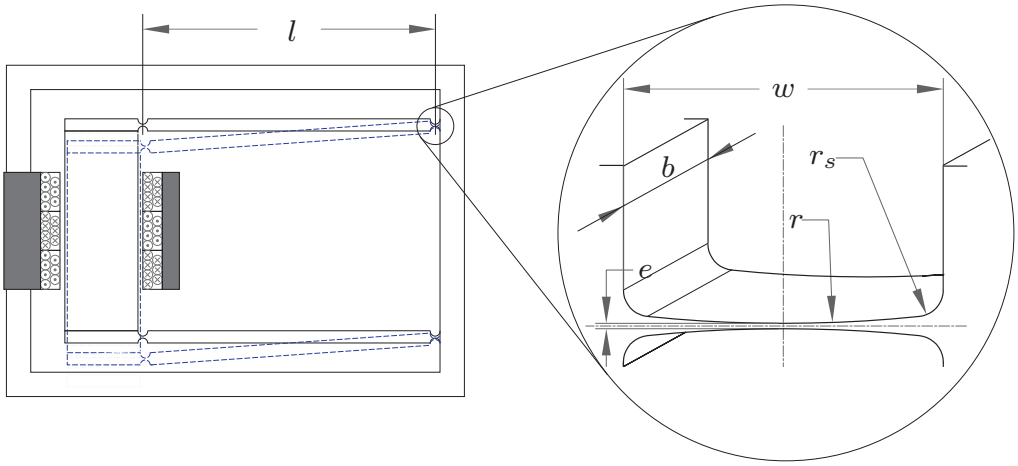

Figure 5.3: *Flexible bearing with notch detail.*

single notch is shown in Fig. 5.3. The notch has a circular shape with radius r which is trimmed to a width of w. The notch has a uniform depth of b and a thickness of e in the middle. The notch has chamfers with radius r_s in order to avoid stress concentrations at the border between the arc with radius r and the vertical notch wall.

According to [62, 63], the spring constant k of the flexible bearing is given by

$$k \approx \frac{8}{9\pi} E \frac{be^{2.5}}{l^2\sqrt{r}} \tag{5.2}$$

where E is the elastic modulus, r is the radius of the notches, e is the thickness at the middle of the joints, b is the depth of the joints and l is the length of the arms from neck to neck. However, this equation is only valid for small displacements and if the stress in the material is below the elastic limit σ_{adm}. In addition, it is assumed that all four notch hinges have exactly the same geometry.

Given the spring constant k, the undamped resonant frequency f_n of the inertial generator can be computed as:

$$f_n = \frac{1}{2\pi}\sqrt{\frac{k}{m}} \tag{5.3}$$

where k is the spring constant and m is the translator mass.

Thus, the spring constant k and consequently the resonant frequency f_n of the generator can be controlled by choosing suitable values for b, e, l, and r and selecting a material with a suitable elastic modulus E.

Maximum displacement

Since the stresses that occur in the joints when the translator is displaced are limited, there will be a maximum linear displacement Z_{lb} of the translator. Z_{lb} is approximated in [62] as follows:

$$Z_{lb} \approx \frac{3\pi}{4} \frac{\sigma_{adm}}{E} l \sqrt{\frac{r}{e}} \tag{5.4}$$

where σ_{adm} is the maximum admissible stress in the joints.

Lateral displacement

When the translator is displaced its motion is not strictly linear, but in fact curvilinear with a small lateral displacement. The maximum lateral displacement is:

$$\Delta x = l - \sqrt{l^2 - {Z_{lb}}^2} \tag{5.5}$$

where Z_{lb} is the maximum possible axial displacement and l is the arm length of the bearing.

Design considerations

Thus, in order to design a suitable flexible bearing for the inertial generator, the geometric parameters r, e, b, and l should be chosen to satisfy the following requirements:

- The resonant frequency f_n as given by (5.3) should match the specified value.
- The maximum possible displacement Z_{lb} should be at least as large as the displacement limit Z_l imposed by the end-stops.
- The maximum lateral translator displacement Δx must be less than the air-gap length between translator and stator, otherwise the translator will collide with the stator coil.

5.3. Optimization Method

5.3.1. Design Goal

The goal of the generator optimization method presented in this thesis is to maximize the generator output power for a given generator volume, V_{conv}, translator displacement, Z_l, and driving acceleration $\ddot{y}(t)$.

5.3.2. Method Outline

The optimization is based on the system model of Subsec. 2.5.3:

$$\ddot{z} + \frac{1}{m} \cdot D \cdot \dot{z} + \omega_n^2 z = -\ddot{y} \tag{5.6}$$

$$\ddot{z} + \frac{1}{m} \cdot \frac{\hat{D}(z)}{1+\alpha} \cdot \dot{z} + \omega_n^2 z = -\ddot{y} \tag{5.7}$$

where $\hat{D}(z)$ is the force capability of the generator, ω_n is the natural angular frequency of the system, and α is the ratio of load to coil resistance, R_l/R_c.

In the above equation electromagnetic, mechanical, and electrical parameters are incorporated:

- *electromagnetic parameters:* The flux gradient, ϕ_z, the coil resistance R_c and consequently $\hat{D}(z)$ are determined solely by translator and stator geometry and material parameters.
- *mechanical parameters:* The spring constant k and consequently the resonance frequency are determined by the design of the bearing that connects translator and generator frame.
- *electrical parameters:* The load resistance R_l and consequently α can be considered as adjustable while the generator is operating. This can be done by suitable electronic circuitry connected to the generator.

In this thesis it is proposed to split up the optimization of the above parameters into two stages:

1. *Optimization of stator and translator geometry:* Stator and translator geometry are optimized to provide maximum force capability for a given generator volume V_{conv} and translator displacement limit Z_l. As the force capability $\hat{D}(z)$ is dependent on z, the maximum and the mean value in the range $[-Z_l, Z_l]$ are considered.
2. *Optimization of spring constant and load resistance:* Using the results from the first optimization stage, the spring constant k and the load resistance R_l are optimized for a given driving acceleration $\ddot{y}(t)$. Note, that varying k tunes the resonance frequency, while varying R_l tunes the force velocity ratio $D(z)$.

5.3.3. Justification of Optimization Method

Splitting up the optimization into two stages can be justified by the following arguments:

- *Reduced computational complexity:* Optimizing all parameters at once while observing the constraints on V_{conv} and Z_l, as well as considering the driving acceleration $\ddot{y}(z)$ would be too computationally intensive. First finding an optimal geometry before the driving accelerations are considered, reduces the complexity to a reasonable level.

- *Scaling up $\hat{D}(z)$ increases output power:* A generator B is able to generate more output power than a generator A if the following conditions are all met:

  – the force capabilities of the two generators are related by

  $$\hat{D}_B(z) = p\hat{D}_A(z) \tag{5.8}$$

  where p is a scaling factor independent from z.

  – $p > 1$ ($\hat{D}_B$ is a scaled up version of $\hat{D}_A$)

  – both generators have the same translator mass m and natural frequency ω_n

  – both generators are driven by the same acceleration $\ddot{y}(t)$

  This can be explained as follows:

  1. The ratio α_B of load resistance to coil resistance of generator B can be tuned in such a way that the force velocity ratios $D(z)$ of the two generators are equal. Using (2.21) we get:

  $$\frac{\hat{D}_B}{1+\alpha_B} = \frac{\hat{D}_A}{1+\alpha_A} \tag{5.9}$$

  $$\frac{p\hat{D}_A}{1+\alpha_B} = \frac{\hat{D}_A}{1+\alpha_A} \tag{5.10}$$

  $$\alpha_B = p(1+\alpha_A) - 1 \tag{5.11}$$

  2. As the two generators now have the same values for $D(z)$, ω_n, m, and $\ddot{y}$, the system equations (2.27) and consequently the resulting relative position $z(t)$ are also the same.
  3. Due to the identical values of $D(z)$ and $z(t)$ the total converted power $\overline{P_{conv}}$[1] is the same for both generators, accord-

[1] $\overline{P_{conv}}$ includes the power dissipated in the coil resistance.

ing to (2.30).

4. According to (2.33), the output power values $\overline{P_{out}}$ of generator A and B are related as follows:

$$\frac{\overline{P_{out}}_B}{\overline{P_{out}}_A} = \frac{\frac{\alpha_B}{1+\alpha_B}}{\frac{\alpha_A}{1+\alpha_A}} = \frac{\alpha_B}{1+\alpha_B}\frac{1+\alpha_A}{\alpha_A} \tag{5.12}$$

After inserting α_B as obtained in (5.11) we get:

$$\frac{\overline{P_{out}}_B}{\overline{P_{out}}_A} = \frac{p(1+\alpha_A)-1}{p(1+\alpha_A)} \cdot \frac{1+\alpha_A}{\alpha_A} \tag{5.13}$$

$$= 1 + \frac{p-1}{p}\alpha_A \tag{5.14}$$

Thus, for $p > 1$:

$$\overline{P_{out}}_B > \overline{P_{out}}_A \tag{5.15}$$

If the ratio between the force capabilities $\hat{D}_B/\hat{D}_A$ is not a constant however, it is not clear which generator will perform better.

Nevertheless, the fact that scaling up $\hat{D}(z)$ increases output power suggests that the mean and the maximum of $\hat{D}(z)$ in the range $[-Z_l, Z_l]$ provide a reasonable figure of merit for stator and translator. Having a figure of merit that is independent from the resonance frequency, load resistance, and driving waveforms, justifies a separate optimization of stator and translator geometry.

5.4. Optimization of Stator and Translator

5.4.1. Overall Goal

The goal of this first optimization stage is to maximize the force capability of the generator, independently from the driving motion. This is done by varying the geometric parameters of stator and translator. In order to allow comparison between different designs the combined volume of stator and translator is fixed in the optimization.

The force capability in this thesis is defined as the ratio of electrical damping force to translator velocity, when the generator is operating with the stator coils short-circuited. Two objectives are considered: the maximum and the mean of the force to velocity ratio within the displacement limits of the translator.

From (2.15), the damping force for zero load resistance is:

$$f = -\frac{\phi_z^2}{R_c} \cdot \dot{z} \tag{5.16}$$

The force to velocity ratio is:

$$\hat{D}(z) = \frac{|f|}{|\dot{z}|} = \left(\frac{\mathrm{d}\phi}{\mathrm{d}z}\right)^2 \frac{1}{R_c} \tag{5.17}$$

where $\phi(z)$ is the flux through the stator coil for a given translator position z. Note that $\hat{D}$ is dependent on the translator position z.

5.4.2. Objective Function

Definition

The force capability $\hat{D}(z)$ is dependent on the translator position which is allowed to vary in the range of $[-Z_l, Z_l]$. In order to carry out an optimization, however, an objective function is needed, that describes the optimization goal as a single value (figure of merit), independent of z. However, it is not clear how a single value can be derived from $\hat{D}(z)$ in a way that is optimal for body-worn inertial generators. In this thesis, two different objective functions are used for comparison:

$$\hat{D}_{max} = \max(\hat{D}(z)) \tag{5.18}$$

$$\hat{D}_{mean} = \overline{\hat{D}(z)} \tag{5.19}$$

Here, only values of translator positions within the displacement range are considered: $z \in [-Z_l, Z_l]$. The objective of the optimization is to *maximize* $\hat{D}_{max}$ or $\hat{D}_{mean}$.

Computation

In order to compute one value of the objective function, $\hat{D}_{max}$ or $\hat{D}_{mean}$, a 2D axisymmetric FE model is constructed based on the given geometric parameters. Subsequently, the flux $\phi(z)$ is computed at several discrete positions by magneto-static Finite Element Analysis (FEA) using Ansys Emag [6]. An exemplary FE model and the corresponding field solution are shown in Fig. 5.4.

The objective functions are computed as follows:

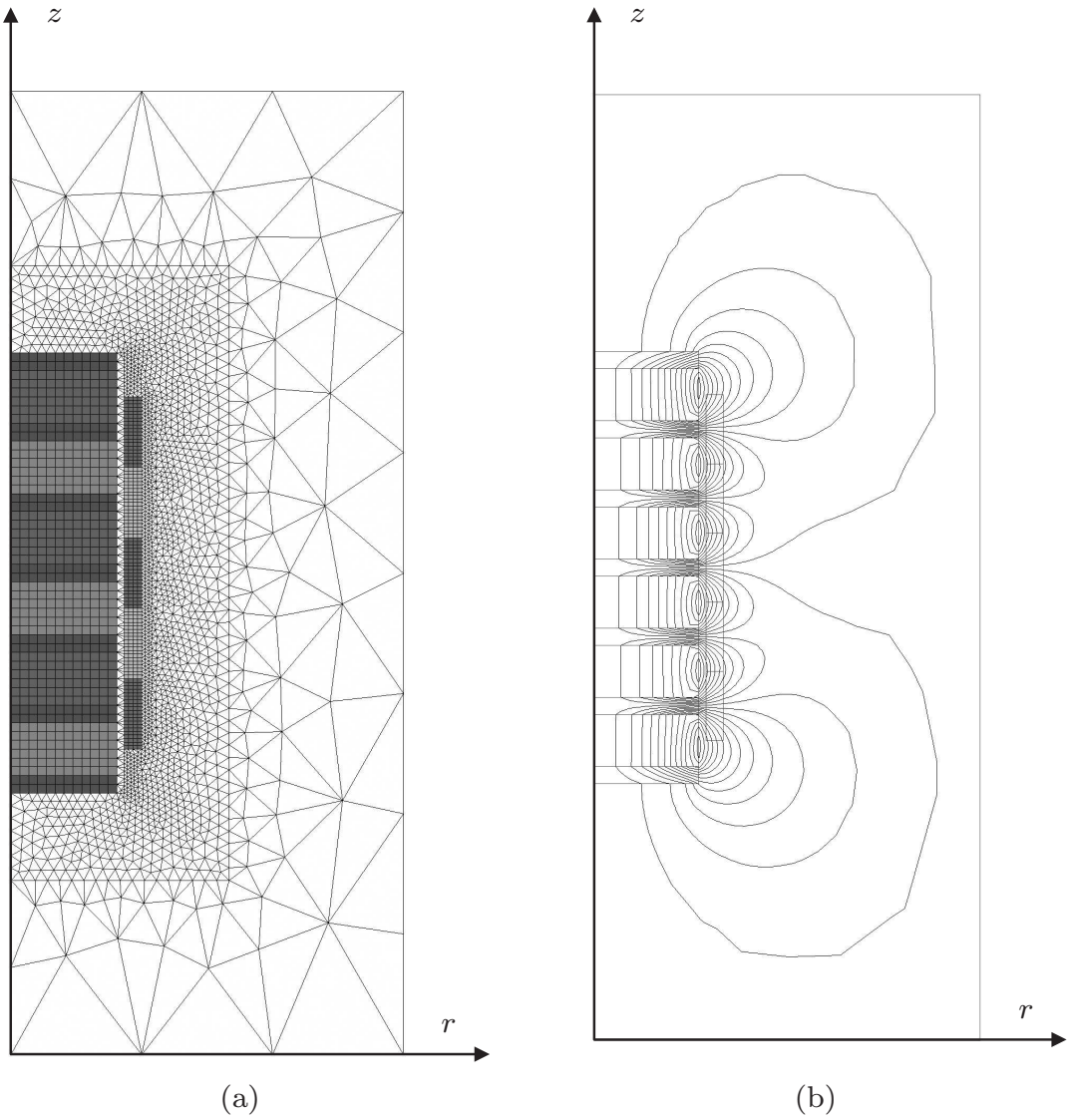

Figure 5.4: *(a) FE model of generator, (b) flux lines of FEA solution.*

- $\hat{\mathbf{D}}_{\mathbf{max}}$: The flux gradient ϕ_z is only computed at the position, z_0 where it is maximal. For odd flux symmetry designs this position is $z_0 = 0$, for even flux symmetry designs this position is approximately at $z_0 = h_p/2$. At z_0 the flux gradient is then approximated by finite differences:

$$\phi_z(z_0) = \frac{\phi(z_0 + \Delta z) - \phi(z_0 - \Delta z)}{2\Delta z} \tag{5.20}$$

where Δz is a finite position difference. In this thesis, this difference has been set to $\Delta z = h_p/2$.

Subsequently, the objective function is computed as

$$\hat{D}_{max} = \Big(\phi_z(z_0)\Big)^2 \frac{1}{R_c} \tag{5.21}$$

Note, that only two FEA runs are necessary to compute $\hat{D}_{max}$.

- $\hat{\mathbf{D}}_{\mathbf{mean}}$: Here, the flux gradient $\phi_z(z)$ is computed for the half range of the translator position: $z \in [0, Z_l]$. This is done by

  1. computing the flux $\phi(z)$ in increments of $\Delta z = h_p/4$
  2. applying a spline-interpolation to get an approximation of $\phi(z)$
  3. deriving $\phi(z)$ with respect to z to obtain $\phi_z(z)$

  Subsequently, the objective function is computed as

$$\hat{D}_{mean} = \text{mean}\left\{\Big(\phi_z(z)\Big)^2 \frac{1}{R_c}\right\} \tag{5.22}$$

  The number of FEA runs required is

$$N = \text{ceil}\left(\frac{4Z_l}{h_p}\right) + 1 \tag{5.23}$$

Note, that the computation of $\hat{D}_{mean}$ is more computationally intensive than the computation of $\hat{D}_{max}$.

5.4.3. Optimization Procedure

For the optimization, the volume V_{conv}, the air-gap length g, and the amplitude limit, Z_l, are fixed. V_{conv} is defined as the cylinder that encompasses stator and translator with the translator motion taken into account (outer rectangular frame in Fig. 5.1(b)). The volume of the translator bearing is ignored to separate the electromagnetic aspects from the mechanical aspects. Hence:

$$V_{conv} = \pi {R_o}^2 \cdot h_{conv} \tag{5.24}$$

Fig. 5.5 shows a flow chart of the optimization procedure. First, flux symmetry (odd or even, cf. Subsec. 5.2.1), and objective function ($\hat{D}_{max}$

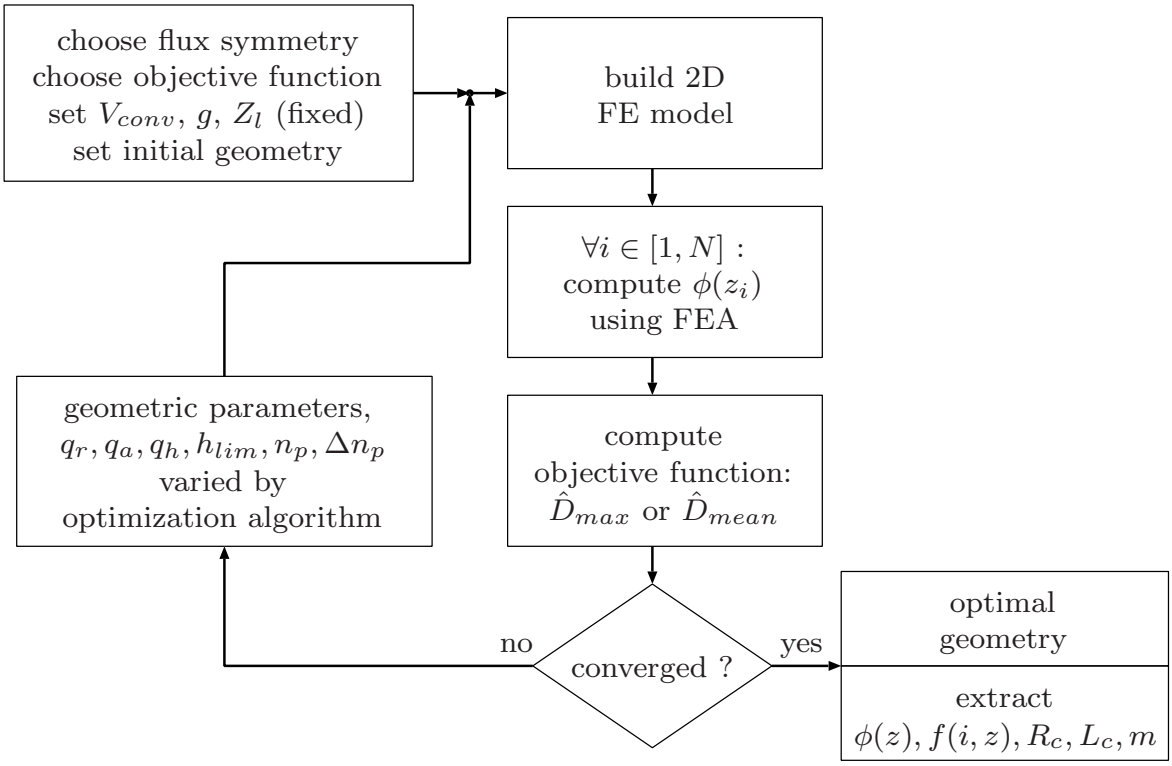

Figure 5.5: *Flow chart of first optimization stage: optimization regarding maximum force capability.*

or $\hat{D}_{mean}$) have to be chosen. Then, starting with an initial geometry, the objective function is computed. Based on the result, the optimization algorithm varies the geometry. As optimization algorithm, adaptive simulated annealing [71] has been selected[2]. The objective function is then computed again. This loop is repeated until the algorithm has converged to a solution and hence the maximum of the objective function has been found. Based on the resulting geometry, the parameters required by the system model of the second optimization stage are then computed: the flux function, $\phi(z)$, the force function, $f(i, z)$, the coil inductances, L_c, the coil resistance, R_c, and the translator mass, m.

The used fixed and variable parameters of the optimization are listed in Tab. 5.2. The values of the fixed parameters are set as follows. The volume, V_{conv}, and amplitude-limit, Z_l, are chosen small enough to

[2]Adaptive simulated annealing (ASA) is a stochastic optimization method and is less likely than gradient-based methods to become stuck in a local maximum of the objective function. At the same time, ASA is preferable to an exhaustive search of the parameter space because the exhaustive search method is too computationally intensive.

allow a reasonably small generator, the air-gap length, g, is chosen large enough to allow for tolerances in the translator bearing. The binary parameter h_{lim} determines whether a *translator-limited* or *coil-limited* configuration is used, see also Subsec. 5.2.1. The part that defines h_{conv} (stator or translator) is then divided into n_p poles, the other part into $n_p + \Delta n_p$ poles. Note that h_{lim} is therefore considered as a variable binary optimization parameter.

Assuming constant fill factor of the coil[3], varying the wire diameter d_w does not affect the force capability, hence d_w is not included in the parameter list.

The parameter range for q_r and q_h is $[0.05, 0.95]$. The boundaries for the aspect ratio q_a are set according to a maximum generator height, h_{conv}, of 20 mm and a maximum outer radius, R_o, of 3 mm. Larger dimensions are deemed to be unsuitable for a body-worn micro generator. The minimum for the coil thickness t_c is 10 μm. n_p is restricted to be in the range between 1 and 25 to keep manufacturing complexity low. The range of Δn_p is limited to $[-5, 5]$ in order to have little unused stator or translator volume.

Table 5.2: *Parameters of first optimization stage: optimization regarding maximum force capability.*

Parameter	Description	Values
	fixed	
V_{conv}	converter volume	0.25 cm^3
g	air-gap length	0.15 mm
Z_l	amplitude limit	2 mm
	variable	
$q_r = R_m/R_o$	ratio of magnet radius to outer radius	$[0.05, 0.95]$
$q_h = h_m/h_p$	ratio of magnet height to pole pitch	$[0.05, 0.95]$
$q_a = h_{conv}/R_o$	aspect ratio: total height to outer radius	$[2.95, 10.03]$
h_{lim}	height-limitation	(*'translator-'* or *'coil-limited'*)
n_p	number of poles on length-limiting part	$[1, 25]$
Δn_p	difference in pole numbers between parts	$[-5, 5]$

[3]The fill factor of a coil is defined as the ratio of the total cross-sectional area of the wires to the total cross-sectional area of the coil.

The permanent magnet material is modeled using the demagnetization curve of N48 grade NdFeB as shown in Fig. 6.2. The maximum energy density BH_{max} is 390 KJ/m^3 and the remanent flux density B_r is 1.42 T [112]. The soft-magnetic material is modeled using the magnetization curve of Vacoflux 50 as shown in Fig. 6.3. The magnetic flux density B_s at saturation is 2.35 T [170]. The computation of the resistance is based on the typical resistance of copper, $\rho_{Cu} = 1.7 \cdot 10^{-8}\Omega$m.

5.4.4. Optimal Geometry

Tab. 5.3 lists the optimal geometric parameter obtained from the optimization. It includes results for the two objective functions $\hat{D}_{max}$ and $\hat{D}_{mean}$ and the two cases of flux symmetry, odd and even. The six main parameters q_r, q_h, q_a, and Δn_p are listed on top, derived parameters at the bottom. As stated previously, that wire diameter d_w does not influence the force capability. However, for the second optimization stage, R_c and consequently d_w needs to be assigned a value. Thus, in Tab. 5.3 d_w is assigned a value and the resulting number of total windings, n_{tot}, as well as the coil resistance R_c is listed.

It can be seen that the resulting force capabilities as well as the optimal parameters are similar for the four cases. The radius of the magnets is about 75% of the total radius, the magnet height h_m is about 85% of the pole pitch, h_p. The aspect ratio is about 10, which is the maximum possible with the used constraints for the generator length, h_{conv}. The ratio of magnet height, h_m, to magnet radius, R_m, is also similar for all cases, which implies a similar operating point on the demagnetization curve. For the designs optimized using the objective function $\hat{D}_{max}$, the optimal pole pitch, h_p, is approximately equal to the amplitude limit, Z_l.

Fig. 5.6 shows the flux distribution for design A of Tab. 5.3. The soft-magnetic spacers between the magnets act as flux concentrators. Consequently, the generator has a higher flux gradient and thus a higher force capability than designs with only a single magnet, such as presented in [3, 67, 102, 156]. In Fig. 5.6 it can be seen, that the leakage flux, indicated by the closed flux lines lying entirely to the left of the coil, is small even though there is no iron in the return path.

In Fig. 5.7 the flux and the force capability are plotted as a function of the translator position. For the odd flux symmetry designs, $\hat{D}(z)$ is maximal at $z = 0$, whereas even flux symmetry designs have the maximum at $z \approx h_p/2$. Note, that the force capability $\hat{D}$ is quasi-

Table 5.3: *Optimal geometric parameters for* $V_{conv} = 0.25\,\mathrm{cm}^3, g = 0.15\,\mathrm{mm}, Z_l = 2\,\mathrm{mm}$

Objective function		$\hat{D}_{max}$		$\hat{D}_{mean}$	
Flux symmetry		odd	even	odd	even
Design		A	B	C	D
$q_{r,Opt}$		0.74	0.74	0.75	0.73
$q_{h,Opt}$		0.84	0.84	0.83	0.86
$q_{a,Opt}$		10.00	9.97	10.02	9.35
h_{tr} limited by		translator	translator	translator	translator
$n_{m,Opt}$		8	8	9	6
Δn_p		1	0	1	0
$\hat{D}_{max}$		0.32	0.31	0.30	0.30
$\hat{D}_{mean}$		0.16	0.17	0.17	0.20
n_c		9	8	10	6
h_m	[mm]	1.64	1.64	1.44	2.11
h_p	[mm]	1.95	1.95	1.74	2.46
R_o	[mm]	2.00	2.00	2.00	2.04
R_m	[mm]	1.48	1.48	1.50	1.49
h_m/R_m		1.11	1.11	0.97	1.42
t_c	[mm]	0.37	0.37	0.37	0.40
h_{tr}	[mm]	16.0	16.0	16.0	15.1
h_c	[mm]	17.55	15.6	17.4	14.8
h_{conv}	[mm]	20.0	20.0	20.0	19.1
d_w	[μm]	25	25	24	27
n_{tot}		12087	10608	12580	9384
R_c	[kΩ]	4.83	4.15	5.57	3.28
m	[g]	0.82	0.82	0.84	0.79

periodic with decreasing amplitudes for positions away from the center. The decreasing amplitudes are due to the decreased flux linkage as the translator moves out of the coil. The periods are approximately equal to the respective pole pitches, as expected.

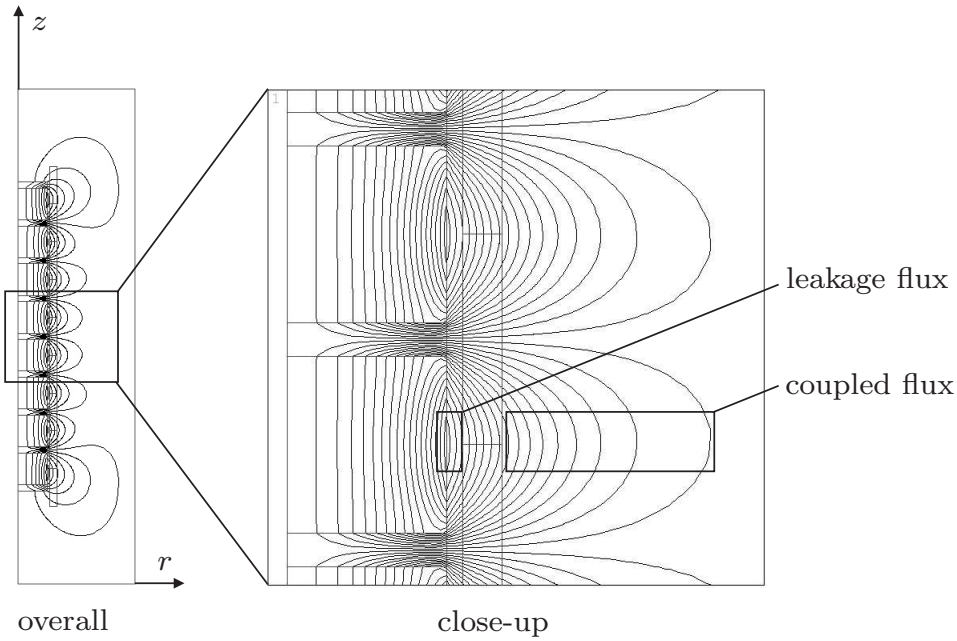

Figure 5.6: *Half cross-section of flux distribution for optimal generator design A of Tab. 5.3. left: Overall flux distribution, right: close-up view of the middle poles.*

5.4.5. Discussion

Used objective function

As can be seen in Tab. 5.3, the optimal parameters as well as the force capabilities as defined by $\hat{D}_{max}$ and $\hat{D}_{mean}$ are similar for both objective functions used. The deviation from the mean is below 10%. Fig. 5.7 shows that the force capability $\hat{D}(z)$ also has a similar shape in $[-Z_l, Z_l]$.

Therefore, the objective function $\hat{D}_{max}$ should be preferred as it requires less computation effort.

Flux symmetry

The optimal parameters as well as the force capability as defined by $\hat{D}_{max}$ and $\hat{D}_{mean}$ are also similar for both flux symmetries. However, the shape of $\hat{D}(z)$ for the two cases is fundamentally different as can be seen in Fig. 5.7. Therefore, similar values of $\hat{D}_{max}$ and $\hat{D}_{mean}$ does not necessarily imply that the four designs will also have similar output power for a given driving motion.

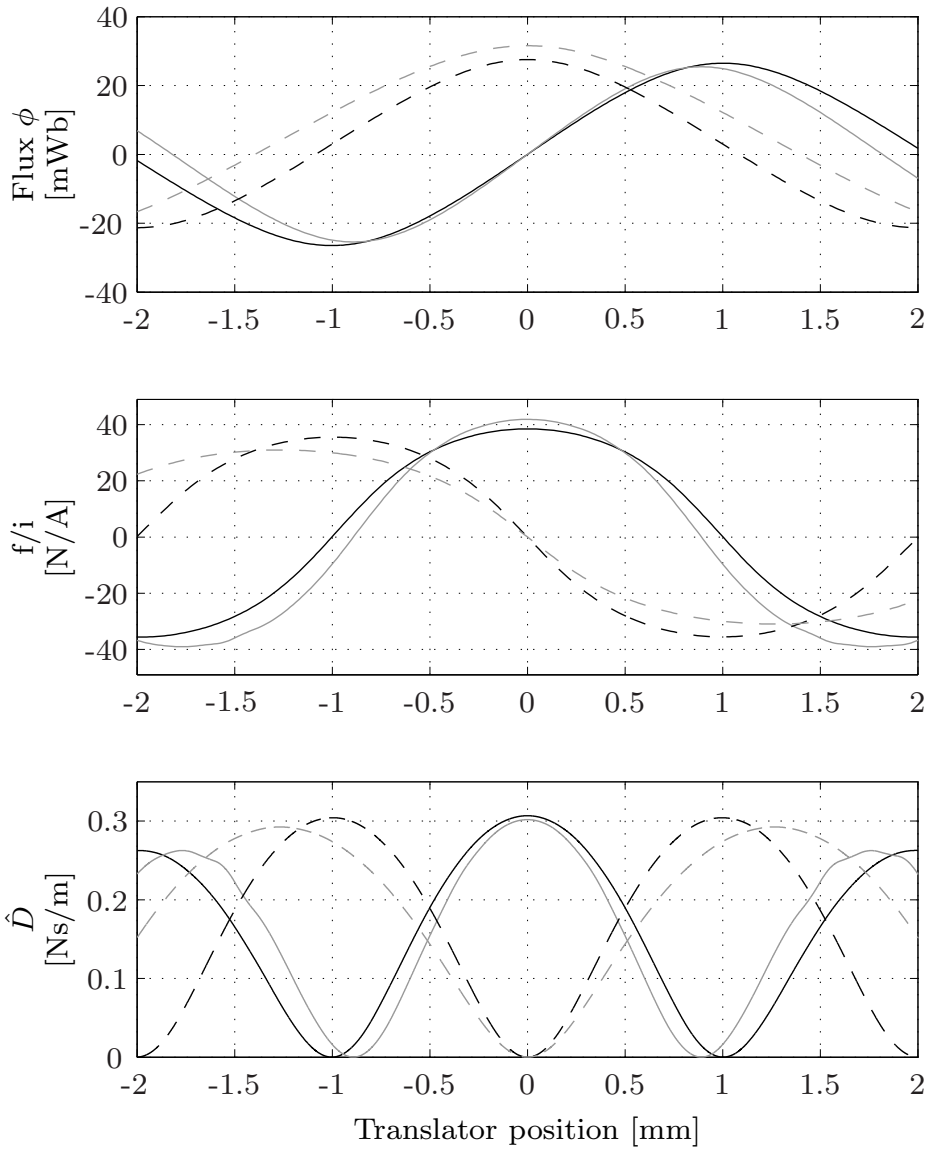

Figure 5.7: *Flux $\phi(z)$, force current ratio f/i, and force capability $\hat{D}$ versus position curves of the optimized designs (cf. Tab. 5.3). Dark gray lines correspond to objective function $\hat{D}_{max}$, light gray lines correspond to objective function $\hat{D}_{mean}$. Solid lines show systems with odd flux symmetry, dashed lines show systems with even flux symmetry.*

Optimal parameters

Inspecting Tab. 5.3 leads to the following observations:

- The aspect ratio of the magnets (ratio of magnet diameter to magnet height) is close to 1 for all designs. This implies that the

magnets have a similar operating point[4]. This operating point is near the point with maximum energy density BH_{max} of the used magnet material.

- The optimal q_r is at about 0.75 for all designs. In order to give insight about this value, Fig. 5.6 (showing the generator geometry with flux lines) is inspected. It can be seen that the return path of the magnetic flux lines through the air is located close to the magnets. Consequently, to couple maximal magnetic flux, the coils should be as thin as possible and located close to the magnets. However, the lower the coil thickness, the higher the coil resistance. Thus, the optimum represents the best trade-off between resistance and flux coupling.

- The optimal q_h can be explained as follows: The thin soft-magnetic spacers act as flux-concentrator and thus lead to a high gradient of the magnetic field in the vertical direction and consequently to a high flux gradient. However, this effect only occurs below saturation. A very high q_h leads to very thin spacers as well as magnetic saturation and is thus not optimal. Very low values of q_h lead to thick spacers relative to the magnets and thus the flux is not concentrated as much.

- The aspect ratio q_a is near its upper bound (due to the constraint $h_{conv} < 20\,\mathrm{mm}$) leading to long and thin generator geometries. This fact may suggest that the force capability increases generally for higher aspect ratio. However this hypothesis is false as further investigations have shown: when the upper bound for q_a is increased, an optimum is found which is not limited by the upper bound of q_a. Therefore, the high aspect ratio of the optimal design is probably a consequence of the chosen values of the fixed parameters.

- In all four designs, the total length h_{conv} is limited by the combined height of translator and its displacement range $h_{tr} + 2Z_l$. This may be due to the fact that a rather large displacement range $[-Z_l, Z_l]$ relative to the volume is used in the optimization.

- Δn_p is 0 or 1 in all designs, leading to similar values of coil height and translator height for each design. This is due fact that larger

[4]The operating point of a magnet is defined by a point on the magnet's demagnetization curve (see [31]).

differences in the lengths would lead to either unused magnet volume or unused coil volume.

- The results show that maximal force capability is not achieved by merely maximizing the number of magnets in the translator and hence maximizing the number of magnetic poles in the translator. This can be explained as follows: Increasing the number of magnets for a given stator geometry decreases the magnet's aspect ratio (ratio of magnet diameter to magnet height). This moves the operating point of the magnet due to its own demagnetization field and changes its ability to produce flux. Decreasing the aspect ratio beyond the optimum will reduce the magnets ability to produce flux.

Discussion of optimization method

In this optimization, the computation of the objective function relies on finite element analysis to compute the static magnetic field distribution for a given position of the generator. The main advantage of FEA compared to analytical methods is accurate determination of the static field solutions. This comes at the cost of long computation times. For example, to obtain an optimal generator geometry using the above described method has taken up to 2 weeks of continuous computation time on a Sun Blade 1500 workstation running at 1.5 GHz.

An optimization method based on analytical field solutions has been presented by Wang et al. in [175, 176]. However, the analyzed generator architectures contain soft-magnetic material in the stator, whereas the architecture optimized in this thesis does not. Baker et al. provide an approximation to compute the force capability of the same architecture as used in this thesis. However, their approximation is not accurate enough to serve as basis for an optimization.

5.5. Optimization of Spring and Load

5.5.1. Overall Goal

In the first optimization stage described in Sec. 5.4, stator and translator geometry have been optimized regarding maximum force capability. This section shows the second optimization stage which focuses on the bearing and the resistive electrical load.

The objective is to optimize the mechanical resonance frequency, f_n, and the load resistance, R_l, regarding mean electrical output power when the generator is driven by a given motion. Note, that the load resistance, R_l, not only represents the load, e.g. a sensor system connected to the generator, but also serves to adapt the damping force: a larger resistance leads to a lower current and consequently a lower damping force, cf. (2.15).

While previous work has only considered sinusoidal driving motion, this thesis uses acceleration waveforms measured at nine different points on the human body during walking. This is motivated by the fact that accelerations of points on the human body typically have a shape that is far from sinusoidal. In addition, the waveforms have a rich spectral content. Exemplary measured acceleration waveforms have been shown in Chapter 3.

5.5.2. Objective Function

Definition

The mean electrical output power, $\overline{P_{out}}$, is defined as the mean power dissipated in a resistive load, R_l, during a given time, T. In order to account for the maximum possible translator displacement, Z_l, the power is defined as zero if the translator collides with the end-stops, i.e. if $z > Z_l$.

$$\overline{P_{out}} = \begin{cases} \frac{1}{T}\int_0^T \frac{u_{R_l}^2}{R_l}\mathrm{d}t & \text{if } |z(t)| <= Z_l \ \forall t \in [0,T] \\ 0 & \text{otherwise} \end{cases} \tag{5.25}$$

Note that this treatment of end-stop collision has been used in Chapter 4 as well. As therein pointed out, generated power may be consequently underestimated.

The goal of the following optimization procedure is to *maximize* $\overline{P_{out}}$.

Computation

In order to compute the objective function (5.25), the system is simulated in Saber [168] using the lumped-parameter model presented in Fig. 2.3 of Chapter 2. For easier reference, the model is shown again in Fig. 5.8. The system input is a measured acceleration waveform $\ddot{y}$. The

simulation yields the relative translator position, $z(t)$, and the voltage, u_{R_l} across the load resistor. Subsequently, $\overline{P_{out}}$ can be computed. Mechanical losses, such as friction, are neglected.

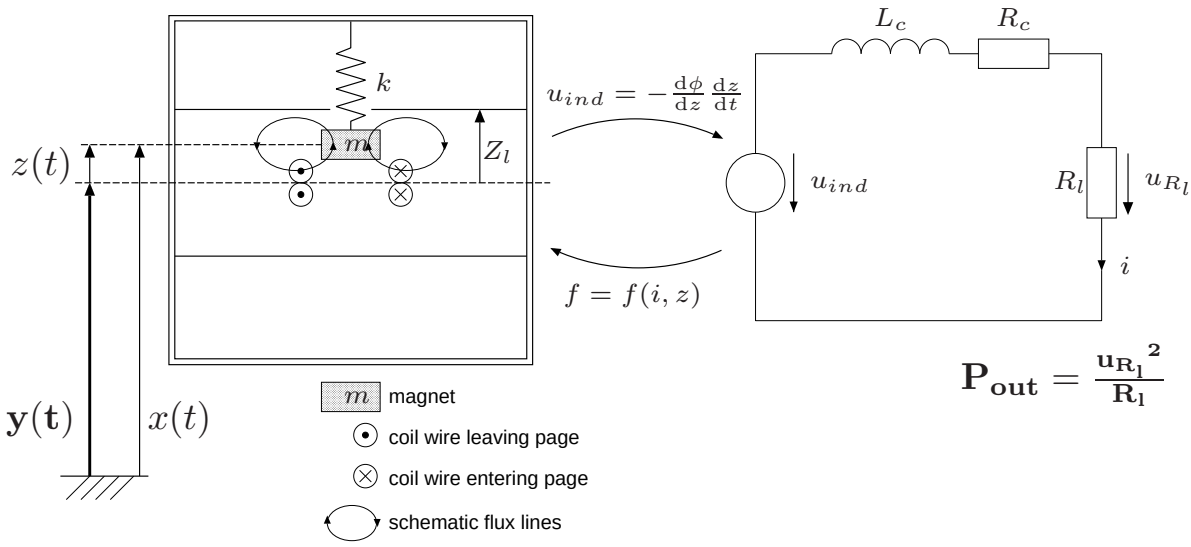

Figure 5.8: *Lumped parameter model of an electromagnetic generator (mechanical sub-model on the left, electrical sub-model on the right).*

In Fig. 5.8, R_c and L_c are the coil resistance and the coil inductance, respectively. R_l is the load resistance, m is the mass of the translator and k is the spring constant of the flexible bearing. $y(t)$, $x(t)$ are the absolute positions of generator frame and translator, respectively, $z(t)$ is the position of the translator relative to the generator frame. $\phi(z)$ is the magnetic flux through the stator coils and $f(i, z)$ is the damping force as a function of coil current, i, and translator position, z. The fixed system parameters, $\phi(z)$, $f(i, z)$, L_c, R_c, and m are extracted from the results of the first optimization stage.

The system input is the absolute motion of the generator frame and is given by the acceleration waveform $\ddot{y}(t)$.

5.5.3. Optimization Procedure

Fig. 5.9 shows a flow chart of the optimization procedure which has the same structure as the one used in the first optimization stage. The same optimization algorithm, adaptive simulated annealing, is used. However, in the second stage, the given parameters are stator and translator geometry, the variable parameters are the spring constant

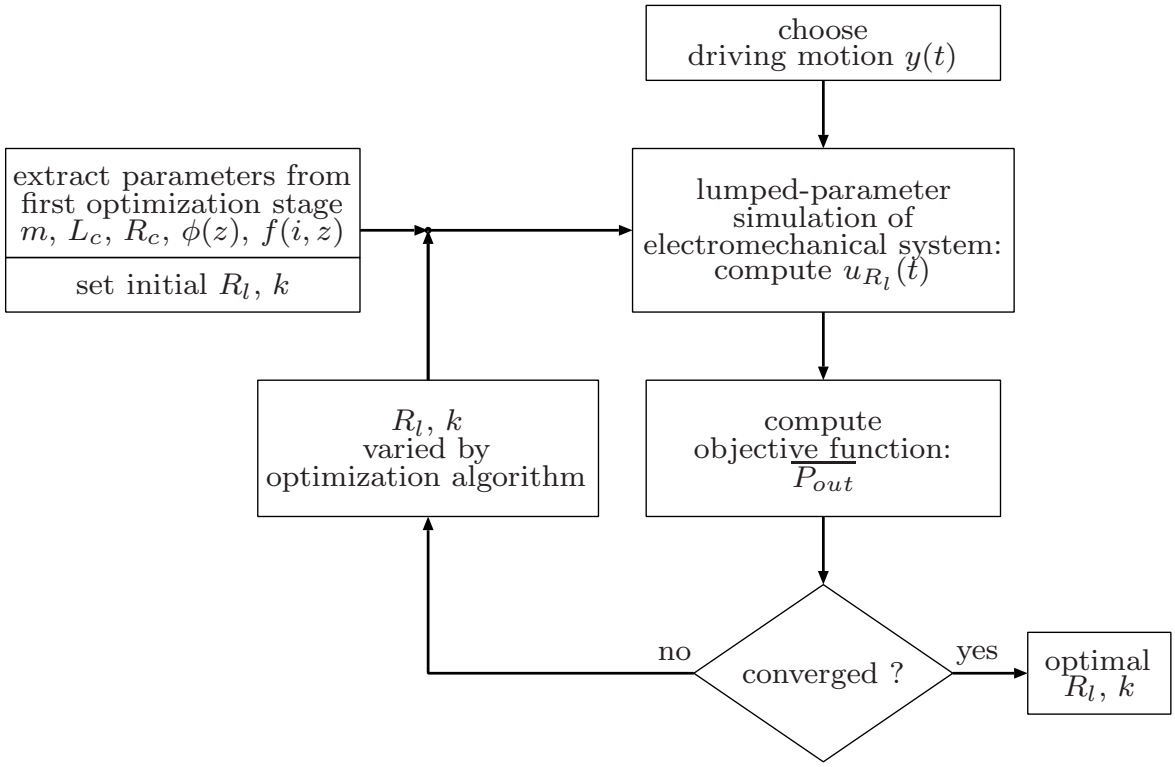

Figure 5.9: *Flow chart of second optimization stage: optimization regarding maximum output power.*

k (used to tune the resonance frequency f_n) and the load resistance R_l. The objective function is $\overline{P_{out}}$, given by (5.25). The second optimization stage has been applied to all four resulting designs from the first optimization stage (cf. Tab. 5.3).

The acceleration waveforms used in the optimization have been measured on nine different position on the human body during walking. The used measurement points are shown in Fig. 5.10 (replicated from Fig. 3.4 for easier reference), the measurement procedure is described in detail in Chapter 3. The waveforms for the system input $\ddot{y}(t)$ have been obtained by processing the original 3D measurement data as follows: From each 3D acceleration waveforms, a window of 10 seconds length has been selected. The 3D waveforms have then been projected onto an axis. This axis defines the generator orientation and thus the orientation of the translator oscillation relative to the body when the generator is mounted. Two different orientations have been selected to study their influence on electrical output power.

The first orientation is the one with maximum variance of the ac-

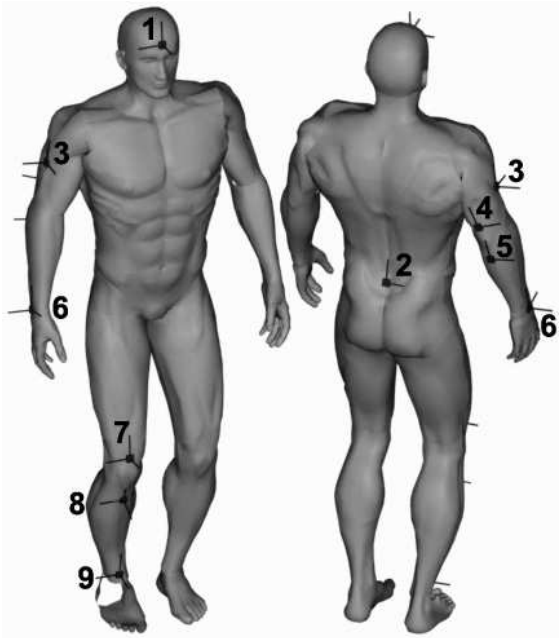

Figure 5.10: *Locations of acceleration measurement points on test subject.*

celeration, the second is the one with minimum DC acceleration.

The following ranges have been used for the variable parameters: R_l is allowed to vary between $0.01R_c$ and $100R_c$, k is allowed to vary in a range that corresponds to resonance frequencies, f_n, between 0.1 Hz and 120 Hz.

5.5.4. Generated Power

In Fig. 5.11(b) and 5.11(a), the generator output power values, $\overline{P_{out}}$, are shown for the generator orientations with maximum acceleration variance and minimum DC acceleration, respectively. The figure includes the four resulting designs from the first optimization stage.

It can be seen, that the generator orientation with maximum acceleration variance leads to less generated power. This is due to the fact that the used acceleration waveforms have a significant DC component. As explained in Subsec. 2.5.5 this causes a DC displacement of the translator and consequently a reduced available amplitude of the translator motion relative to the generator frame. A smaller amplitude in turn leads to lower translator velocity and lower generator power.

For the same generator orientation, the performance of the four different designs is similar. None of the designs has a consistently supe-

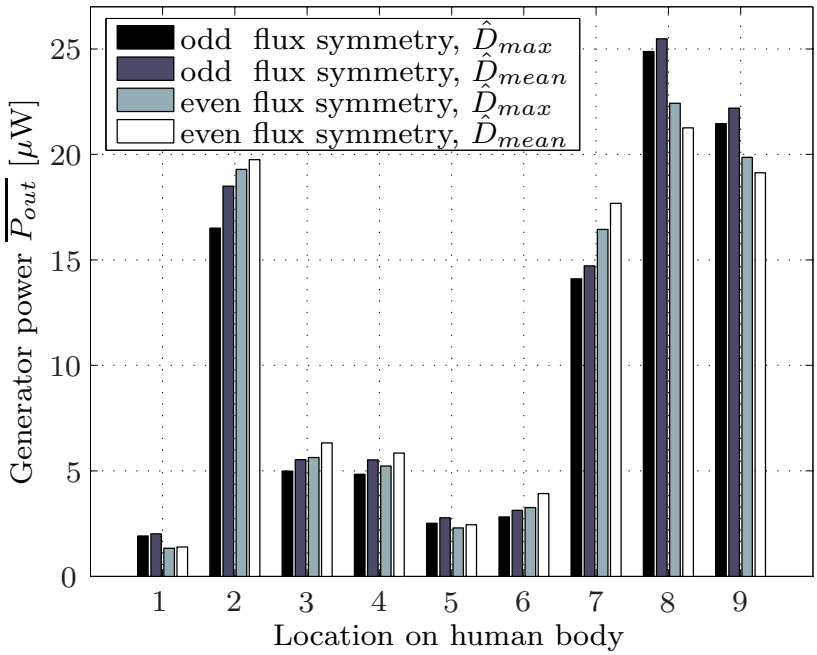

(a) generator orientation: minimum DC acceleration

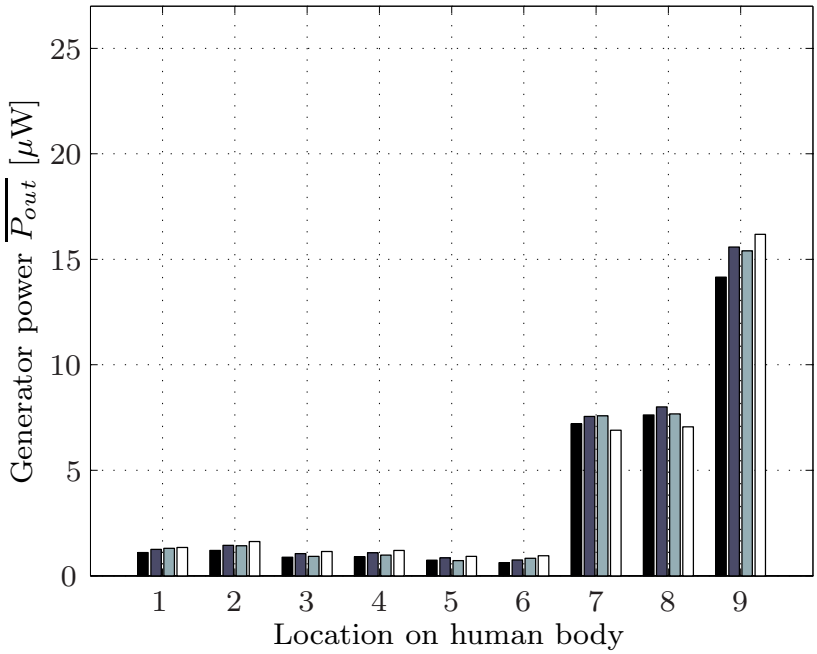

(b) generator orientation: maximum acceleration variance

Figure 5.11: *Generator power, $\overline{P_{out}}$, of the optimized generator architectures, considering two different generator orientations relative to the body. The numbers on the x-axis correspond to the measurement points of Fig. 5.10.*

rior performance. Thus it is concluded that for the given optimization setting, the flux symmetry of the generator does not have a significant influence on the generated power, even though the force capability $\hat{D}(z)$ has a very different shape for the two cases (cf. Fig. 5.7).

In addition, it can be seen that generally, locations on the lower body (locations 7-9) yield significantly more power than locations on the upper body (1, 3-6). This is caused by stronger accelerations on the lower body due to foot to ground impacts during walking. Location 2 leads to relatively low output power for the generator orientation with maximum variance, while for the other generator orientation, the output power is relatively large. This observation can be explained by inspecting Fig. 3.6. There, it can be seen that location 2 has larger peak to peak acceleration values in the lateral (horizontal) axis than the other locations on the upper body. These strong horizontal accelerations, however, can only be exploited by the generator orientation with minimum DC acceleration, since only this orientation is close to horizontal.

5.5.5. Optimal Resonance and Load Resistance

In Fig. 5.12, the optimal resonance frequency, f_n, and the optimal load resistance, R_l, are plotted for the two used generator orientations.

The optimal resonance frequencies for measurement points 1 to 6 are similar and significantly lower than the ones for measurement points 7 to 9. This can be explained by the stronger accelerations at the latter locations: a stiffer spring and thus a higher resonance frequency is needed to prevent collisions of the translator with the end-stops[5].

When comparing the optimal parameters for the two generator orientations, one observes that the optimal resonances for the maximum acceleration variance orientation are consistently higher than for the other orientation. This is due both to the larger accelerations as well as to the DC acceleration component. Both factors require a stiffer spring to prevent end-stop collisions. End-stop collisions can also be avoided by lowering the load resistance R_l and thus increasing the damping, however this reduces the electrical efficiency and thus the output power.

Inspecting Fig. 5.12 also shows that the optimal load resistance, R_l, is at least about the double of R_c for all cases[6], which means that the

[5]Note that the output power has been defined as 0 if collisions occur.

[6]The used R_c values are listed in Tab. 5.3.

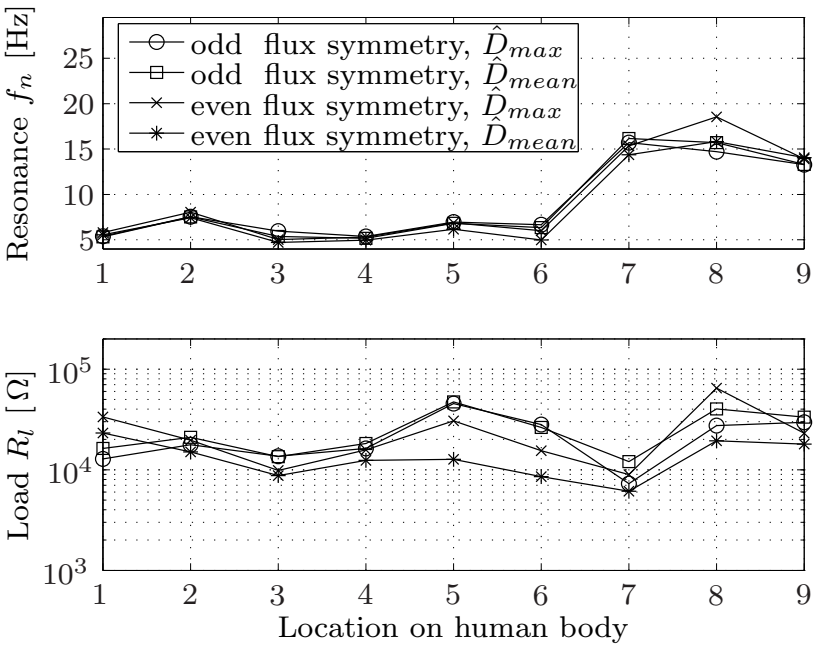

(a) generator orientation: minimum DC acceleration

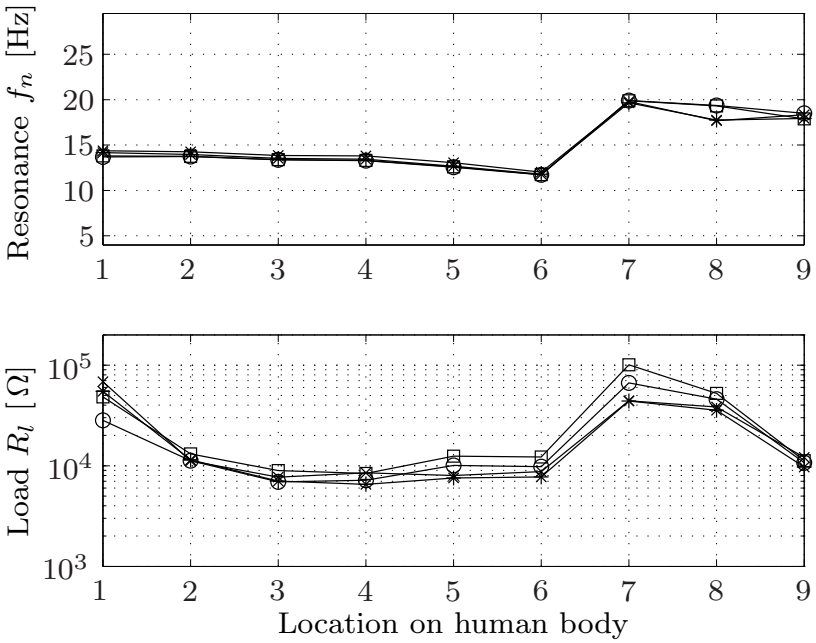

(b) generator orientation: maximum acceleration variance

Figure 5.12: *Optimal parameters of the optimized generator architectures, considering two different generator orientations relative to the body. The numbers on the x-axis correspond to the measurement points of Fig. 5.10.*

resistive energy loss in the coil resistance is less than a third of the total power and that the electrical efficiency is higher than 2/3.

Note, that the typical approach to equate the load resistance to the internal resistance is not valid here. This is due to the inertial operating principle of the generator (cf. Subsec. 2.3.1) Typically, the translator motion (e.g. its amplitude and frequency for the sinusoidal case) is given. In this case, using equal coil and load resistances maximizes the output power. However, in inertial generators, the translator motion is dependent on the load resistance because the load resistance influences the electrical damping force. As shown in Chapter 4, maximum output power for inertial generators is achieved by tuning the electrical damping force (by varying the load resistance) to an optimal value, which depends on the driving motion. The optimal value of the load is thus generally not the same as the coil resistance.

5.5.6. Sensitivity of Power to Generator Parameters

The sensitivity of output power to deviations of the spring constant k and the load resistance R_l from their optimal value has been analyzed for two reasons:

- The spring constant and hence the resonant frequency is typically not adjustable online during generator operation. However, different walking speeds as well as different mounting locations on the human body require different optimal resonant frequencies.
- The load resistance R_l is considered to be adjusted online to maximize power for varying driving motions. However, precise optimal tuning of R_l may require complex electronic circuits consuming significant electrical power themselves. Therefore, it is important to know how sensitive the generator output power is to deviations of the load resistance from its optimal value.

For the sensitivity analysis, the spring constant k and the load resistance R_l have been varied in 7 and 15 discrete steps to deviate $\pm 60\%$ from the optimum, respectively[7]. When varying the spring constant, the load resistance R_l, which is considered adjustable online, has been re-optimized each time. In contrast, the spring constant is regarded as fixed and has hence been held constant when varying the load resistance.

[7] A change of $\pm 60\%$ of the spring constant corresponds to a change of $-37\%, +26\%$ of the resonant frequency.

The sensitivity analysis has been carried for the design C Tab. 5.3. The relative output power values of the analysis are shown in Figs. 5.13 and 5.14. Note that for location 8, one point lies about 1% above the

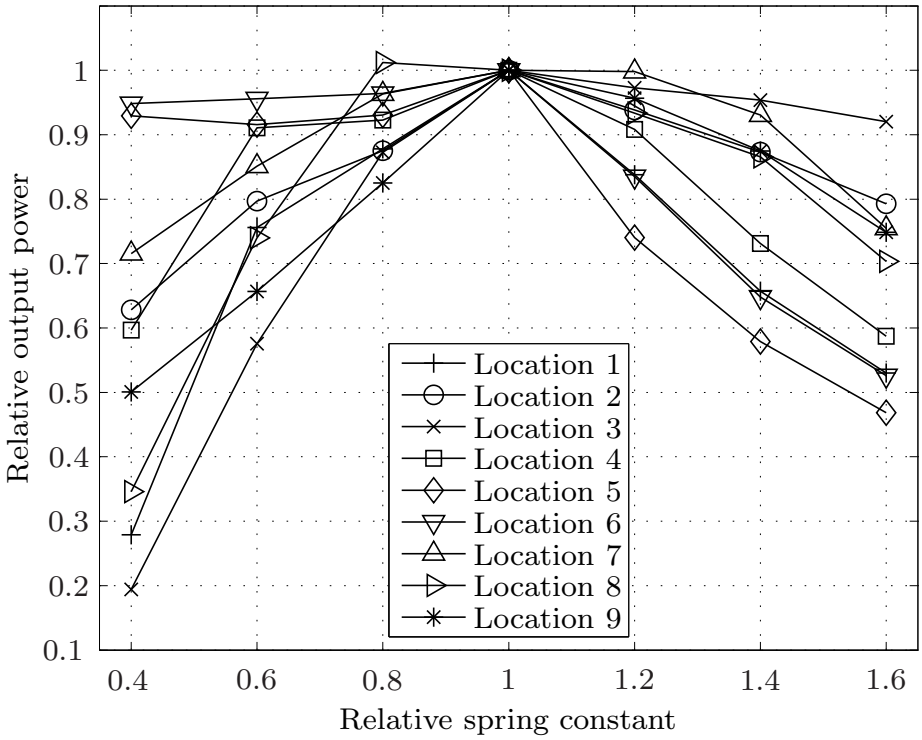

Figure 5.13: *Sensitivity of output power to variations of the spring constant for design C (cf. Tab. 5.3).*

original optimum. Hence, the originally computed optimum is slightly off. However, the error is small and only one case among a large number of cases is affected.

As can be seen in Fig. 5.13, varying the spring constant k by $\pm 60\%$ causes a power drop of less than 50% in the majority of cases. The exceptions are 1, 3, 8 for a deviation of -60% and location 5 for a deviation of $+60\%$.

Inspecting Fig. 5.14 shows that increasing the load resistance R_l leads to output power 0 in all cases. This can be explained as follows: The optimal values of R_l correspond to a translator motion which utilizes the full range of available displacement. If the resistance is increased beyond this value, the translator collides with the end-stops which leads to power 0 according to the definition of (5.25). A value of R_l below the optimum decreases the generated power no more than

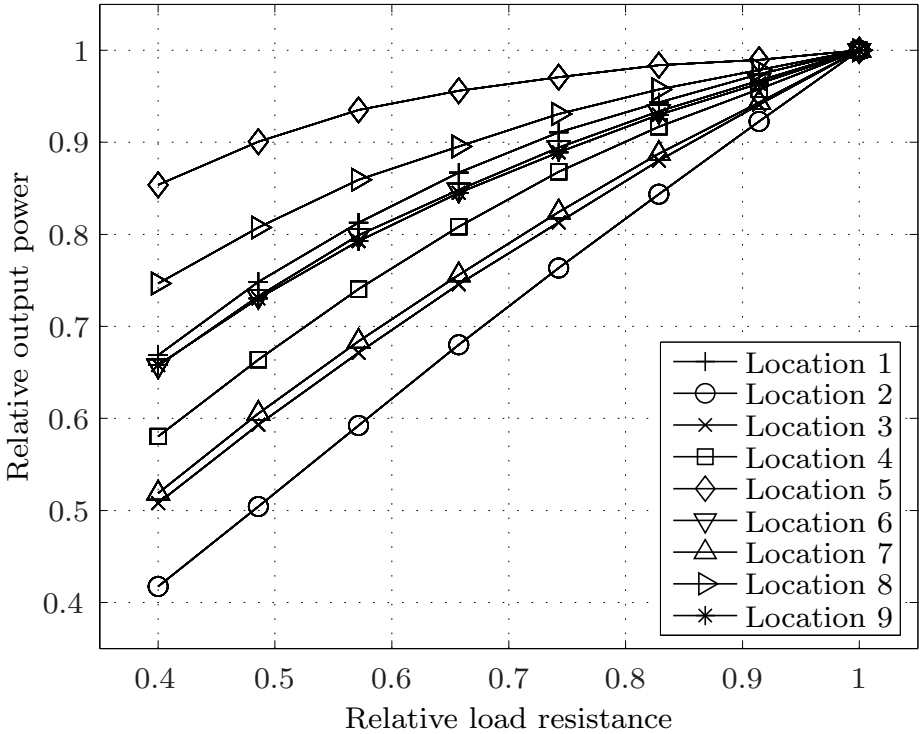

Figure 5.14: *Sensitivity of output power to variations of the load resistance for design C (cf. Tab. 5.3).*

50%, except for one case of measurement point 2.

5.6. Scaling Analysis

The above results have been obtained for fixed values of the volume V_{conv} and the air-gap length g. In order to gain more insight, the influence of these parameters on optimal geometry and generator performance has been analyzed. For each parameter, the analysis has been carried out as follows: The parameter is set to half the original value, the other parameter is kept constant. Both optimization stages are then executed. The same procedure is repeated with the parameter set to twice the original value.

As initial design only design C (cf. Tab. 5.3) has been considered. Thus, only the objective function $\hat{D}_{mean}$ and odd flux symmetry are used. In the second optimization step, only the generator orientation with minimum DC acceleration has been analyzed.

Tab. 5.4 shows the optimal geometry parameters resulting from the

first optimization step of the analysis. It can be observed that q_r and q_h

Table 5.4: *Influence of scaling on optimal parameters*

		Design C	V_{conv} scaled		g scaled	
g	[mm]	0.15	0.15	0.15	0.075	0.30
V_{conv}	[cm^3]	0.25	0.125	0.5	0.25	0.25
$q_{r,Opt}$		0.75	0.71	0.74	0.79	0.69
$q_{h,Opt}$		0.83	0.86	0.88	0.81	0.83
$q_{a,Opt}$		10.02	14.18	6.09	10.03	10.01
$n_{m,Opt}$		9	10	3	10	9
Δn_p		1	1	1	1	10
h_m	[mm]	1.44	1.30	3.99	1.27	1.45
R_m	[mm]	1.50	1.00	2.20	1.57	1.38
h_m/R_m		0.97	1.30	1.81	0.81	1.05
R_o	[mm]	2.00	1.41	2.97	2.00	2.00
h_{conv}	[mm]	20.0	20.0	18.1	20.0	20.0

have similar values in all cases which provides evidence that the optima are relatively insensitive to the scaling of volume and air-gap length.

In addition, this result differs from the findings for a similar architecture (same topology but with soft-magnetic iron around the stator coils) in [176]. There, it was found that q_h should be as close to 1 as possible for maximum force capability. The difference is probably due to the fact that the model in [176] neglects saturation, which occurs for high q_h values.

5.6.1. Influence of Volume

Fig. 5.15 shows, relative to the initial design, the force capability and the mean output power $\overline{P_{out}}$, respectively, when halving or doubling the volume $V_{conv0} = 0.25\,\text{cm}^3$.

While only $\hat{D}_{mean}$ has been used as objective function in the first optimization step, both $\hat{D}_{max}$ and $\hat{D}_{mean}$ are shown in the plots. As the different optimal designs have different translator masses, $\overline{P_{out}}$ is also shown normalized by the respective translator mass.

As can be seen, increasing the volume V_{conv} increases the force capability by about the same factor, however the output power increases by a smaller factor while the normalized output power decreases slightly. This is in contrast to an ideal VDRG ($R_c = 0$, $\hat{D}(z) = constant$) where

the normalized output power stays constant, e.g. the output power is proportional to the translator mass. The decrease of the normalized power may be caused by the generator not being able to provide the required electrical damping force. Consequently, a higher spring constant is needed to prevent collisions of the translator with the end-stops which lowers the electrical output power.

5.6.2. Influence of Air-Gap Length

Fig. 5.16 shows, relative to the initial design, the force capability $\hat{D}$ and the mean output power $\overline{P_{out}}$, respectively, when halving or doubling the air-gap length $g_0 = 0.15\,\mathrm{mm}$. Again, both $\hat{D}_{max}$ and $\hat{D}_{mean}$ are shown in the plots.

It can be seen that doubling the air-gap length leads to a power drop of about 50%. This is due to increased leakage flux in the air-gap. For half the original air-gap length the power is increased by about 20 to 50%. The power normalized by the translator mass is less sensitive to air-gap length variations. Hence, the changes of the (not normalized) output power are partially due to the variations of the translator mass.

5.7. Discussion

The power values determined in this chapter can be compared with the estimated power values for the VDRG in Chapter 4 by inspecting Fig. 4.6. The intersection of the vertical line at the used value for Z_l and the plotted curves for the VDRG yields the predicted power value. The value for Z_l used in this chapter ($Z_l = 2\,\mathrm{mm}$) leads to predictions of about $20\,\mu\mathrm{W}$ for the upper body and $80\,\mu\mathrm{W}$ for the lower body. Thus, the predictions for the VDRG are about 4 times higher than the values reached by the designed electromagnetic generator. The reasons for the discrepancy are the following:

- In Chapter 4, the DC component of the driving acceleration waveforms has been subtracted for the simulations to allow comparisons between the generator classes. In this chapter, however, the DC component is included, in order to reflect realistic operation conditions. As explained Subsec. 5.5.4, the DC component reduces generator power.

- For the VDRG of Chapter 4 the ratio of electrical damping force to translator or mover velocity D is constant and is allowed to take

any value, whereas for the electromagnetic generator analyzed in this chapter, the force velocity ratio is a function of the translator position z and is dependent on the generator geometry.

- The loss of electrical energy in the stator coils is not considered in Chapter 4.

5.8. Conclusions

In this chapter it has been shown that it is possible to generate between 2 and 25 μW using a body-worn electromagnetic generator with a stator-translator volume of 0.25 cm^3. The output power depends on the generator mounting location on the human body and the driving motion. The achieved power levels are sufficient for many sensing applications.

The results are based on a novel linear inertial electromagnetic generator architecture. The architecture is based on the combination of a tubular air-cored electromagnetic generator and a flexible parallel-spring bearing. This architecture has a high electromagnetic force capability and low mechanical damping, which enables high-efficiency operation.

In order to optimize the generator design parameters, an optimization method has been presented. The method is based on two stages. The first stage uses electromagnetic finite element analysis to find the geometry of the generator that yields maximum electrical damping force. The second stage uses the geometry of the first stage and finds the resonance frequency and electrical load which lead to maximum electrical output power.

The optimization results show that the optimal values for some geometric parameters are independent from generator volume. In addition, it has been shown, that the optimal resonant frequencies are not simply at the fundamental frequency of the human motion, as often assumed. Instead, they are significantly higher, which leads to higher output power than previously estimated.

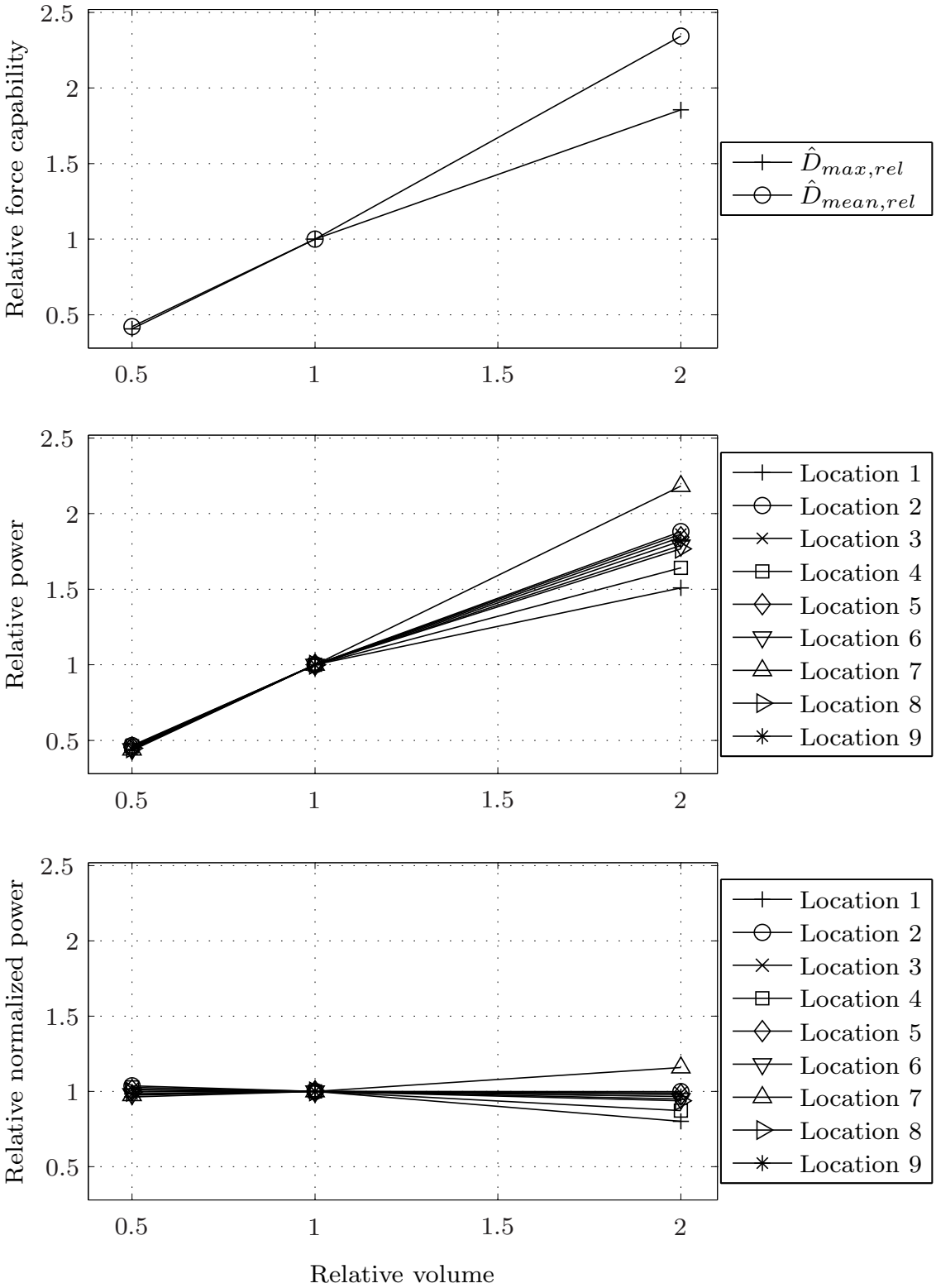

Figure 5.15: *Influence of volume V_{conv} on force capability $\hat{D}$ (top), output power $\overline{P_{out}}$ (middle), and output power normalized by mass $\overline{P_{out}}/m$ (bottom). The used volumes are $V_{conv} = 0.125\,\mathrm{cm}^3$, $V_{conv,0} = 0.25\,\mathrm{cm}^3$, and $V_{conv} = 0.5\,\mathrm{cm}^3$. All values are relative to the values of design C of Tab. 5.3.*

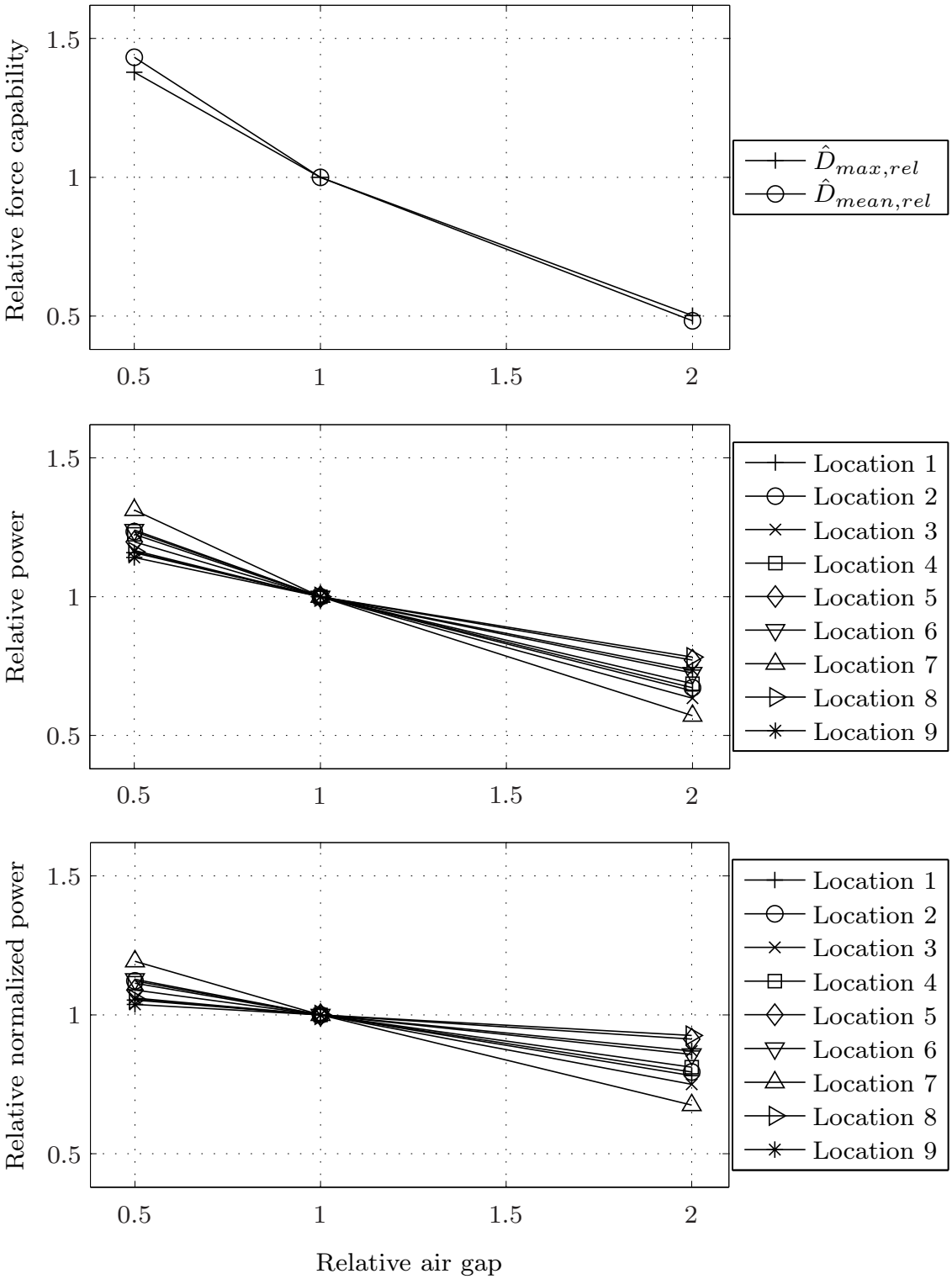

Figure 5.16: *Influence of air-gap length g on force capability $\hat{D}$ (top), output power $\overline{P_{out}}$ (middle), and output power normalized by mass $\overline{P_{out}}/m$ (bottom). The used air-gap lengths are $g = 0.075\,\mathrm{mm}$, $g_0 = 0.15\,\mathrm{mm}$, and $g = 0.3\,\mathrm{mm}$. All values are relative to the values of design C of Tab. 5.3.*

6

Experimental Validation

The previously used FE stator-translator model and the lumped-parameter system model are validated in this chapter. To this end, a prototype is designed and fabricated using standard precision engineering methods. The prototype includes the complete mechanical and electromagnetic structure necessary for generator operation. Based on measurements on the operating generator, key mechanical and electrical parameters are extracted and compared with simulation results.

6.1. Generator Prototype

Three prototypes, based on the geometric parameters listed in Tab. 6.1, have been fabricated to validate the FE model used in Sec. 5.4 and the lumped-parameter system model used in Sec. 5.5. In addition, generated power is measured for a body-worn generator during walking.

6.1.1. Design

Cross-sections of the designed generator device, seen from the side and from top, are shown in Fig. 6.1(a) and Fig. 6.1(b), respectively. Note,

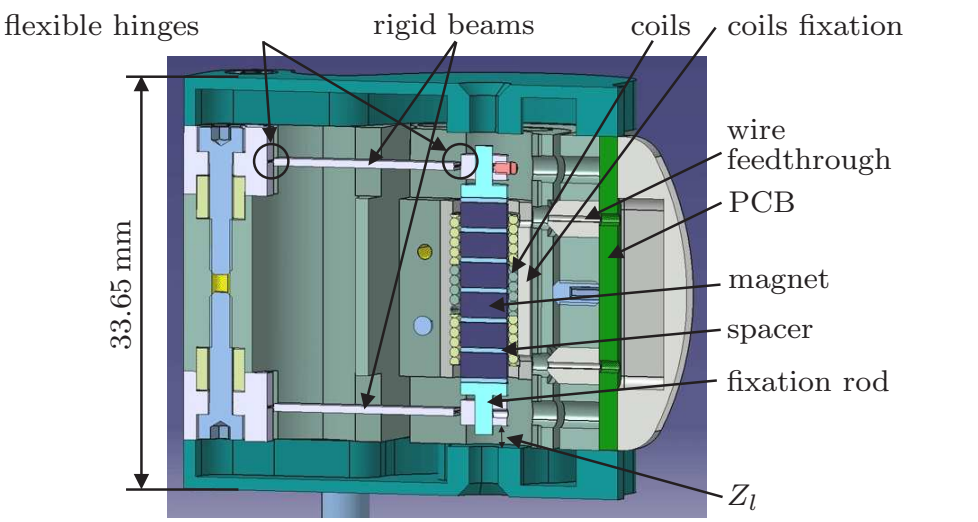

(a) Lateral cross-section

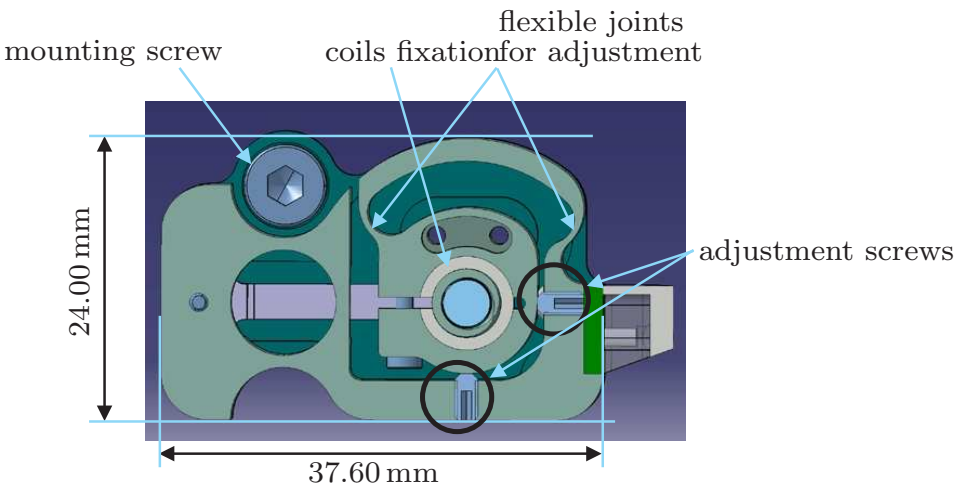

(b) Top cross-section

Figure 6.1: *Drawings of prototype design*

that two fixation rods have been added to the translator to allow attachment to the bearing. A printed circuit board (PCB) is mounted on the housing. The connection wires of the coil are threaded through a wire feedthrough and soldered on the PCB. A connector (not shown) is soldered on the PCB for external connection. A fixation made from POM (polyoxymethylene, a polymer material) is used to clamp the coil and attach it to the generator housing. The two adjustment screws and flexible joints shown in Fig. 6.1(b) are used to adjust the lateral position of the coil relative to the translator. Thus a uniform air-gap can be set. Note that most of the volume and weight of the prototype is used for the flexible coil adjustment joints and for the generator housing. The complete structure weighs about 43 g, however, the combined mass of coils, coils fixation, bearing, and translator is only 3.68 g.

6.1.2. Specifications of Stator and Translator

The generator size of the fabricated generator prototypes is chosen larger than the value used in the optimizations of Chapter 5 in order to simplify fabrication. The fabricated generator design has a combined stator and translator volume of $V_{conv} = 0.49\,\mathrm{cm}^3$ which is twice as large as the value used in the optimizations of Chapter 5. However, the prototype can still serve its main purpose: the validation of the simulation models.

The geometric specifications of stator and translator are listed in Tab. 6.1. The meaning of the parameters has been shown graphically in Fig. 5.1. Since the generator has an odd difference between number of magnets n_m and number of coils n_c, the flux function $\phi(z)$ will have odd symmetry. The parameter m_{eff} is the mass that in conjunction with the spring constant effectively determines the resonant frequency of the generator. m_{eff} includes the mass of the translator, fixation rods, and contributions of the rigid beams.

The used permanent magnet and soft-magnetic materials are the same as in Sec. 5.4:

- The permanent magnet material is N48 grade Neodymium-Iron-Boron [112] with a maximum energy density BH_{max} of $390\,\mathrm{KJ/m}^3$ and a remanent flux density B_r of 1.42 T. The demagnetization curve is shown Fig. 6.2.

- The used soft-magnetic material is Vacoflux 50 [170]. The magnetic flux density at saturation B_s is 2.35 T The initial magnetization curve is shown in Fig. 6.3.

Table 6.1: *Nominal specifications of stator and translator.*

V_{conv}	0.49 cm^3	n_m	6	n_c	5
h_{conv}	18.05 mm	h_{tr}	14.45 mm	t_c	0.8 mm
m	1.37 g	h_m	2.0 mm	d_w	31.5 μm
m_{eff}	1.69 g	h_s	0.35 mm	d_{wi}	25 μm
g	0.15 mm	R_m	2.0 mm	n_{tot}	9250
Z_l	1.8 mm	R_o	2.95 mm	R_c	5.13 kΩ

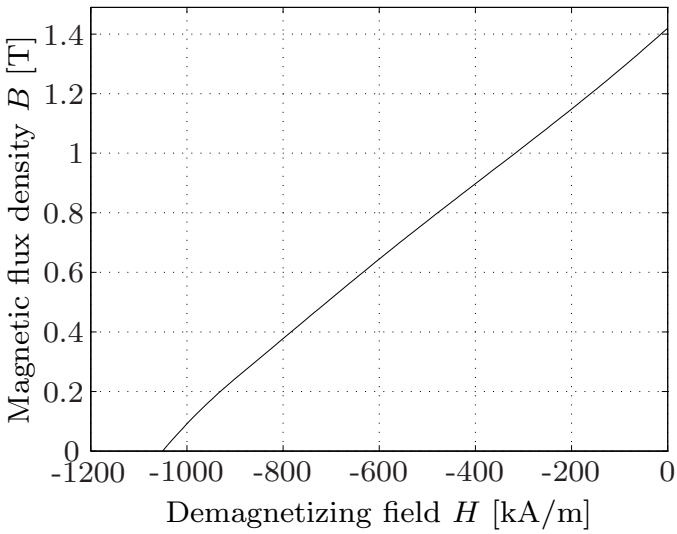

Figure 6.2: *Demagnetization curve of permanent magnet material N48 NdFeB*

6.1.3. Specifications of Bearing

The specifications of the bearing geometry are listed in Tab. 6.2 with graphical illustration in Fig. 5.3. E is the elastic modulus of the material used for the flexible bearing. The spring constants listed in Tab. 6.2 are computed in two ways: k_{an} is based on (5.2), whereas k_{FEA} is computed using finite element analysis. As can be seen, there is a significant difference between the values.

Based on the calculated spring constants and the effective translator mass, the undamped resonant frequency f_n can be computed by (2.3):

$$\text{based on FEA } f_n = 21.1\,\text{Hz} \tag{6.1}$$

$$\text{based on (5.2) } f_n = 18.5\,\text{Hz} \tag{6.2}$$

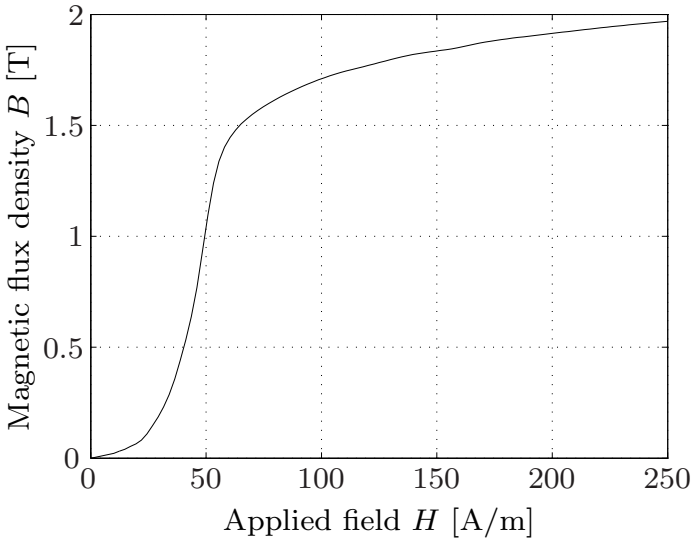

Figure 6.3: *Magnetization curve of soft-magnetic material Vacoflux 50.*

Table 6.2: *Nominal specifications of bearing.*

e	30	μm
b	3	mm
r	2.5	mm
w	0.6	mm
l	16.2	mm
E	$71.5 \cdot 10^9$	N/m^2
k_{FEA}	29.75	N/m
k_{an}	22.80	N/m

6.1.4. Fabrication

The flexible bearing and the generator housing consist of aluminum EN AW-7010 and have been fabricated using wire-discharge machining and milling. The magnets are N48 grade NdFeB magnets [112], the soft-magnetic spacers are made from Vacoflux 50 material [170]. Magnets, spacers, and fixation rods have been assembled and glued together by hand using a fixture made from Teflon. Pictures of the fabricated prototype are shown in Fig. 6.4.

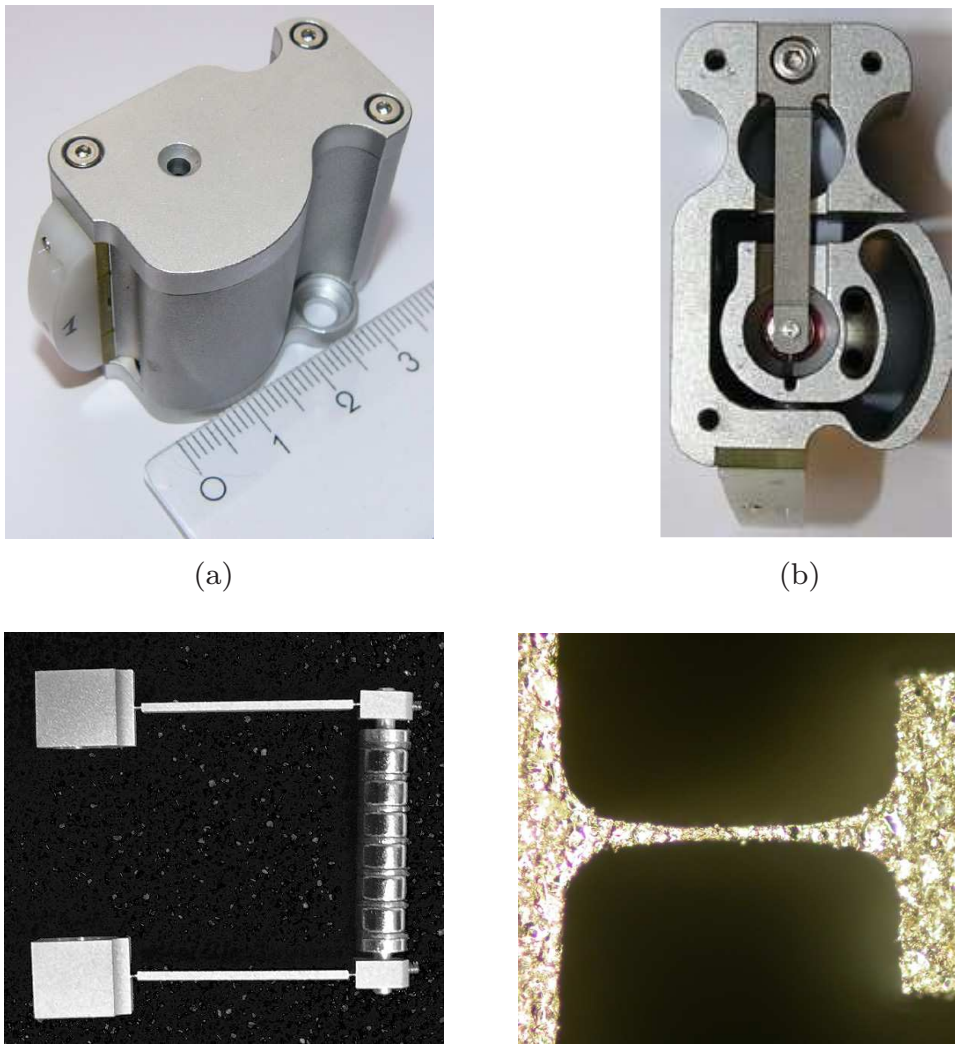

(a) (b)

(c) (d)

Figure 6.4: *Fabricated Prototype: (a) encapsulated generator, (b) open generator, seen from top, (c) bearing and translator (d) close up of notch hinge.*

6.2. Experiments

Three different types of measurements have been carried out on the prototypes, one with sinusoidal driving motion, one with initial displacement excitation, and one with the generator mounted on the human body. The experiments are described in the following subsections.

6.2.1. Sinusoidal Driving Motion

The generator is mounted on a table-mounted shaker that generates a sinusoidal driving motion. A laser vibrometer and a data acquisition interface is used to simultaneously record relative translator position $z(t)$ and load voltage $u_{R_l}(t)$. The laser vibrometer can also be used to measure the absolute position $y(t)$ of the generator housing. However, only one position signal can be acquired at a given time.

The purpose of the measurements is to determine the flux function $\phi(z)$, compare it with the predictions and thus to validate the used electromagnetic FE model. In addition, the measurement of $z(t)$ for a given driving acceleration $\ddot{y}(t)$ allows to validate the used lumped-parameter system model of the generator.

A schematic drawing of the measurement setup is shown in Fig. 6.5, while a picture can be seen in Fig. 6.6. In the setup the generator is

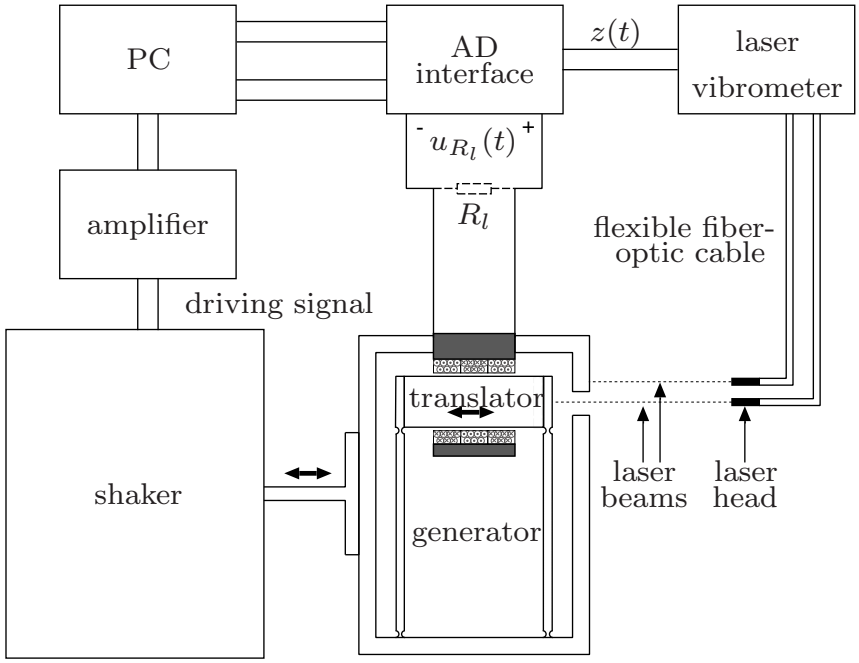

Figure 6.5: *Schematic drawing of measurement setup.*

mounted on a shaker. The mover position $z(t)$ relative to the frame is measured using a differential laser vibrometer (Polytec OFV 512 Fiber Interferometer). The vibrometer determines relative translator displacement from the Doppler shift of back-scattered laser light. In order to measure $z(t)$ one laser beam is focused on the generator housing while the other beam is focused on the translator

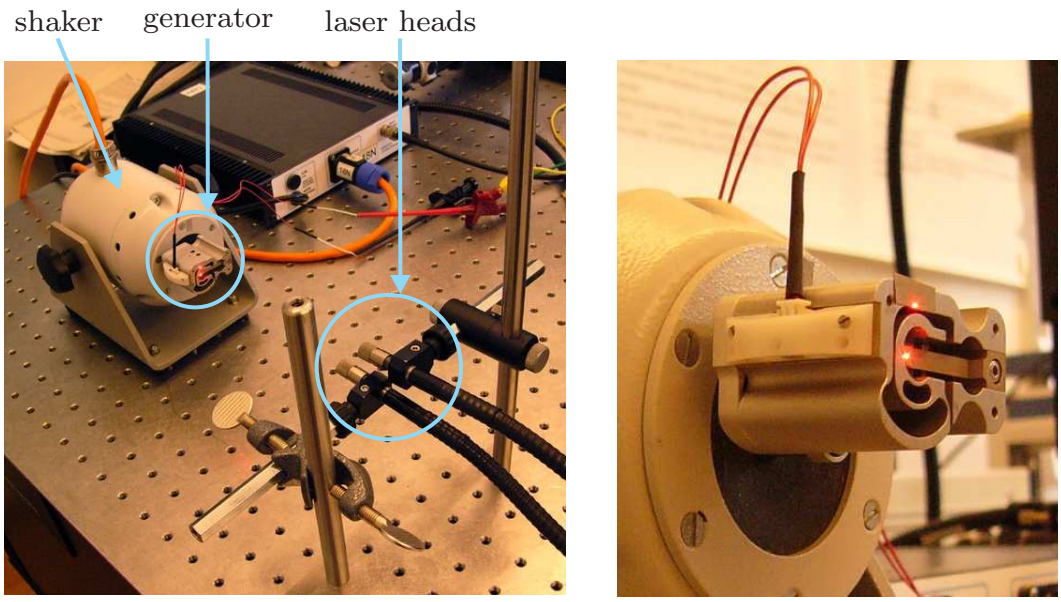

(a) (b)

Figure 6.6: *(a) Picture of measurement setup, (b) the two laser spots used to determine relative translator motion $z(t)$.*

The acquisition of position signal and generated voltage as well as the generation of the shaker driving signal is performed by LabView Software [122]. The used sampling frequency is 800 Hz.

6.2.2. Decaying Oscillations

The generator is mounted on a table and a short impulse is applied to the translator by tapping it slightly which leads to a decaying oscillating motion. As above, relative position and load voltage are measured. From the decay rate of the oscillations in open-circuit mode, the parasitic mechanical damping can be determined. Similarly, the combined electrical and mechanical damping can be analyzed when a load resistance is connected to the generator.

6.2.3. Body-Mounted Operation

The generator is mounted on the human body using an elastic fixture. In this setting only the voltage $u_{R_l}(t)$ is recorded. Subsequently, the electrical output power of the generator can be calculated. Thus, these measurements serve as realistic examples of how much electrical power can be obtained when the generator is worn on the body.

6.3. Mechanical Properties

6.3.1. Validation of Predicted Properties

The mechanical properties of the generator, undamped resonant frequency f_n and mechanical damping δ_m can be determined by analyzing the frequency and decay rate of the free oscillating translator after it has been excited by a short impulse. For this analysis it is assumed that the mechanical damping is proportional to translator velocity. Thus, the translator motion can be described by:

$$z(t) = Ae^{-\delta_m t} \sin(\omega_e t + \theta) \tag{6.3}$$

where A is the initial amplitude, δ_m is the mechanical damping, ω_e is the eigenfrequency of the system and θ is the phase shift.

For all three generator prototypes, decaying motions have been measured and the above equation has been fitted to the measured translator motion $z(t)$. In Fig. 6.7 both the measured and the fitted $z(t)$ are plotted. Evidently, the fitted curve matches the measured curve well.

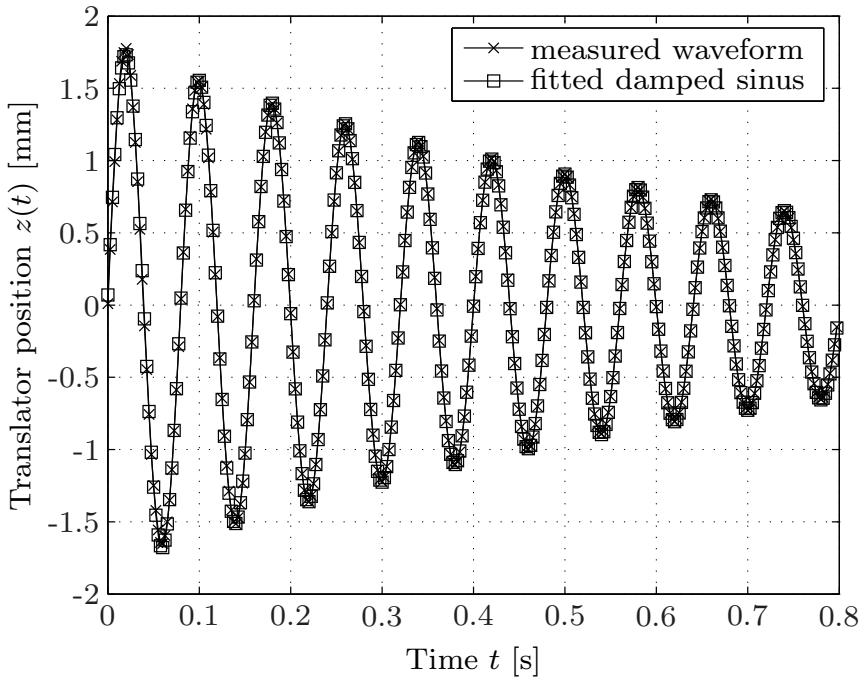

Figure 6.7: *Mechanical damping: Measured and fitted translator position $z(t)$.*

From the fitted values of ω_e and δ_m, the following parameters have been calculated:

$$\omega_n = \sqrt{\omega_e^2 + \delta_m^2} \tag{6.4}$$

$$f_e = \frac{\omega_e}{2\pi} \tag{6.5}$$

$$f_n = \frac{\omega_n}{2\pi} \tag{6.6}$$

$$Q_m = \frac{\omega_n}{2\delta_m} \tag{6.7}$$

$$D_m = 2m\delta_m \tag{6.8}$$

where Q_m is the mechanical quality factor and D_m is the mechanical damping constant.

The measured mechanical generator properties are listed in Tab. 6.3.

Table 6.3: *Measured mechanical system parameters.*

	fitted		derived		
	f_e [Hz]	δ_m [rad/s]	f_n [Hz]	Q_m [1]	D_m [Ns/m]
predicted by FEA	-	-	21.10	-	-
predicted by (5.2)	-	-	18.5	-	-
generator 1	12.484	1.33	12.486	29.5	0.0045
generator 2	16.063	1.38	16.064	36.4	0.0047
generator 3	14.159	1.77	14.162	25.1	0.0060

As can be seen, finite element analysis (FEA) and the approximation of (5.2) overestimate f_n up to 70%. In addition, there is a variation in the natural frequency between the specimens of about ±12%, indicating that it is difficult to control resonance precisely. The deviations may be caused by the following:

- *Fabrication tolerances:* As can be seen from (5.2) small deviations in the thickness e of the notch hinges have an influence on the spring constant k that is stronger than quadratic. However, measurements on the fabricated prototypes have shown that the actual e deviates less than 3.3% from the specified value (1 μm relative to nominal value of 30 μm). According to (5.2) this leads

to a deviation in k of less than 8.5%. Consequently, the error in the resonant frequency f_n is 4.2%.

- *Surface roughness:* Henein et al. have stated the hypothesis that surface roughness may reduce the effective thickness e of flexible hinges and thus lower stiffness and resonant frequency [64].

6.3.2. Influence of Air-Damping

There are typically three types of air damping in micro systems (cf. Fig. 6.8, [13]):

- *Slide-film damping:* Slide-film damping is caused by two surfaces moving relative to each other in close distance.
- *Squeeze-film damping:* This type of air-damping is caused by a surface oscillating perpendicularly to another surface in close distance.
- *Drag-force damping:* Drag-force is the force that is exerted on an object moving in air.

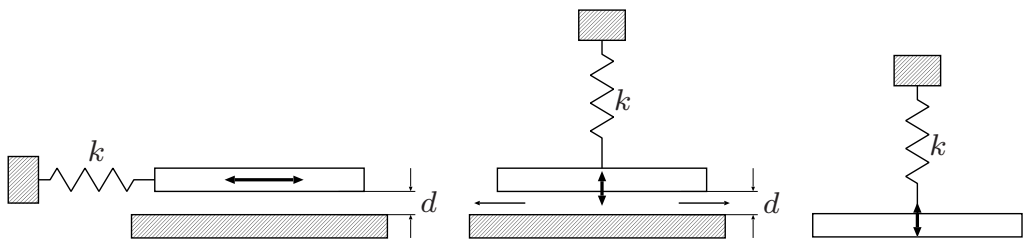

(a) Slide-film damping (b) Squeeze-film damping (c) Drag-force damping

Figure 6.8: *Types of air-damping in microsystems according to [13].*

In the used generator architecture, there is both slide-film damping between translator and stator as well as drag-force damping caused by the oscillating beams of the flexible bearing. Below, the influence of these two damping types is approximately determined.

Slide-film damping

According to [13] the quality-factor of an oscillator affected by slide-film damping can be approximated by

$$Q_{Cd} = \frac{m\omega d}{\mu A} \tag{6.9}$$

where m is the mass of the oscillating body, ω is the angular frequency, d is the distance between the moving and the non-moving surface, μ is the coefficient of viscosity of air, and A is the surface area affected by the damping. The above equation is only valid if

$$\omega \ll \frac{\mu}{\rho_{air} d^2} \tag{6.10}$$

where ρ_{air} is the density of air.

The parameters used to compute the slide-film damping of the generator prototype are listed in Tab. 6.4. These values represent the limit

Table 6.4: *Parameters used to compute slide-film damping.*

Parameter in (6.9)	Design parameter	Value	Unit
m	m	1.69	g
ω		$2\pi \cdot 15$	rad/s
d	g	0.15	mm
μ		$1.82 \cdot 10^{-5}$	$\mathrm{Ns/m^2}$
A	$l_c(2\pi(R_m + g))$	158.7	$\mathrm{mm^2}$
ρ_{air}		1.20	$\mathrm{kg/m^3}$

of validity of (6.9), however for smaller values of d the condition is clearly fulfilled.

The quality factor then becomes $Q_{Cd} = 8270$.

Drag-force damping

In [13] the drag-force damping of a vibrating beam is approximated by

$$Q_{sn} = 3\pi\rho_b B h \omega_n 256\mu \tag{6.11}$$

where ρ_b is the density of the beam material, B is the width of the beam, h is the thickness of the beam and ω_n is the resonant frequency.

In the generator prototype the beam material is aluminum with a density of $\rho_b = 2830 kg/m^3$, the beam width is $B = 3\,\mathrm{mm}$, and the beam thickness is $h = 0.6\,\mathrm{mm}$.

The quality factor then becomes $Q_{sn} = 971$.

Discussion

Both the computed quality factor for slide-film and drag-force damping are much higher than the quality factors determined in Tab. 6.3, thus the influence of slide-film and drag-force damping on the mechanical losses in the generator prototype is marginal.

Both the quality factor of slide-film and drag-force damping are scaled by p^2 if all generator dimensions are scaled by p. Thus, slide-film and drag force damping become more dominant with decreasing generator size.

6.4. Electromagnetic Properties

6.4.1. Magnetic flux versus Translator Position

The flux $\phi(z)$ through the coil as a function of the translator position z is determined by the following procedure:

1. The generator is driven by sinusoidal shaker motion.
2. The open-circuit voltage $u_{oc}(t)$ is measured.
3. The relative mover position $z(t)$ is measured simultaneously using the vibrometer.
4. A window of a half-cycle of the translator motion (from peak to peak) is cut out from the data.
5. $u_{oc}(t)$ and $z(t)$ are high-pass filtered to remove DC offset.
6. $u_{oc}(t)$ is integrated to obtain $\phi(t)$. Now, a set of points corresponding to $\phi(z)$ is available, however the data contains an offset in z because the translator quiescent position is not exactly centered relative to the coil. This is due to imprecise mounting.
7. The offset z_0 can be found as follows: Since the generator has an odd flux symmetry, the maximum flux gradient should occur at $z = 0$. Thus, the position offset z_0 can be determined by finding the maximum of the flux gradient $\phi_z(z)$.

The resulting flux curves $\phi(z)$ from this procedure are shown in Fig. 6.9. The corresponding curves for the force current ratio and the

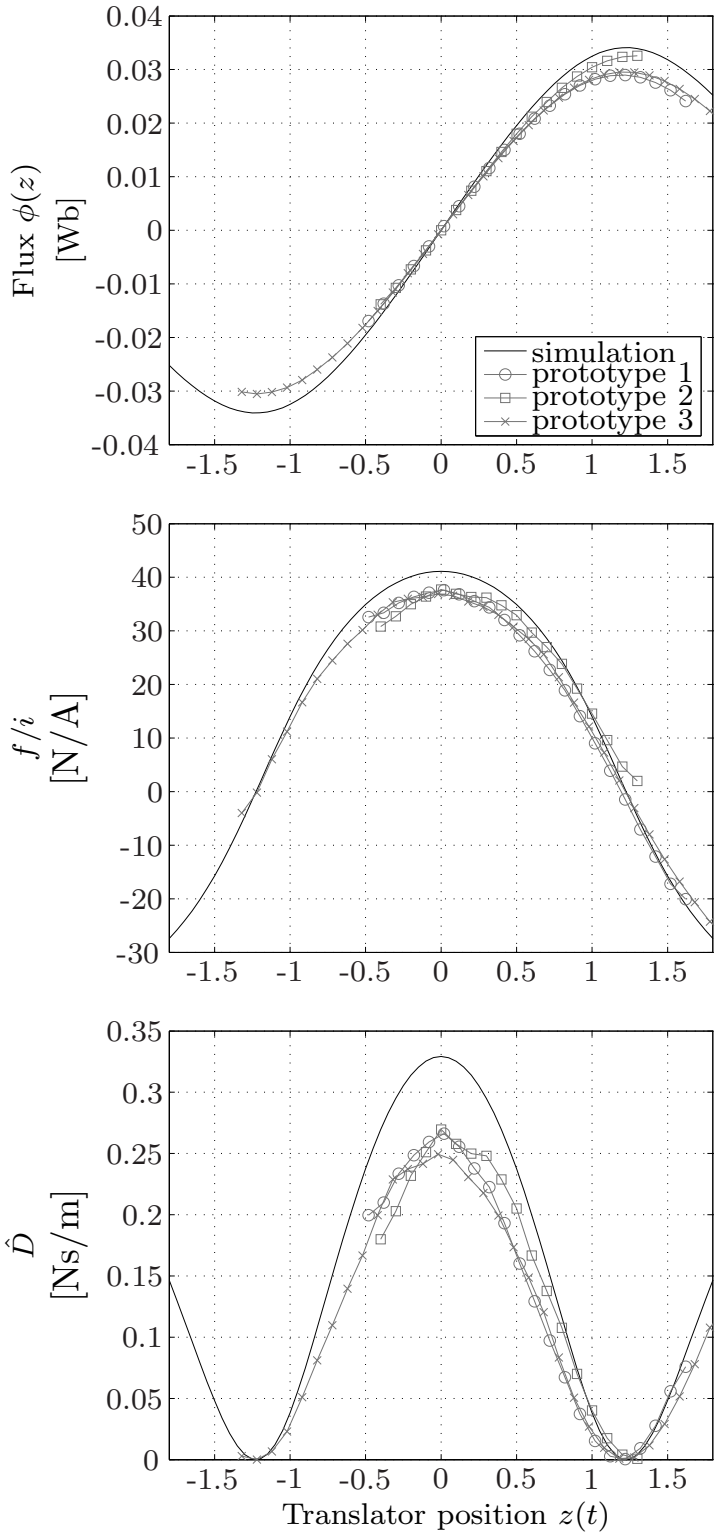

Figure 6.9: *Comparison of simulated and measured flux $\phi(z)$ (top), force current ratio f/i (middle), and force capability $\hat{D}(z)$ (bottom).*

force capability are also shown. The force current ratio and the force capability are computed as follows:

$$\frac{f}{i}(z) = \phi_z(z) \tag{6.12}$$

$$\hat{D}(z) = \frac{\phi_z^2}{R_c} \tag{6.13}$$

where R_c is the coil resistance.

As can be seen, only part of the possible translator displacement range is used by the prototypes. This is again due to the off-center quiescent position of the translator.

The measured flux curves $\phi(z)$ and the force current ratio f/i deviate maximally 12% from the predicted value. The force capability $\hat{D}$, however, deviates maximally about 23% since it is dependent on the square of the flux gradient. The deviation of the measured to the simulated value of $\hat{D}(z)$ is attributed to the following influences:

- *Remanent magnet flux density:* The flux $\phi(z)$ is approximately proportional to the remanent flux density B_r of the magnet. Thus, a deviation between the nominal B_r and the true B_r leads to a proportional error in $\phi(z)$.

  Measurements on five magnets from the same batch as used in the prototype have been carried out in order to determine the actual remanence of the used magnets. The measurement procedure consists of measuring the axial magnetic flux density $B_{z,a}$ at several equidistant points on the magnet's magnetization axis[1]. Subsequently, B_r is determined by fitting a curve to

  $$B_{z,a}(z_a) = \frac{B_r}{2}\left[\frac{h_m + z_a}{\sqrt{R_m^2 + (h_m + z_a)^2}} - \frac{z_a}{R_m^2 + z_a^2}\right] \tag{6.14}$$

  where z_a is the axial distance from the magnet's surface. An exemplary curve fit is shown in Fig. 6.10. The mean B_r computed this way is 1.217 T (standard deviation is 0.018 T), which is 14.3% lower than expected.

- *Geometric deviations:* Deviations of the geometric parameters of the translator and stator have an influence on the electromagnetic performance.

[1]The used instrumentation is the digital teslameter DTM 151 and the high-sensitivity Hall probe MPT-231 from Group 3 Technology Ltd [59]. The Hall probe has an active area of 0.5 mm · 1.0 mm.

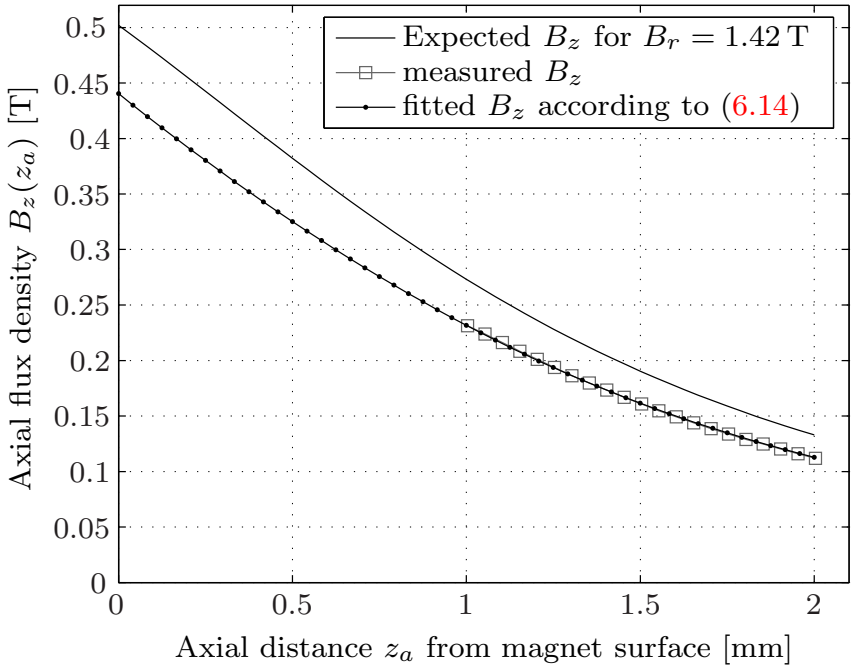

Figure 6.10: *Expected, measured and fitted curve of axial flux density of a single magnet.*

Taking into account the above error sources, the error of the predicted values is acceptable and hence the FE model used to compute $\hat{D}(z)$ is deemed to be valid.

6.4.2. Electrical Damping

In addition to the determination of $\hat{D}(z)$ in Subsec. 6.4.1, the electrical damping properties of the generator can also be determined by analyzing the decay rate of a free oscillation. For this purpose, an electrical load R_l is connected to the generator. When the translator is slightly tapped the damping of the resulting oscillation is due to both mechanical and electrical damping. By accounting for the mechanical damping as determined in Sec. 6.3, the electrical damping can then be determined.

In the carried out measurements the load resistance R_l was set to $20\,\mathrm{k}\Omega$ which is about four times the coil resistance R_c. For comparison, the decaying translator motion has also been simulated. In addition, the same measurement and simulation have been carried out for open-circuit operation of the generator. Fig. 6.11 shows the normalized translator position $z'(t)$ for simulations and measurements of

open-circuit and loaded operation for specimen No. 3. The actual initial value of $z(t)$ is in the order of 0.15 mm. For this displacement range, $\hat{D}(z)$ is approximately constant.

The mechanical damping and the resonance frequency used in the simulations is the value determined experimentally in Sec. 6.3. As in Subsec. 6.4.1, the electrical damping is overestimated by the simulation.

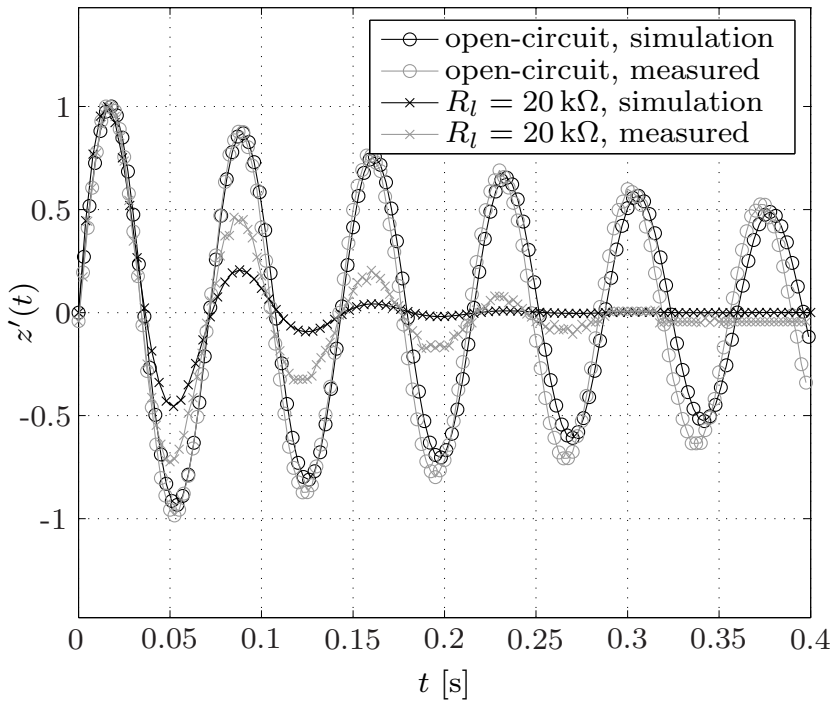

Figure 6.11: *Comparison of damping when generator is operated open-circuit or with a* 20 kΩ *load. Displacements are normalized to allow easier comparison.*

Using the same procedure as Sec. 6.3, the combined electrical and mechanical damping δ_{tot} is computed. The electrical damping δ_{el} is then obtained by subtracting the mechanical damping δ_m. Based on δ_{el} an equivalent electrical damping constant D_{el} can be computed. D_{el} is similar to $D(z)$ defined in (2.17). The difference is that D_{el} is constant and hence not dependent on z. However, for the small displacements used in the experiment (< 0.15 mm), $D(z)$ is approximately constant and approximately equal to D_{el}. From D_{el} an equivalent force capability $\hat{D}_{el}$ analogous to $\hat{D}(z)$ (cf. (2.21)) is determined by:

$$\hat{D}_{el} = D_{el}\big(1 + \alpha\big) \tag{6.15}$$

α is the ratio of load resistance to coil resistance.

The results of the above procedure are listed in Tab. 6.5. The values of $\hat{D}(z_0)$ are given by Fig. 6.9. z_0 is the offset of the translator quiescent position.

Table 6.5: *Electrical damping (measured).*

Specimen No.	D_{tot} $[\frac{\text{Ns}}{\text{m}}]$	D_m $[\frac{\text{Ns}}{\text{m}}]$	D_{el} $[\frac{\text{Ns}}{\text{m}}]$	α	$\hat{D}_{el}$ $[\frac{\text{Ns}}{\text{m}}]$	z_0 [mm]	$\hat{D}(z_0)$ $[\frac{\text{Ns}}{\text{m}}]$
1	0.0433	0.0045	0.0388	3.77	0.185	0.5	0.17
2	0.0546	0.0047	0.0499	3.79	0.239	0.5	0.21
3	0.0380	0.0060	0.0320	3.67	0.149	0.3	0.21

When inspecting Tab. 6.5 and Fig. 6.9 it can be seen that the equivalent force capabilities, $\hat{D}_{el}$, obtained by the decaying oscillation measurement and the ones obtained from the integration of the generator voltage, $\hat{D}(z_0)$, are significantly different. This difference can be partly attributed to errors in the determination of the quiescent position z_0.

6.5. Generator Efficiency

6.5.1. Efficiency versus Maximum Output Power

It is important to note that high generator efficiency and maximum electrical output power are different objectives. The operating conditions that provide maximum efficiency will generally not be the ones that yield maximum output power.

For a given generator (specified by $\hat{D}_{el}$, k, m, and Z_l) the value of α for maximum generated power is dependent on the driving motion $y(t)$ and can therefore not be given in closed form. In Subsec. 5.5.5, the optimal α has been determined numerically for a given driving motion and a given generator.

6.5.2. Computation of Generator Efficiency

While the value of α for maximum output power has to be determined numerically, the value of α for maximum generator efficiency can be given in closed form, assuming that electrical and mechanical damping can be modeled by the damping constants D_{el} and D_m, respectively.

The mean mechanical power flowing into the generator must be equal to the sum of electrical output power and all losses. The losses include

- *electrical losses:* Electrical losses are mainly due to resistive losses in the coil and are thus dependent on the coil resistance R_c. Eddy current losses are negligible.
- *mechanical losses:* Mechanical losses occur in the generator bearing due to internal friction. The losses are modeled by the mechanical damping constant D_m.
- *magnetic losses:* Magnetic losses, mainly due to magnetic hysteresis, occur only when a varying magnetic field is applied to a magnetic material. The generator presented in this thesis has no soft-magnetic material in the stator and thus magnetic losses are negligible.

The mechanical efficiency η_m and the electrical efficiency η_{el} can be approximated by:

$$\eta_m = \frac{D_{el}}{D_{el} + D_m} \tag{6.16}$$

$$\eta_{el} = \frac{R_l}{R_l + R_c} \tag{6.17}$$

where D_{el} and D_m are the damping constants due to electrical and mechanical damping, respectively. The overall efficiency is:

$$\eta = \eta_m \cdot \eta_{el} = \frac{D_{el}}{D_{el} + D_m} \cdot \frac{R_l}{R_l + R_c} \tag{6.18}$$

Using (6.15) and $\alpha = R_l/R_c$, the efficiency becomes:

$$\eta = \frac{\frac{\hat{D}_{el}}{1+\alpha}}{\frac{\hat{D}_{el}}{1+\alpha} + D_m} \cdot \frac{\alpha}{1+\alpha} \tag{6.19}$$

$$\eta = \frac{\hat{D}_{el}}{\hat{D}_{el} + D_m(1+\alpha)} \cdot \frac{\alpha}{1+\alpha} \tag{6.20}$$

With the definition of the ratio q_D

$$q_D = \frac{\hat{D}_{el}}{D_m} \tag{6.21}$$

we get:

$$\eta = \frac{q_D}{q_D + 1 + \alpha} \cdot \frac{\alpha}{1 + \alpha} \tag{6.22}$$

By deriving this equation with respect to α and setting the derivative to zero, the optimum is obtained:

$$\alpha_{opt} = \sqrt{1 + q_D} \tag{6.23}$$

The efficiency curves for the three prototypes as a function of α are shown in Fig. 6.12. The used values for $\hat{D}_{el}$ and D_m are taken from Tab. 6.5. The overall maximum efficiency for the generators is between

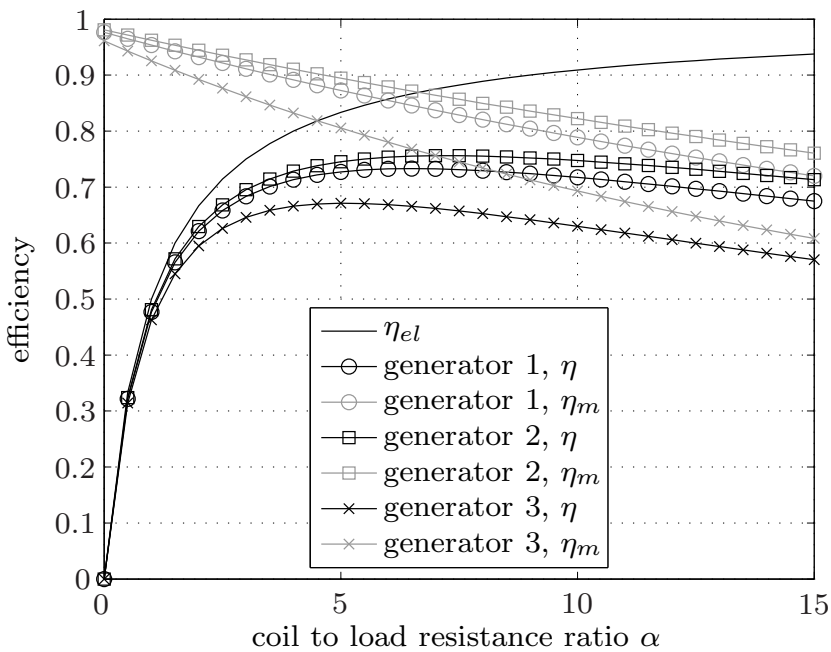

Figure 6.12: *Efficiency as a function of load to coil resistance α for the tested generator prototypes. The curves are based on (6.20) and the experimentally determined values for D_m and $\hat{D}_{el}$ listed in Tab. 6.5.*

65% and 75%. The optimal values for α are in the range of $[5, 7.5]$. It can be seen, that the chosen α for the measurements of about 3.8 (cf. Tab. 6.5) is not far from the optimal efficiency point. Note, that prototype 2 has the highest efficiency, while prototype 3 has the lowest. When comparing this with Tab. 6.5, one can see that in this case higher values of $\hat{D}_{el}$ correspond to higher efficiency values. This agrees with the statements made in Subsec. 5.3.3.

Fig. 6.13 shows the efficiency as a function of α for various q_D according to (6.22). Note that in contrast to Fig. 6.12, the curves in

Fig. 6.13 are not based on measurements. As expected, the higher the ratio q_D of equivalent force capability of the generator to mechanical damping, the higher are the achievable generator efficiencies.

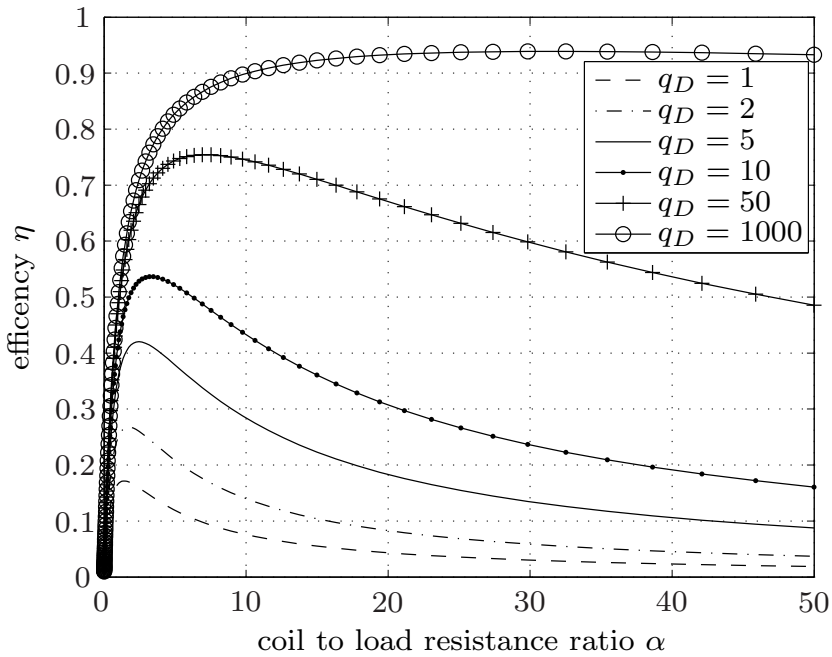

Figure 6.13: *Efficiency as a function of load to coil resistance α for various ratios q_D of electrical force capability to mechanical damping.*

6.6. Validation of System Model

The lumped system model of the generator (cf. Sec. 5.5) has been validated by comparing the measured load voltage $u_{R_l}(t)$ and the measured translator position $z(t)$ with simulation results for a given sinusoidal driving motion. The amplitude of the driving motion for the simulation model is determined by measuring the absolute motion of the generator housing with the laser vibrometer and then fitting a sinusoid to the measured motion. The used system model accounts for the offset of the quiescent translator position. In order to show the influence of the parasitic mechanical damping, the simulation has been executed with and without the mechanical damping D_m considered. The resulting translator motion $z(t)$ and the voltage across the load $u_{R_l}(t)$ are shown in Fig. 6.14.

Fig. 6.14 shows that simulated and measured waveforms have the same general shapes. In particular, the voltage waveform $u_{R_l}(t)$ has the

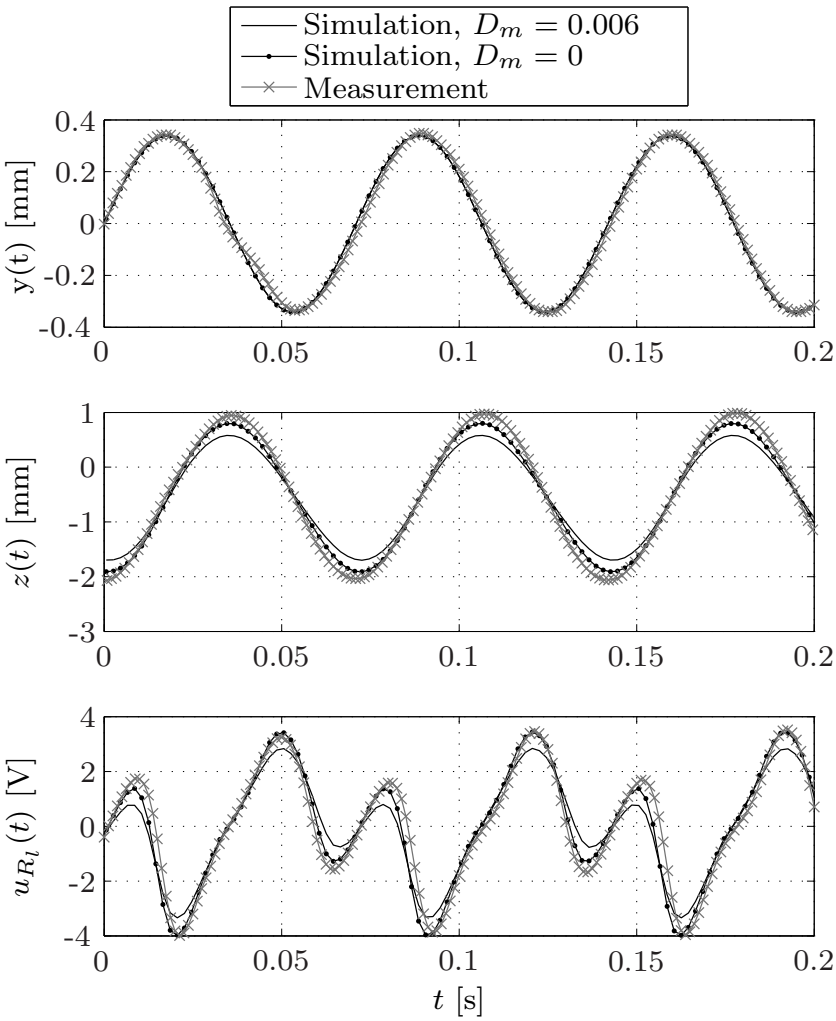

Figure 6.14: *Comparison of generator simulation and measurements for sinusoidal driving motion. Top: driving motion y, middle: translator displacement z, bottom: load voltage u_{R_l}. A load of $R_l = 20\,\mathrm{k}\Omega$ is used. Used specimen: generator No. 3.*

same asymmetry relative to the x-axis. This asymmetry is due to the off-center quiescent translator position.

It can be seen that the simulated translator position $z(t)$ has smaller amplitudes than the measured one. As previously stated in Subsec. 6.4.1, this is due to the FE model overestimating the $\hat{D}(z)$. Taking this into account, the simulated and the measured waveforms match well and thus, the lumped parameters system model is considered to be valid.

6.7. Generator Output Power from Body-Mounted Operation

In order to evaluate the generator system under realistic operating conditions, the generator has been mounted on a person. The person has then been walking around at normal walking speed in an office space environment. The voltage $u_{R_l}(t)$ has simultaneously been measured.

The generator has been mounted on the upper arm and below the knee (location 3 and 8, respectively, in Fig. 5.10). The oscillation axis of the translator has been oriented horizontally forward and horizontally to the right, respectively, for the two mounting locations. A load resistance of 10 kΩ has been used in the experiment.

Exemplary results of the measurements are shown in Fig. 6.15. The mean output power is about 5.1 μW for location 3, and 22.0 μW for location 8.

These power values are in the same range as the power values predicted in Chapter 5. Note, however, that the volume V_{conv} of the prototypes is twice as large as the volume of the designs analyzed in Chapter 5. On the other hand, the geometric parameters of the prototypes and the used load resistance are not optimized.

6.8. Comparison with State of the Art

In order to compare the performance of the generator built in this thesis with existing generators the ratio of output power for a given translator motion to stator and translator volume is used as figure of merit. The translator motion is defined by

$$z(t) = Z_0 \sin(2\pi f_d t) \tag{6.24}$$

where Z_0 is the amplitude and f_d is the frequency of the sinusoidal translator motion.

Maximum output power $\overline{P_{out}}$ is then obtained by setting the load resistance R_l equal to the coil resistance R_c. The output power is then

$$\overline{P_{out}} = \overline{u_{ind}^2} \cdot \frac{1}{4R_c^2} \tag{6.25}$$

Tab. 6.6 shows the results for the two reported inertial electromagnetic generators for which sufficient data is available for comparison. The power density for the generator of this thesis has been obtained

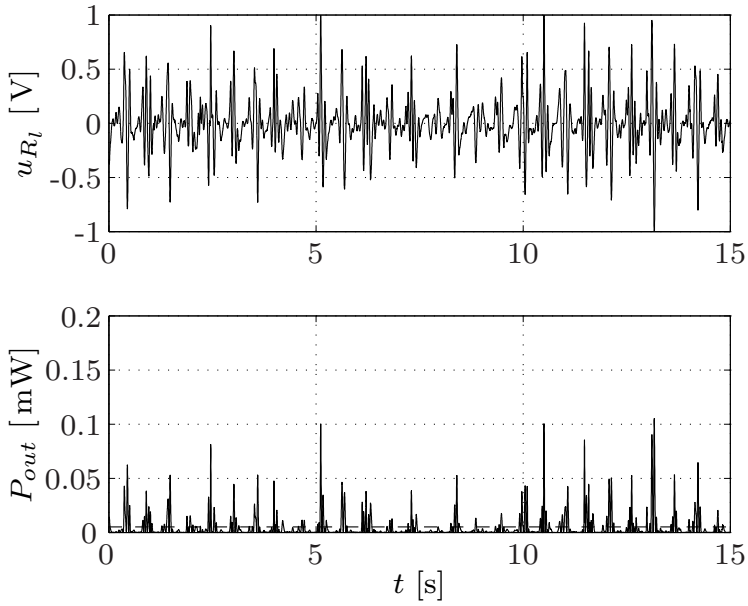

(a) Location 3, mean power 5.1 μW

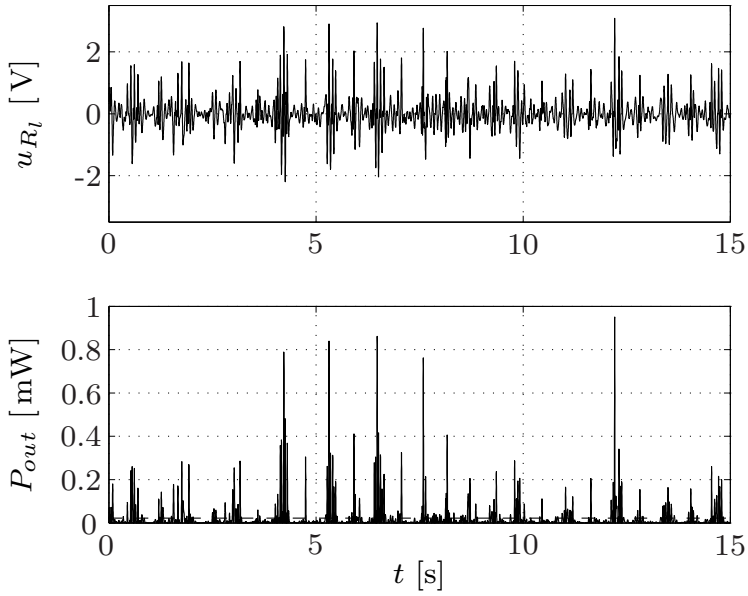

(b) Location 8, mean power 22.0 μW

Figure 6.15: *Example voltage $u_{R_l}(t)$ and power across load resistance during walking. The location numbers correspond to the mounting positions of Fig. 5.10.*

by computing the output power for $R_l = R_c$ and the same translator motion as used in the corresponding related work. It can be seen, that the generator reported in this thesis has a power density which more than 500 times larger than the one reported by Glynne-Jones et al.

Table 6.6: *Comparison with state of the art.*

Related work						Generator of this thesis		
ref.	Z_0 [mm]	f_d [Hz]	$\overline{P_{out}}$ [mW]	V_{conv} [cm^3]	$\frac{\overline{P_{out}}}{V_{conv}}$ [$\frac{\text{mW}}{\text{cm}^3}$]	$\overline{P_{out}}$ [mW]	V_{conv} [cm^3]	$\frac{\overline{P_{out}}}{V_{conv}}$ [$\frac{\text{mW}}{\text{cm}^3}$]
[28]	0.1	110	0.830	1.0	0.830	0.116	0.49	0.237
[58]	0.36	322	0.037	0.84	0.044	12.461	0.49	25.43

The generator from Ching et al. [28] has about four times the power density of the generator built in this thesis. It has to be noted, however, that the comparison is unfair, as Ching's generator makes use of a rotary motion of the magnet but [28] only reports the linear displacement amplitude of the magnet motion.

6.9. Conclusions

Three specimens of a generator prototype based on the proposed architecture of Chapter 5 have been successfully designed and fabricated. The combined volume of stator and translator is 0.49 cm^3. The complete structure weighs about 43 g, however the combined mass of coils, coils fixation, bearing, and translator is only 3.68 g.

Measurements have been carried out to validate the predicted parameter values of the generator. The following observations and conclusions are made:

- The natural frequency is overestimated by up to 70% in the simulations (cf. Tab. 6.3). This is partially due to the effect of surface roughness which is neglected by the simulations.
- The natural frequency between the generator specimens varies by ±12% (cf. Tab. 6.3), suggesting that it is difficult to control the resonance frequency precisely with the used fabrication method.
- The FE model (cf. Subsec. 5.4.2), used to compute $\hat{D}(z)$, has been validated. The measured force capability $\hat{D}(z)$ is up to 23% smaller than the predicted values (cf. Fig. 6.9). This error is attributed to deviations in the remanent flux density of the magnets and geometric parameters of stator and translator from their nominal values.

- The lumped-parameter system model (cf. Subsec. 5.5.2), used to compute the generator output power, is valid.
- The overall efficiency of the fabricated prototypes is between 65% and 75% (cf. Fig. 6.12).
- The fabricated generators are able to generate a voltage of up to 4 V under load (cf. Fig. 6.14).

7

Conclusions

7.1. Summary and Achievements

Body-worn sensor networks (BSN) could have a major impact on how health care is conducted in the future. By continously monitoring the life signs of patients and analyzing the signal patterns, dangerous medical conditions could be detected earlier which would lead to more effective treatment and shorter hospital stays. In addition, long-term life-sign data could improve the quality of diagnoses when a person becomes ill. Many other applications of on-body sensor have been explored by research groups.

One of the big obstacles on the way towards this vision is the power supply of the sensor nodes. Finite energy sources such as batteries require user maintenance and are not practical for BSN, especially if many sensor nodes are used. A possible solution to the power supply issue is *energy harvesting*. In this approach, energy in the surroundings of the sensor nodes is collected and used to supply the sensor node with power. Available energy sources include thermal energy (body heat), mechanical energy (body motion) or radiation energy (sun light).

This thesis has explored the suitability of inertial electromagnetic micro-generators to harvest mechanical energy from human body mo-

tion. Compared to existing work on electromagnetic micro-generators for energy harvesting, the main contributions of the thesis are special consideration of the operating conditions of body-worn generators, a novel generator architecture, and the proposal of a suitable optimization method. The following contributions have been made:

- A large set of 3D on-body acceleration data from human walking has been gathered using a custom-made sensor system. The measurements include 9 points on the human body and 8 test subjects. The evaluation of the data has shown that on-body acceleration consists of many spectral frequencies up to 30 Hz and can thus not be modeled by sinusoidal waveforms. This observation has a significant influence when generator output power is estimated.

- Based on the recorded acceleration waveforms and generic generator models, the performance of three types of body-worn inertial generators has been analyzed independent of implementation technology. The analyzed types are velocity-damped resonant generators (VDRG), Coulomb-damped resonant generators (CDRG), and Coulomb-force parametric generator (CFPG). Velocity-damped generators can be implemented using piezoelectric or electromagnetic conversion principles, Coulomb-damped generators correspond to electrostatic implementations. The following has been shown:

  - In optimal operation, inertial generators operate at the displacement limit, i.e. the proof-mass makes full use of the available displacement limit Z_l.
  - For $Z_l < 1\,\mathrm{mm}$, generator output power is approximately proportional to both the mass m and the displacement limit Z_l of the proof-mass. However, for $Z_l > 1\,\mathrm{mm}$, the output power increases less rapidly than Z_l.
  - Which generator has the largest output power depends on Z_l. VDRG has highest performance for large values of Z_l and the CFPG for small values of Z_l. The cross-over point is at approximately $200\,\mu\mathrm{m}$ for generators mounted on the upper body and at $800\,\mu\mathrm{m}$ for generators mounted on the lower body.
  - For $Z_l < 1\,\mathrm{mm}$, the optimal spring constant of the resonant generators is approximately proportional to $1/Z_l$.

  - Inertial generators mounted on the lower body generate about 4 times as much power as generators mounted on the upper body.

- An architecture for an electromagnetic inertial micro-generator has been proposed. The architecture is based on the combination of a tubular air-cored generator topology and a flexible bearing based on a parallel spring stage.

- A two-stage optimization method for inertial electromagnetic generators has been developed and applied to the selected architecture. The first stage optimizes the geometry of generator to maximize the electromagnetic force capability of the generator. The second stage optimizes resonance frequency and load resistance to generate maximum output power from a given driving motion. The following has been shown:

  - The optimal ratios of magnet radius to total translator radius, q_r, and magnet height to pole height, q_h, vary little with generator volume. The optimal q_r is about 0.7 to 0.8, the optimal ratio of magnet height to pole height is about 0.8 to 0.9.
  - The length of stator and translator are similar in optimal designs.
  - The generator force capability and the output power increase approximately linearly with volume.
  - As in the comparison of VDRG, CDRG, and CFPG, the generated power is about 4 times higher for generators mounted on the upper body compared to the lower body.
  - The optimal resonant frequencies of the generator are not at the fundamental frequency of the body motion, as frequently assumed by previous work. Instead, they are between 5 and 20 Hz, depending on the driving motion and the displacement limit Z_l of the translator.

- Three specimen of a generator prototype have successfully been designed and fabricated.

  - The combined volume of stator and translator is $0.49\,\mathrm{cm}^3$. The complete structure weighs about 43 g, however the combined mass of coils, coils fixation, bearing, and translator is only 3.68 g.

- The generators have an overall efficiency of 65% to 75% and generate between 5 and 25 μW from normal human walking. These power levels are sufficient for many sensing applications.
- The voltage levels across the load reach 0.5 to 4 V, which allows further electronic power processing.
- Maximum generator efficiency is achieved by setting the ratio of load resistance to coil resistance to an optimal value. This optimal value depends on the ratio of electrical damping to mechanical damping.
- Measurements carried out on the generators have confirmed the simulation models used in this thesis.

In conclusion, this thesis shows that electromagnetic inertial generators are a viable option for the power supply of body-worn sensors networks. However, a volume of 0.125 to 0.5 cm^3 is required for the volume of translator and stator for acceptable power levels.

7.2. Outlook

The presented inertial electromagnetic micro-generator design could be used as power supply in future body-worn sensor networks. However, further research is necessary towards the realization of this vision. Possible starting points are discussed in the following paragraphs.

- The presented generator has been connected to a resistive load in the simulation as well as in the measurements. The generated voltage has alternating polarity. However, in a real application scenario, a DC voltage source is needed. In addition, the sensor node powered by the generator should also be able to operate during a period when no body motion is present. Thus, suitable power processing is needed to rectify the generated AC voltage as well as to provide energy storage.

  A further task of the power processing circuitry is the online adaptation of the electrical load and thus the electrical damping to the driving motion. This adaptation is necessary in order to maximize the generated power.

  Research on efficient power processing for inertial electromagnetic generators is rarely published and is specially challenging, since

the input voltage has low voltage levels and an irregular, non-sinusoidal shape.

- The flexible bearing presented in this thesis occupies a significant volume. In order to make the generator a viable option for body-worn power supplies, the bearing should be miniaturized. This could be achieved by adding additional flexible hinges to the structure which would allow to reduce the lengths of the parallel beams while having the same maximum displacement.

- The reliability of the generator has not been analyzed in this thesis. However, for the envisioned application in body-sensor networks, reliability is crucial. Possible mechanisms resulting in failure or performance reduction include fatigue fracture of the notch hinges in the bearing, break of the coil wires, and demagnetization of the magnets due to heavy vibrations.

- The generator prototypes have been fabricated using standard precision engineering methods and subsequent hand assembly. This procedure leads to excessive fabrication cost if the generator is to be used in commercial body-worn sensor networks. Thus, a suitable strategy has to be developed to allow low-cost mass-production.

Glossary

Symbols

Name	SI Unit	Meaning
A	m^2	plate area (air damping analysis)
B	T	magnetic flux density, also called magnetic induction
b	m	depth of notch hinge
D	Ns/m	ratio of damping force due to energy conversion to velocity of transducing element, also called force velocity ratio
D_m	Ns/m	damping coefficient due to mechanical losses
D_{tot}	Ns/m	total damping coefficient
$\hat{D}(z)$	Ns/m	force capability of inertial generator (force velocity ratio for short-circuit operation)
$\hat{D}_{el}$	Ns/m	equivalent force capability (constant approximation of $\hat{D}(z)$)
d	m	distance between two moving surfaces (air damping analysis)
d_w	m	diameter of coil wire with insulation
d_{wi}	m	diameter of coil wire without insulation
e	m	thickness of notch hinge
E	N/m^2	elastic modulus
E	V/m	electric field
f	N	electrical damping force due to energy conversion
f_d	Hz	frequency of driving motion
f_e	Hz	eigen-frequency
f_n	Hz	natural frequency or undamped resonant frequency

F_s	N	spring force
F_a	N	inertial force
g	m	air-gap length
H	A/m	magnetic field strength
h_{conv}	m	converter height (height needed to accommodate stator and translator including translator displacement)
h_m	m	height of magnet
h_p	m	pole pitch
h_s	m	height of soft-magnetic spacer
h_{tr}	m	height of translator
L_c	H	coil inductance
l	m	arm length of flexible bearing
m	kg	translator mass
m_{eff}	kg	effective translator mass of prototype, used to compute natural frequency f_n
n_c		number of coils
n_m		number of magnets
n_p		number of poles on length-limiting part of generator
Δn_p		difference in number of poles between stator and translator
n_{tot}		total number of coil windings
$\overline{P_{conv}}$	W	mean power converted from mechanical to electrical (includes power dissipated in the coil resistance)
$\overline{P_{out}}$	W	mean generator output power (power dissipated in load)
Q_m		mechanical qualitiy factor
q_D		ratio of equivalent force capability to mechanical damping ($\hat{D}_{el}/D_m$)
q_r		ratio of magnet radius to outer radius (R_m/R_o)
q_h		ratio of magnet height to pole pitch (h_m/h_p)

q_w		aspect ratio: total converter height to outer radius (h_{conv}/R_o)
R_c	Ω	coil resistance
R_l	Ω	load resistance
R_m	m	radius of magnet
r	m	radius of notch hinge
r_s	m	chamfer radius of notch hinge
t_c	m	coil thickness
$u_{R_l}(t)$	V	voltage across load resistance
V_{conv}	m^3	converter volume (volume needed to accommodate stator and translator including translator displacement)
w	m	width of notch hinge
$x(t)$	m	position of proof-mass or translator
$y(t)$	m	position of generator frame
Z_l	m	maximum translator displacement (as limited by generator housing)
Z_{lb}	m	maximum translator displacement (as limited by maximum stress of flexible bearing)
$z(t)$	m	position of proof-mass or translator relative to generator frame
α		ratio of load to coil resistance (R_l/R_c)
δ_m	rad/s	mechanical damping
η		overall generator efficiency
η_{el}		electrical efficiency
η_m		mechanical efficiency
μ	Ns/m^2	coefficient of viscosity of air
$\phi(z)$	Wb	total magnetic flux through coil as a function of translator position
ρ_{air}	kg/m^3	density of air
ρ_b	kg/m^3	density of beam material
ω_e	rad/s	angular frequency equivalent of f_e
ω_n	rad/s	angular frequency equivalent of f_n

Acronyms and Abbreviations

BSN	body sensor network
CDRG	coulomb-damped resonant generator
CFPG	coulomb-force parametric generator
EEG	**e**lectro**e**ncephalo**g**raphy, neurophysiologic measurement of the electrical activity of the brain by recording from electrodes
EHG	energy harvesting generator
FEA	finite element analysis
1 g	an acceleration of 9.81 m/s, which is approximately equal to the acceleration due to gravity on the Earth's surface
1 g	a mass of 1 gram
NdFeB	neodymium-iron-boron (permanent magnet material)
PadNET	physical activity detection network
POM	**p**oly**o**xy**m**ethylene, also known as acetal or polyacetal
PM	permanent magnet
RF	radio frequency
VDRG	velocity-damped resonant generator

Bibliography

[1] N. Almeras, N. Mimeault, O. Serresse, M. Boulay, and A. Tremblay. Non-exercise daily energy expenditure and physical activity pattern in male endurance athletes. *Eur J Appl Physiol*, 63:184–187, 1991.

[2] R. Amirtharajah and A. P. Chandrakasan. Self-powered low power signal processing. In *1997 Symposium on VLSI Circuits*, pp. 25–26, June 1997.

[3] R. Amirtharajah and A. P. Chandrakasan. Self-powered signal processing using vibration-based power generation. *IEEE Journal of Solid-State Circuits*, 33(5):687–695, May 1998.

[4] Analog Devices. ADXL202/210 iMEMS Accelerometer Datasheet, Rev. A. Available at http://www.analog.com.

[5] U. Anliker, J. Ward, P. Lukowicz, G. Tröster, F. Dolveck, M. Baer, F. Keita, B. Schenker-Eran, F. Catarsi, L. Coluccini, A. Belardinelli, D. Shklarski, M. Alon, E. Hirt, R. Schmid, and M. Vuskovic. Amon: A wearable multiparameter medical monitoring and alert system. *IEEE Transactions on Information Technology in Biomedicine*, 8(4):415–427, Dec. 2004.

[6] ANSYS Inc. ANSYS Emag. http://www.ansys.com/products/emag.asp.

[7] J. Antaki, G. Gertocci, E. Green, A. Nadeem, T. Rintoul, R. Kormos, and B. Griffith. A gait-powered autologous battery charging system for artificial organs. *ASAIO J (American Society for Artificial Internal Organs)*, 41(3):M588–M595, July 1995.

[8] K. Antonsson, E and W. Mann, R. The frequency content of gait. *Journal of Biomechanics*, 18(1):39–47, 1985.

[9] A. Arnau, ed. *Piezoelectric Transducers And Applications*. Springer, 2004, 2004. ISBN 3-540-20998-0.

[10] N. J. Baker. *Linear Generators for Direct Drive Marine Renewable Energy Converters*. PhD thesis, School of Engineering, University of Durham, UK, 2003.

[11] N. J. Baker and M. A. Mueller. Permanent magnet air-cored tubular linear generator for marine energy converters. In *Second IEE International Conference on Power Electronics, Machines and Drives, Edinburgh, UK*, vol. 2, pp. 862–867, Mar. 2004.

[12] L. Bao and S. S. Intille. Activity recognition from user-annotated acceleration data. In *Proceedings of Second International Conference on Pervasive Computing, Vienna, Austria*, pp. 1–17, Apr. 2004.

[13] M.-H. Bao. *Micro Mechanical Transducers. Pressure Sensors, Accelerometers And Gyroscopes.* Elsevier, 2000. ISBN 0-444-50558-X.

[14] P. Bauer, M. Sichitiu, R. Istepanian, and K. Premaratne. The mobile patient: Wireless distributed sensor networks for patient monitoring and care. In *Proceedings of the IEEE EMBS International Conference on Information Technology Applications in Biomedicine, Arlington, Virginia, USA*, pp. 17–21, Nov. 2000.

[15] S. P. Beeby, P. Glynne-Jones, E. P. James, M. J. Tudor, and N. M. White. Kinetic energy harvesting for wireless sensor systems. Presentation at IEE Annual Wheatstone Event, Dec. 2002.

[16] S. P. Beeby, M. J. Tudor, E. Koukharenko, N. M. White, T. O'Donnell, C. Saha, S. Kulkarni, and S. Roy. Micromachined silicon generator for harvesting power from vibrations. In *The 4th Int. Workshop on Micro and Nanotechnology for Power Generation and Energy Conversion Application (PowerMEMS 2004), Kyoto, Japan*, pp. 104–107, Nov. 2004.

[17] S. P. Beeby, M. J. Tudor, E. Koukharenko, N. M. White, T. O'Donnell, C. Saha, S. Kulkarni, and S. Roy. Design and performance of a microelectromagnetic vibration-powered generator. In *Transducers '05, Seoul, Korea, Tech. Digest*, vol. 1, pp. 780–783, June 2005.

[18] S. P. Beeby, M. J. Tudor, E. Koukharenko, N. M. White, T. O'Donnell, C. Saha, S. Kulkarni, and S. Roy. Design, fabrication and simulations of microelectromagnetic vibration powered generator for low power MEMS. In *Symposium on Design Testing Integration and Packaging of MEMS/MOEMS (DTIP '05), Montreux, Switzerland*, pp. 374–379, June 2005.

[19] J. Boland, Y.-H. Chao, Y. Suzuki, and Y. C. Tai. Micro electret power generator. In *Proceedings of the IEEE International Conference on Micro Electro Mechanical Systems (MEMS)*, pp. 538–541, 2003.

[20] A. Bolz, V. Lang, B. Merkely, and M. Schaldach. First results of an implantable sensor for blood flow measurement. *Annual International Conference of the IEEE Engineering in Medicine and Biology Proceedings*, 1997.

[21] H. Böttner. Thermoelectric micro devices: Current state, recent developments and future aspects for technological progress and applications. In *International Conference on Thermoelectrics, Long Beach, California, USA*, 2002.

[22] H. Brashear, T. Starner, P. Lukowicz, and H. Junker. Using multiple sensors for mobile sign language recognition. In *Proceedings of the 7th International Symposium on Wearable Computers*, pp. 45–52, 2003.

[23] L. Bratteby, B. Sandhagen, M. Lotborn, and G. Samuelson. Daily energy expenditure and physical activity assessed by an activity diary in 374 randomly selected 15-year-old adolesscents. *Eur J Clin Nutr*, 51(9):592–600, 1997.

[24] A. Buzhinskii, V. Use of the snap-through membrane effect to limit dynamic loads. *Mechanics of Solids*, 24(4):40–45, 1989.

[25] B. Cavallier, K. Dogheche, P. Delobelle, L. Hirsinger, E. Cattan, D. Remiens, M. Marzencki, B. Charlot, S. Basrour, and S. Ballandras. Piezoelectric micro-machined ultrasonic transducer (pMUT) for energy harvesting. In *IEEE International Ultrasonics Symposium (UFFC '05)*, Sept. 2005.

[26] N. N. H. Ching, G. M. H. Chan, W. J. Li, H. Y. Wong, and P. H. W. Leong. PCB-integrated micro-generator for wireless systems. In *Proceedings of the International Symposium on Smart Structures and Microsystemms, Hong Kong*, Oct. 2000.

[27] N. N. H. Ching, H. Y. Wong, W. J. Li, and P. H. W. Leong. A laser-micromachined vibrational to electrical power transducer for wireless sensing systems. In *Proceedings of Transducers'01 / Eurosensors XV*, June 2001.

[28] N. N. H. Ching, H. Y. Wong, W. J. Li, P. H. W. Leong, and Z. Wen. A laser-micromachined multi-modal resonating power transducer for wireless sensing systems. *Sensors and Actuators, A: Physical*, 97:685–690, Apr. 2002.

[29] D. L. Churchill, M. J. Hamel, C. P. Townsend, and S. W. Arms. Strain energy harvesting for wireless sensor networks. *Smart Structures and Materials 2003: Smart Electronics, MEMS, BioMEMS, and Nanotechnology, Proceedings of SPIE*, 5055(1): 319–327, 2003.

[30] Citizen Watch Ltd. Eco-drive and eco-drive thermo watches. http://www.citizenwatch.com.

[31] J. Coey, ed. *Rare-Earth Iron Permanent Magnets*. Oxford Science Publications, 1996. ISBN 0 19 8517920.

[32] P. J. Cornwell, J. Goethal, J. Kowko, and M. Damianakis. Enhancing power harvesting using a tuned auxiliary structure. *Journal of Intelligent Material Systems and Structures*, 16(10):825–834, 2005.

[33] G. Despesse, J. J. Chaillout, T. Jager, J. M. Léger, A. Vassilev, S. Basrour, and B. Charlot. High damping electrostatic system for vibration energy scavenging. In *Proceedings of the 2005 joint conference on Smart objects and ambient intelligence*, pp. 283–286, New York, NY, USA, May 2005. ACM Press.

[34] G. Despesse and T. Jager. Exploitation of the thermotunnel effect for energy scavenging. *Journal of Applied Physics*, 96(9), Nov. 2004.

[35] G. Despesse, T. Jager, S. Basrour, J. J. Chaillout, J. M. Léger, B. Charlot, and A. Vassilev. Fabrication and characterization of high damping electrostatic micro devices for vibration energy scavenging. In *Symposium on Design, Test, Integration and Packaging of MEMS/MOEMS (DTIP 2005), Montreux, Switzerland*, June 2005.

[36] G. Dewar. Static and dynamic magnetoelasticity. In *Proceedings of SPIE The International Society for Optical Engineering*, 2001.

[37] A. Dhawan, K. Ghosh-Tushar, M. Seyam-Abdelfattah, and J. Muth. Development of woven fabric-based electrical circuits. In *Materials Research Society Symposium Proceedings*, 2002.

[38] K. Dogheche, B. Cavallier, P. Delobelle, L. Hirsinger, E. Cattan, D. REmiens, B. Charlot, S. Basrour, and S. Ballandras. A bi-stable micro-machined piezoelectric transducer for mechanical to electrical energy transformation. In *Symposium on Design, Test, Integration and Packaging of MEMS/MOEMS (DTIP 2005), Montreux, Switzerland*, June 2005.

[39] T. Douseki, Y. Yoshida, F. Utsunomiya, N. Itoh, and N. Hama. A batteryless wireless system uses ambient heat with a reversible-power-source compatible CMOS/SOI DC-DC converter. In *IEEE International Solid-State Circuits Conference, 2003. Digest of Technical Papers*, vol. 1, Feb. 2003.

[40] M. El-hami, P. Glynne-Jones, E. P. James, S. P. Beeby, and N. M. White. Design analysis of a self-powered micro-renewable power supply. Presentation at International Conference on Electrical Machines 2000 (ICEM), Aug. 2000.

[41] M. El-hami, P. Glynne-Jones, E. P. James, S. P. Beeby, and N. M. White. Design and analysis of a self-powered micro-renewable power supply. In *Proceedings International Conference on Electrical Machines 2000 (ICEM)*, vol. 3, pp. 1466–1470, Aug. 2000.

[42] M. El-hami, P. Glynne-Jones, E. P. James, S. P. Beeby, N. M. White, A. D. Brown, and M. Hill. A new approach towards the design of a vibration-based microelectromechanical generator. In *Proceedings of Transducers'00 / Eurosensors XIV*, pp. 483–486, 2000.

[43] M. El-hami, P. Glynne-Jones, N. M. White, M. Hill, S. Beeby, E. James, A. D. Brown, and J. N. Ross. Design and fabrication of a new vibration-based electromechanical power generator. *Sensors and Actuators, A: Physical*, 92(1–3):335–342, Aug. 2001.

[44] Encyclopaedia Britannica, Inc. Encyclopaedia britannica online. http://search.eb.com/.

[45] EnOcean GmbH. Batteryless piezo radio transmitter modules. http://www.enocean.com/.

[46] M. Ericka, D. Vasic, F. Costa, G. Poulin, and S. Tliba. Energy harvesting from vibration using a piezoelectric membrane. *Journal De Physique*, 2005.

[47] K. Finkenzeller. *RFID Handbook (Second Edition)*. John Wiley & Sons, Ltd., 2003.

[48] FitSense Inc. Pacer activity monitor device. http://www.fitsense.com/b/Pacer.asp.

[49] A. Flowerday and R. Smith. Lessons learnt from long-term chronic condition monitoring. In *International Workshop on Wearable and Implantable Body Sensor Networks Proceedings, Imperial College, London, U.K.*, Apr. 2004.

[50] ForeverFlashlights. Batteryless flashlights. http://www.foreverflashlights.com/.

[51] Freeplay Energy Plc. Windup radios. http://windupradio.com/windup.htm.

[52] L. Gamlyn, P. Needham, S. M. Sopher, and T. J. Harris. The development of a neural network-based ambulatory ECG monitor. *Neural Computing and Applications*, 41(4):273–278, Apr. 1999.

[53] K. Ghandi. Compact piezoelectric based power generation. DARPA Energhy Harvesting Programm, 2000. URL http://www.darpa.mil/dso/trans/energy/ab_ccc.html.

[54] H. Glosch, M. Ashauer, U. Pfeiffer, and W. Lang. Thermoelectric converter for energy supply. *Sensors and Actuators, A: Physical*, 74(1):246–250, Apr. 1999.

[55] P. Glynne-Jones, S. P. Beeby, E. P. James, and N. M. White. The modelling of a piezoelectric vibration powered generator for microsystems. In *Proceedings of Transducers'01 / Eurosensors XV*, vol. 1, pp. 46–49, June 2001.

[56] P. Glynne-Jones, S. P. Beeby, and N. M. White. Towards a piezoelectric vibration-powered microgenerator. *IEE Proceedings Sciene, Measurement and Technology*, 148(2):68–72, Mar. 2001.

[57] P. Glynne-Jones, M. El-hami, S. P. Beeby, E. P. James, A. D. Brown, M. Hill, and N. M. White. A vibration-powered generator

for wireless microsystems. In *International Symposium on Smart Structures and Microsystems (IS3M)*, Oct. 2000.

[58] P. Glynne-Jones, M. J. Tudor, S. P. Beeby, and N. M. White. An electromagnetic, vibration-powered generator for intelligent sensor systems. *Sensors and Actuators, A: Physical*, 110(1-3): 344–349, Feb. 2004.

[59] Group3 Technology Ltd. Digital teslameter DTM151 and hall probe MPT-231. http://group3technology.com.

[60] D. Guyomar, A. Badel, E. Lefeuvre, and C. Richard. Toward energy harvesting using active materials and conversion improvement by nonlinear processing. *IEEE Transactions on Ultrasonics, Ferroelectrics, and Frequency Control*, Apr. 2005.

[61] J. P. D. Hartog. Forced vibrations with combined coulomb and viscous friction. *Journal of Applied Mechanics (Transactions of ASME)*, 53:107–115, Dec. 1931.

[62] S. Henein. *Conception des Structures Articulées à Guidages Flexibles de Haute Précision*. PhD thesis, École Polytechnique Fédéral de Lausanne, 2000.

[63] S. Henein. *Conception des Guidages Flexibles*. Presses Polytechniques et Universitaire Romandes, 2004. ISBN 2-8807-481-4.

[64] S. Henein, S. Bottinelli, and R. Clavel. Parallel spring stages with flexures of micrometric cross-sections. *Proceedings of the SPIE The International Society for Optical Engineering*, 3202: 209–220, 1998.

[65] C. Hierold, B. Clasbrumme, D. Behrend, T. Scheiter, M. Steger, K. Oppermann, H. Kapels, E. Landgraf, D. Wenzel, and D. Etuodt. Implantable low power integrated pressure sensor system for minimal invasive telemetric patient monitoring. In *The Eleventh Annual International Workshop on Micro Electro Mechanical Systems, 1998. MEMS 98. Proceedings*, pp. 568–573, 1998.

[66] A. S. Holmes, G. Hong, and K. R. Pullen. Axial-flux permanent magnet machines for micropower generation. *Microelectromechanical Systems, Journal of*, 14:54–62, 2005.

[67] W.-S. Huang, K.-E. Tzeng, M.-C. Cheng, and R.-S. Huang. Design and fabrication of a vibrational micro-generator for wearable MEMS. In *Eurosensors XVII, The 17th European Conference on Solid-State Transducers, University of Minho Guimaraes, Portugal*, pp. 695–697, Sept. 2003.

[68] B. L. Ibey, V. K. Yadavalli, H. R. Thomas, R. M. Rounds, M. V. Pishko, and G. L. Coté. Implantable fluorescence-based glucose sensor development. In *Progress in Biomedical Optics and Imaging Proceedings of SPIE*, vol. 5702, pp. 1–6, 2005.

[69] M. Ichiki, K. Ashida, T. Kitahara, and M. Tanaka. Piezoelectric transducer properties and its application to the micro power generator. *Ferroelectrics*, 273:237–242, 2002.

[70] T. Ikeda. *Fundamentals of Piezoelectricity.* Oxford University Press, New York, 1990.

[71] L. Ingber. Simulated annealing: Practice versus theory. *Mathematical and Computer Modelling*, 18:29–57, Dec. 1993.

[72] E. P. James, P. Glynne-Jones, M. El-hami, S. P. Beeby, J. N. Ross, and N. M. White. Planar signal extraction techniques for a self-powered microsystem. Presentation at MTEC 2001, Feb. 2001.

[73] E. P. James, P. Glynne-Jones, M., El-Hami, S. P. Beeby, J. N. Ross, and N. M. White. Planar signal extraction techniques for a self-powered microsystem. *Measurement and Control*, 34(2): 37–39, Mar. 2001.

[74] E. P. James, M. J., Tudor, S. P. Beeby, N. R. Harris, P. Glynne-Jones, J. N. Ross, and N. M. White. An investigation of self-powered systems for condition monitoring applications. *Sensors and Actuators A: Physical*, 110(1-3):171–176, Feb. 2004.

[75] E. P. James, M. J. Tudor, S. P. Beeby, N. R. Harris, P. Glynne-Jones, J. N. Ross, and N. M. White. A wireless self-powered micro-system for condition monitoring. In *Proceedings of Eurosensors XVI*, Sept. 2002.

[76] Y. B. Jeon, R. Sood, J. h. Jeong, and S. G. Kim. MEMS power generator with transverse mode thin film PZT. *Sensors and Actuators A: Physical*, 122:16–22, July 2005.

[77] E. Jovanov, A. O'Donnell Lords, D. Raskovic, P. G. Cox, R. Adhami, and F. Andrasik. Stress monitoring using a distributed wireless intelligent sensor system. *Engineering in Medicine and Biology Magazine, IEEE*, 22:49–55, 2003.

[78] S.-Y. Jung, H.-Y. Choi, H.-K. Jung, Y.-S. Choi, and K.-M. Choi. Performance evaluation of permanent magnet linear generator for charging the battery of mobile apparatus. In *IEEE International Electric Machines and Drives Conference, IEMDC*, pp. 516–521, 2001.

[79] T.-P. Jung, S. Makeig, M. Stensmo, and T. J. Sejnowski. Estimating alertness from the EEG power spectrum. *IEEE Transactions on Biomedical Engineering*, 44(1):60–69, Jan. 1997.

[80] H. Junker, P. Lukowicz, and G. Tröster. Padnet: Wearable physical activity detection network. In *Seventh International Symposium on Wearable Computers, 2003. Proceedings*, pp. 244–245, 2003.

[81] J. Y. Kang, H. J. Kim, J. S. Kim, and T. S. Kim. Optimal design of piezoelectric cantilever for a micro power generator with microbubble. In A. Dittmar and D. Beebe, ed., *2nd Annual International IEEE EMBS Special Topic Conference on Microtechnologies in Medicine and Biology*, pp. 424–427, 2002.

[82] J. J. Kiely, D. V. Morgan, D. M. Rowe, and J. M. Humphrey. Low cost miniature thermoelectric generator. *Electronics Letters*, 27 (25):2332–2334, Dec. 1991.

[83] W. Kim, A. Voploshin, S. Johnson, and A. Simkin. Measurement of the impulsive bone motion by skin-mounted accelerometers. *Journal of Biomechanical Engineering*, 115(1):47–52, Feb. 1993.

[84] Kinetron B.V., Micro Generating Systems. Homepage. http://www.kinetron.nl.

[85] M. Kishi, H. Nemoto, T. Hamao, M. Yamamoto, S. Sudou, M. Mandai, and S. Yamamoto. Micro-thermoelectric modules and their application to wristwatches as an energy source. In *International Conference on Thermoelectrics, ICT, Proceedings*, pp. 301–307, Aug. 1999.

[86] Kistler Instruments Ltd. http://www.kistler.com.

[87] M. J. Konak, I. G. Powlesland, S. P. van der Velden, and S. C. Galea. A self-powered discrete time piezo-elecric vibration damper. *Proceedings of SPIE - the International Society of Optical Engineering*, 3241:270–279, 1997.

[88] R. D. Kornbluh, R. Pelrine, Q. Pei, R. Heydt, S. Stanford, S. Oh, and J. Eckerle. Electroelastomers: Applications of dielectric elastomer transducers for actuation, generation, and smart structures. *Smart Structures and Materials 2002: Industrial and Commercial Applications of Smart Structures Technologies. San Diego, CA, United States*, 4698(1):254–270, Mar. 2002.

[89] J. Kravcak, L. Novak, and A. Zentko. The analysis of large barkhausen effect in the FeSiB amorphous wire. *Czechoslovak Journal of Physics*, 52(2):175–178, Feb. 2002.

[90] H. Kulah and K. Najafi. An electromagnetic micro power generator for low-frequency environmental vibrations. In *Proceedings of The 17th IEEE International Conference on Micro Electro Mechanical Systems, MEMS 2004, Maastricht, Netherlands*, pp. 237–240, 2004.

[91] A. D. Kuo. Harvesting energy by improving the economy of human walking. *Science*, 309:1686–1687, Sept. 2005.

[92] J. Kymissis, C. Kendall, J. Paradiso, and N. Gershenfeld. Parasitic power harvesting in shoes. In *Second International Symposium on Wearable Computers 1998*, pp. 132–139, 1998.

[93] A. Lal, R. Duggirala, and H. Li. Pervasive power: A radioisotope-powered piezoelectric generator. *Pervasive Computing, IEEE*, 4: 53–61, 2005.

[94] J. B. Lee, Z. Chen, M. G. Allen, A. Rohatgi, and R. Arya. High voltage solar cell array as an electrostatic MEMS power supply. *Proceedings of the IEEE Micro Electro Mechanical Systems*, pp. 331–336, 1994.

[95] J. M. H. Lee, S. C. L. Yuen, W. J. Li, and P. H. W. Leong. Development of an AA size energy transducer with micro resonators. In *Proceedings IEEE International Symposium on Circuits and Systems*, vol. 4, pp. IV876–IV879, 2003.

[96] E. Lefeuvre, A. Badel, A. Benayad, L. Lebrun, C. Richard, and D. Guyomar. A comparison between several approaches of piezoelectric energy harvesting. *Journal De Physique*, 2005.

[97] E. S. Leland, E. M. Lai, and P. K. Wright. A self-powered wireless sensor for indoor environmental monitoring. In *Symposium, University of Texas, Austin, USA*, Oct. 2004.

[98] G. A. Lesieutre, G. K. Ottman, and H. F. Hofmann. Damping as a result of piezoelectric energy harvesting. *Journal of Sound and Vibration*, 269:991–1001, Jan. 2004.

[99] H. Li, A. Lal, J. Blanchard, and D. Henderson. Self-reciprocating radioisotope-powered cantilever. *Journal of Applied Physics*, 92 (2):1122–1127, July 2002.

[100] W. J. Li. Wireless sensors with integrated vibration-induced power generator. International Conference on Intelligent Robots and Systems (IROS 2000), Oct. 2000.

[101] W. J. Li, G. M. H. Chan, N. N. H. Ching, P. H. W. Leong, and H. Y. Wong. Dynamical modeling and simulation of a laser-micromachined vibration-based micro power generator. *International Journal of Nonlinear Sciences and Numerical Simulation*, 1(5):345–353, Oct. 2000.

[102] W. J. Li, T. C. H. Ho, G. M. H. Chan, P. H. W. Leong, and H. Y. Wong. Infrared signal transmission by a laser-micromachined vibration-induced power generator. In *43rd IEEE Midwest Symposium on Circuits and Systems, Michigan, USA.*, vol. 1, pp. 236–239, 2000.

[103] Lightning Switch. Wireless switch controls. http://www.lightningswitch.com.

[104] Y. Liu, K. Ren, H. F. Hofmann, and Q. Zhang. Electrostrictive polymers for mechanical energy harvesting. In *Proceedings of SPIE The International Society for Optical Engineering*, 2004.

[105] I. Locher, T. Kirstein, and G. Tröster. Routing methods adapted to e-textiles. In *Proc. 37th International Symposium on Microelectronics (IMAPS 2004)*, Nov. 2004.

[106] P. Lukowicz, J. A. Ward, H. Junker, M. Stäger, G. Tröster, A. Atrash, and T. Starner. Recognizing workshop activity using body worn microphones and accelerometers. In *Proceedings of the Second International Conference on Pervasive Computing, Vienna*, Apr. 2004.

[107] W. Ma, L. Rufer, Y. Zohary, and M. Wong. Design and implementation of an integrated floating-gate electrostatic power micro-generator. In *The 13th International Conference on Solid-State Sensors, Actuators and Microsystems (Transducers '05), Seoul, Korea*, June 2005.

[108] W. Ma, W. Wong, and L. Rufer. Dynamic simulation of an implemented electrostatic power micro-generator. In *Symposium on Design, Test, Integration and Packaging of MEMS/MOEMS (DTIP 2005), Montreux, Switzerland*, June 2005.

[109] M. Marzencki, S. Basrour, and B. Charlot. Design, modelling and optimisation of integrated piezoelectric micro power generators. In *Nanotechnology Conference and Trade Show (NANOTECH'05), Anaheim, California, USA*, vol. 3, pp. 545–54, May 2005.

[110] M. Marzencki, B.Charlot, S.Basrour, M.Colin, and L.Valbin. Design and fabrication of piezoelectric micro power generators for autonomous microsystems. In *Symposium on Design, Test, Integration and Packaging of MEMS/MOEMS (DTIP 2005), Montreux, Switzerland*, pp. 299–302, June 2005.

[111] K. Matsuzawa and M. Saka. Seiko human powered quartz watch. In M. Rose, ed., *Proc. Prospector IX: Human Powered Systems Technologies (Space Powered Institute, Auburn University, AL, 1997)*, pp. 359–384, 1997.

[112] Maurer Magnetic AG. Permanent magnets. http://www.maurermagnetic.ch.

[113] S. Meninger, J. O. Mur-Miranda, R. Amirtharajah, A. P. Chandrakasan, and J. H. Lang. Vibration-to-electric energy conversion. *IEEE Transactions on Very Large Scale Integration (VLSI) Systems*, 9(1):64–76, Feb. 2001.

[114] P. Miao, A. S. Holmes, E. Yeatman, T. C. Green, and P. D. Mitcheson. Micro-machined variable capacitors for power generation. In *Electrostatics '03, Edinborough, UK*, Mar. 2003.

[115] P. D. Mitcheson, T. C. Green, E. M. Yeatman, and A. S. Holmes. Architectures for vibration-driven micropower generators. *IEEE Journal of Microelectromechanical Systems*, 13(3):429–440, June 2004.

[116] P. D. Mitcheson, P. Miao, B. Stark, E. Yeatman, A. Holmes, and T. Green. MEMS electrostatic micro-power generator for low frequency operation. *Sensors and Actuators, Part A, in press*, 115(2–3):523–529, Sept. 2004.

[117] P. D. Mitcheson, B. H. Stark, P. Miao, A. S. Holmes, E. M. Yeatman, and T. C. Green. Analysis and optimisation of MEMS electrostatic on-chip power supply for self-powering of slow-moving sensors. In *Eurosensors'03, Portugal*, pp. 48–51, Sept. 2003.

[118] M. Mizuno and D. G. Chetwynd. Investigation of a resonance microgenerator. *Journal of Micromechanics and Microengineering*, 13(2):209–216, 2003.

[119] F. Moll and A. Rubio. Human powered piezoelectric batteries to supply power of wereables electronic devices. *Int. J. Soc. Mater. Eng. Resour*, 10(1):34–40, Mar. 2002.

[120] K. Mossi, C. Green, Z. Ounaies, and E. Hughes. Harvesting energy using a thin unimorph prestressed bender: Geometrical effects. *Journal of Intelligent Material Systems and Structures*, Mar. 2005.

[121] K. Nakano, T. Saito, A. Nakayama, and T. Kurose. A portable generator using vibration due to human walking. In *Power MEMS 2002, International Workshop on Power MEMS, Tsukuba, Japan*, Nov. 2002.

[122] National Instruments Corp. LabVIEW. http://www.ni.com/labview/.

[123] H. Naumann, K. Michel, P. Mossdorf, and U. Freiberg. Bistabile magnetische Sensoren zum Nachweis von elektrischen Stromänderungen - Puls-wire sensors to demonstrate changes of

the electric current intensity. *Technisches Messen*, 58(7/8):283–286, July 1991.

[124] P. Needham and L. Gamlyn. Arrhythmia analysis in the community. In *International Workshop on Wearable and Implantable Body Sensor Networks Proceedings, Imperial College, London, U.K.*, Apr. 2004.

[125] B. Nigg, P. Neukomm, and E. Unold. Ueber die Beschleunigungen die am menschlichen Körper bei verschiedenen Bewegungen auf verschiedenen Unterlagen auftreten. *Orthopaede*, 3:140–147, 1974.

[126] P. Niu, P. Chapman, R. Riemer, and X. Zhang. Evaluation of motions and actuation methods for biomechanical energy harvesting. In *35th Annual IEEE Power Electronics Specialists Conference (PESC 04)*, vol. 35, pp. 2100–2106, June 2004.

[127] A. Nounou and H. F. Ragaie. A lateral comb-drive structure for energy scavenging. In *Proceedings 2004 International Conference on Electrical, Electronic and Computer Engineering, ICEEC'04*, pp. 553–556, 2004.

[128] Oakley Inc. Timebomb watch. http://www.oakley.com.

[129] G. K. Ottman, A. C. Bhatt, H. Hofmann, and G. A. Lesieutre. Adaptive piezoelectric energy harvesting circuit for wireless, remote power supply. In *Collection of Technical Papers AIAA ASME ASCE AHS ASC Structures, Structural Dynamics and Materials Conference*, vol. 4, pp. 2410–2417, 2001.

[130] G. K. Ottman, H. Hofmann, A. Bhatt, and G. Lesieutre. Adaptive piezoelectric energy harvesting circuit for wireless remote power supply. *IEEE Transactions on Power Electronics*, 17(5):669–676, Sept. 2002.

[131] G. K. Ottman, H. F. Hofmann, and G. A. Lesieutre. Optimized piezoelectric energy harvesting circuit using step-down converter in discontinuous conduction mode. *IEEE Transactions on Power Electronics*, 18(2):696–703, Mar. 2003.

[132] J. A. Paradiso and T. Starner. Energy scavenging for mobile and wireless electronics. *Pervasive Computing, IEEE*, 4(1):18–27, 2005.

[133] R. Pelrine and R. Kornbluh. High-speed electrically actuated elastomers with strain greater than 100 %. *Science*, 287(5454): 836–839, Feb. 2000.

[134] R. Pelrine, R. Kornbluh, J. Eckerle, P. Jeuck, S. Oh, Q. Pei, and S. Stanford. Dielectric elastomers: Generator mode fundamentals and applications. *Proceedings of the SPIE The International Society for Optical Engineering*, 2001.

[135] A. W. Penn. Small electrical power sources. *Physics in Technology*, 5(2):115–140, 1974.

[136] S. Platt, S. Farritor, and H. Haider. On low-frequency electric power generation with PZT ceramics. *IEEE/ASME Transactions on Mechatronics*, 10:240–252, 2005.

[137] S. R. Platt, S. Farritor, K. Garvin, and H. Haider. The use of piezoelectric ceramics for electric power generation within orthopedic implants. *IEEE/ASME Transactions on Mechatronics*, 10: 455–461, 2005.

[138] Polar Electro. Heart rate monitors. http://www.polar.fi.

[139] V. M. Ponizovskii. Diamagnetic suspension and its applications (survey). *Instruments and Experimental Techniques*, 24(4):833–841, July 1981.

[140] G. Poulin, E. Sarraute, and F. Costa. Generation of electrical energy for portable devices comparative study of an electromagnetic and a piezoelectric system. *Sensors and Actuators, A: Physical*, 116(3):461–467, Oct. 2004.

[141] H. Qu and J. Gotman. A patient-specific algorithm for the detection of seizure onset in long-term EEG monitoring: Possible use as a warning device. *IEEE Transactions on Biomedical Engineering*, 44:115–122, 1997.

[142] W. Qu, M. Plotner, and J. Fischer-W. Microfabrication of thermoelectric generators on flexible foil substrates as a power source for autonomous microsystems. *Journal of Micromechanics and Microengineering*, 11(2):146–152, Mar. 2001.

[143] M. Ramsay and W. Clark. Piezoelectric energy harvesting for bio MEMS applications. In *Proceedings of SPIE The International Society for Optical Engineering*, vol. 4332, pp. 429–438, 2001.

[144] D. Raskovic, T. Martin, and E. Jovanov. Medical monitoring applications for wearable computing. *Computer Journal*, 2004.

[145] G. Rauscher and C. Radeloff. Impulsdrähte als magnetische Geber für Bewegungs- und Feldsensoren. *Siemens Forsch.- u. Entwickl.-Ber.*, 15(3):135–144, Feb. 1986.

[146] G. Rauscher and C. Radeloff. *Magnetic Sensors*, chapter Wiegand and Pulse-Wire Sensors. VCH Verlag, Weinheim, 1989.

[147] E. K. Reilly, E. Carleton, S. Roundy, and P. Wright. Vibrational energy scavenging via thin film piezoelectric ceramics. In *Advanced Materials for Energy Conversion II*, pp. 325–330, 2004.

[148] L. C. Rome, L. Flynn, E. M. Goldmann, and T. D. Yoo. Generating electricity while walking with loads. *Science*, 309:1725–1728, Sept. 2005.

[149] D. Ross. *Power from Waves.* Oxford University Press, 1995.

[150] S. Roundy, P. K. Wright, and K. S. Pister. Micro-electrostatic vibration-to-electricity converters. In *Proceedings of IMECE2002 ASME International Mechanical Engineering Congress & Exposition, New Orleans, Louisiana*, Nov. 2002.

[151] S. Roundy, P. K. Wright, and J. Rabaey. A study of low level vibrations as a power source for wireless sensor nodes. *Computer Communications*, 26(11):1131–1144, July 2003.

[152] S. Roundy, P. K. Wright, and J. M. Rabaey. *Energy Scavenging For Wireless Sensor Networks : With Special Focus On Vibrations.* Kluwer Academic, 2004. ISBN 1-4020-7663-0.

[153] S. Scherrer, D. G. Plumlee, and A. J. Moll. Energy scavenging device in LTCC materials. In *IEEE Workshop on Microelectronics and Electron Devices (WMED)*, pp. 77–78, Apr. 2005.

[154] Y. Schutz, S. Weinsier, P. Terrier, and D. Durrer. A new accelerometric method to assess the daily walking practice. *International Journal of Obesity*, 26:111–118, 2002.

[155] C. Shearwood, A. Powell, and M. Pate. MEMS: For sensors and optoelectronics. *European Semiconductor*, 17(10):33, Nov. 1995.

[156] C. Shearwood and R. B. Yates. Development of an electromagnetic microgenerator. *Electronics Letters*, 33(22):1883–1884, Oct. 1997.

[157] N. S. Shenck and J. A. Paradiso. Energy scavenging with shoe-mounted piezoelectrics. *IEEE Micro*, 21(3):30–42, May 2001.

[158] B. K. Smith. Definition, expansion and screening of architectures for planetary exploration class nuclear electric propulsion and power systems. Master's thesis, Massachusetts Institute of Technology, 2003.

[159] S. T. Smith, D. G. Chetwynd, and D. K. Bowen. Design and assessment of monolithic high precision translation mechanisms. *Journal of Physics E: Scientific Instruments*, 20(8):977–983, 1987.

[160] S. R. Snarski, R. G. Kasper, and A. B. Bruno. Device for electromagnetohydrodynamic (EMHD) energy harvesting. In *Proceedings of SPIE The International Society for Optical Engineering*, vol. 5417, pp. 147–161, 2004.

[161] J. W. Sohn, S. B. Choi, and D. Y. Lee. An investigation on piezoelectric energy harvesting for MEMS power sources. *Proceedings of the Institution of Mechanical Engineers, Part C: Journal of Mechanical Engineering Science*, 219(4):429–443, Apr. 2005.

[162] R. K. Sood. Piezoelectric micro power generator (pmpg): A MEMS-based energy scavenger. Master's thesis, Massachusetts Institute of Technology, Sept. 2003.

[163] M. E. Staley and A. B. Flatau. Characterization of energy harvesting potential of terfenol-d and galfenol. In *Proceedings of SPIE The International Society for Optical Engineering*, 2005.

[164] T. Starner. Human-powered wearable computing. *IBM Systems Journal*, 35(3–4):618–629, 1996.

[165] T. Starner and J. Paradiso. *"Human Generated Power for Mobile Electronics", Low-Power Electronics Design*, chapter 45, pp. 1–35. CRC Press, 2004.

[166] T. Sterken, K. Baert, R. Puers, and S. Borghs. Power extraction from ambient vibration. In *Proceedings of SeSens (Workshop on*

Semiconductor Sensors) 2002, Veldhoven, the Netherlands, pp. 680–683, Nov. 2000.

[167] M. Strasser, R. Aigner, M. Franosch, and G. Wachutka. Miniaturized thermoelectric generators based on poly-si and poly-sige surface micromachining. *Sensors and Actuators, A: Physical*, A98-A98:535–542, Apr. 2002.

[168] Synopsys Inc. Saber mixed-technology system simulation. http://www.synopsys.com/products/mixedsignal/saber/saber.html.

[169] R. Tashiro, N. Kabei, K. Katayama, Y. Ishizuka, F. Tsuboi, and K. Tsuchiya. Development of an electrostatic generator that harnesses the motion of a living body. *JSME International Journal (Japan Society of Mechanical Engineers)*, 43(4):916–922, 2000.

[170] VAC Vacuumschmelze GmbH. Soft-magnetic materials. http://www.vacuumschmelze.de.

[171] P. Verardi, F. Craciun, and M. Dinescu. Characterization of PZT thin film transducers obtained by pulsed laser deposition. In *IEEE Ultrasonoics Symposium Proceedings*, vol. 1, pp. 569–572, 1997.

[172] T. von Büren, P. Lukowicz, and G. Tröster. Kinetic energy powered computing - an experimental feasibility study. Proceedings of the Seventh International Symposium on Wearable Computers (ISWC 2003), 2003.

[173] T. von Büren, P. D. Mitcheson, T. C. Green, E. M. Yeatman, A. S. Holmes, and G. Tröster. Optimization of inertial micropower generators for human walking motion. *IEEE Sensors Journal*, 6 (1):28–38, Feb. 2006.

[174] S. Walter. *Entwicklung miniaturisierter elektrodynamischer Energiewandler mit Reluktanzläufer*. PhD thesis, TU Berlin, 2004.

[175] J. Wang, G. W. Jewell, and D. Howe. A general framework for the analysis and design of tubular linear permanent magnet machines. *IEEE Transactions on Magnetics*, 35:1986–2000, 1999.

[176] J. Wang, G. W. Jewell, and D. Howe. Design optimisation and comparison of tubular permanent magnet machine topologies. *Electric Power Applications, IEE Proceedings-*, 148:456–464, 2001.

[177] J. Wang, W. Wang, G. W. Jewell, and D. Howe. A low-power, linear, permanent-magnet generator/energy storage system. *IEEE Transactions on Industrial Eletronics*, 49:640–648, 2002.

[178] N. M. White, P. Glynne-Jones, and S. P. Beeby. A novel thick-film piezoelectric micro-generator. *Smart Materials and Structures*, 10 (4):850–852, Aug. 2001.

[179] N. M. White, P. Glynne-Jones, S. P. Beeby, M. J. Tudor, and M. Hill. Design and modelling of a vibration powered micro-generator. *Measurement and Control*, 34(9):267–271, Nov. 2001.

[180] C. B. Williams, A. Pavic, R. S. Crouch, and R. C. Woods. Feasibility study of vibration-electric generator for bridge vibration sensors. In *Proceedings of the International Modal Analysis Conference IMAC*, vol. 2, pp. 1111–1117, 1998.

[181] C. B. Williams, C. Shearwood, M. A. Harradine, P. H. Mellor, T. S. Birch, and R. B. Yates. Development of an electromagnetic micro-generator. *IEE Proceedings Circuits, Devices and Systems*, 148(6):337–342, Dec. 2001.

[182] C. B. Williams, R. C. Woods, and R. B. Yates. Feasibility study of a vibration powered micro-electric generator. In *IEE Colloquium on Compact Power Sources, London, UK*, p. 7, 1996.

[183] C. B. Williams and R. B. Yates. Analysis of a micro-electric generator for microsystems. In *Proceedings of Transducers'95 / Eurosensors IX*, vol. 1, pp. 369–372, June 1995.

[184] C. B. Williams and R. B. Yates. Analysis of a micro-electric generator for microsystems. *Sensors and Actuators, A: Physical*, 52(1):8–11, Mar. 1996.

[185] A. D. Winter. *Biomechanics And Motor Control Of Human Movement*. John Wiley & Sons, 2nd edition, 1990.

[186] D. C. Yates and A. S. Holmes. Micro power radio module. *DC FET Project ORESTEIA, Deliverable ND3.2, Tech. Report.*, 2003.

[187] E. Yeatman. Advances in power sources for wireless sensor nodes. In *Proc. 1st International Workshop on Body Sensor Networks, London, UK*, pp. 20–21, Apr. 2004.

Curriculum Vitae

Personal Information

Thomas von Büren
Born 12 March 1974
Citizen of Flumenthal SO, Switzerland

Education

2000–2006	PhD studies in information technology and electrical engineering (Dr. sc. ETH) at ETH Zurich, Switzerland
1995–2000	M.Sc. studies in electrical engineering (Dipl. El.-Ing. ETH) at ETH Zurich Diploma thesis at LAAS CNRS, Toulouse, France
1989–1995	Kantonsschule Solothurn, Solothurn, Switzerland Matura Type C
1991–1992	Naperville Central High School, Naperville, IL, USA High School Diploma
1986–1989	Secondary school Derendingen/Luterbach, Switzerland
1981–1986	Primary school in Oekingen, Switzerland

Work Experience

2000–2006	Research and teaching assistant at Electronics Laboratory, ETH Zurich, Switzerland
1998	Internship with Philips Semiconductors, Eindhoven, The Netherlands